

Physics and Applications of Optical Nonlinearity in High-Q Microresonators

Thesis by
Zhiquan Yuan

In Partial Fulfillment of the Requirements for the
Degree of
Doctor of Philosophy

The logo for the California Institute of Technology (Caltech), featuring the word "Caltech" in a bold, orange, sans-serif font.

CALIFORNIA INSTITUTE OF TECHNOLOGY
Pasadena, California

2024
Defended January 16th, 2024

© 2024

Zhiqun Yuan

ORCID: 0000-0001-9054-6004

All rights reserved

ACKNOWLEDGEMENTS

The past six years at Caltech for me have been memorable and rewarding. Studying abroad is both challenging and exciting. Luckily Caltech provided me with invaluable resources to pursue my PhD degree. The small campus, convenient and safe neighborhood, and great academic atmosphere make my life and studies enjoyable. Even though the sudden pandemic situation changed my PhD journey in many ways, I am glad I have so much support from all the kind and talented people around.

Foremost, my deepest appreciation goes to my advisor, Prof. Kerry Vahala, for all the guidance and support over the years. More than a distinguished scientist and a pioneer in the field, Prof. Vahala provided our group with a free environment to explore diverse research opportunities. Through countless in-person discussions, I have benefited immensely from his boundless enthusiasm, profound insights and academic rigor. It is such an honor and a privilege to be his student.

I extend my sincere gratitude to Prof. Andrei Faraon, Prof. Harry Atwater, and Prof. Oskar Painter for their service on my graduate committee and for the invaluable input they provided on my thesis. Special thanks to Prof. John Bowers, Prof. Qiang Lin, Dr. Andrey Matsko, Dr. Scott Diddams, and Dr. Stephanie Leifer for their guidance and support in my research endeavors.

I would like to express my gratitude to my group members and collaborators. I'd like to first thank Dr. Chengying Bao and Dr. Yu-Hung Lai for being my mentors when I ventured into this field. The generous sharing of both experimental techniques and life experiences eased my transition. I would like to thank Dr. Myoung-Gyun Suh, Dr. Qi-Fan Yang, Dr. Boqiang Shen, Dr. Heming Wang, Dr. Hao-Jing Chen, Lue Wu, Maodong Gao, Qing-Xin Ji, Bohan Li, Yan Yu, Peng Liu, Jinyu Liu, Jinhao Ge and Kellan Colburn. Our conversations and discussions on both research and daily life were enjoyable and fulfilling.

I want to express my love and thanks to my parents and family, my most solid and unwavering support despite the physical distance. Their belief in me and encouragement to explore the outside world have been my guiding lights. Special thanks to my girlfriend, Zhaoying Chen, for being my companion on this journey. The time we spent together has enriched my life and given me courage. Lastly, to all my friends who have accompanied me on this long journey—life is indeed a journey, and your presence has been a constant source of support and companionship.

ABSTRACT

Optical microresonators trap light in compact volumes at discrete resonant frequencies. Benefiting from the ultra-low propagation loss, the electromagnetic wave intensity is greatly enhanced. Due to the pronounced light confinement, nonlinear optical effects are significantly magnified in the microresonators. In this thesis, I investigate various nonlinear optical phenomena using high quality factor silica wedge and fully-integrated thin film silicon nitride microresonators. The exploration begins with Kerr nonlinearity-induced soliton microcombs followed by their application in mid-IR band gas spectroscopy. The generation of solitons under normal dispersion conditions, which frustrate soliton formation, is then considered. Subsequently, attention is directed towards stimulated Brillouin lasers and their frequency noise performance, including long-term frequency stabilization based on the built-in temperature reference and validation of two modification factors affecting short-term fundamental linewidth. Along this journey, a novel method for calibrating ultra-narrow laser linewidths is introduced. Lastly, this method is employed to measure the narrow linewidth of a visible laser generated through second harmonic generation in silicon nitride resonators.

PUBLISHED CONTENT AND CONTRIBUTIONS

- [1] Bohan Li et al. “High-coherence hybrid-integrated 780 nm source by self-injection-locked second-harmonic generation in a high-Q silicon-nitride resonator.” In: *Optica* 10.9 (2023), pp. 1241–1244. DOI: 10.1364/OPTICA.498391.
Z. Y. participated in the conception of the project, performed the experiments, analyzed the data, and contributed to the writing of the manuscript.
- [2] Zhiquan Yuan et al. “Soliton pulse pairs at multiple colors in normal dispersion microresonators.” In: *Nature Photonics* 610.11 (2023), pp. 977–983. DOI: 10.1038/s41566-023-01257-2.
Z. Y. participated in the conception of the project, performed the experiments, analyzed the data, and contributed to the writing of the manuscript.
- [3] Yu-Hung Lai et al. “Brillouin backaction thermometry for modal temperature control.” In: *Optica* 9.7 (2022), pp. 701–705. DOI: 10.1364/OPTICA.459082.
Z. Y. assisted with the experiments, analyzed the data, and contributed to the writing of the manuscript.
- [4] Zhiquan Yuan et al. “Correlated self-heterodyne method for ultra-low-noise laser linewidth measurements.” In: *Optics Express* 30.14 (2022), pp. 25147–25161. DOI: 10.1364/OE.458109.
Z. Y. participated in the conception of the project, performed the experiments, analyzed the data, and contributed to the writing of the manuscript.
- [5] Chengying Bao et al. “Architecture for microcomb-based GHz-mid-infrared dual-comb spectroscopy.” In: *Nature Communications* 12.1 (2021), p. 6573. DOI: 10.1038/s41467-021-26958-6.
Z. Y. participated in the conception of the project, performed the experiments, analyzed the data, utilized the data processing algorithm, and contributed to the writing of the manuscript.
- [6] Chengying Bao et al. “Interleaved difference-frequency generation for microcomb spectral densification in the mid-infrared.” In: *Optica* 7.4 (2020), pp. 309–315. DOI: 10.1364/OPTICA.382992.
Z. Y. participated in the conception of the project, performed the experiments, analyzed the data, and contributed to the writing of the manuscript.
- [7] Heming Wang et al. “Petermann-factor sensitivity limit near an exceptional point in a Brillouin ring laser gyroscope.” In: *Nature Communications* 11.1 (2020), p. 1610. DOI: 10.1038/s41467-020-15341-6.
Z. Y. participated in the conception of the project, performed the experiments, analyzed the data, and contributed to the writing of the manuscript.

- [8] Zhiquan Yuan et al. “Linewidth enhancement factor in a microcavity Brillouin laser.” In: *Optica* 7.9 (2020), pp. 1150–1153. DOI: 10.1364/OPTICA.394311.

Z. Y. participated in the conception of the project, performed the experiments, analyzed the data, and contributed to the writing of the manuscript.

TABLE OF CONTENTS

Acknowledgements	iii
Abstract	iv
Published Content and Contributions	v
Table of Contents	vi
List of Illustrations	ix
Chapter I: Introduction	1
1.1 Optical microresonators	1
1.2 Optical nonlinearity	2
1.3 Chapter overview	7
Chapter II: Microresonator characterization and soliton generation	9
2.1 Characterization of microresonators	9
2.2 Silica wedge resonator and thin film silicon nitride resonator	11
2.3 Soliton capture and stabilization	14
Chapter III: Architecture for microcomb-based GHz-mid-infrared dual-comb spectroscopy	18
3.1 Introduction	18
3.2 Spectroscopy with GHz resolution and interleaved difference-frequency-generation (iDFG)	19
3.3 Architecture of the DCS system	21
3.4 Characterization of the DCS system	24
3.5 Mid-IR DCS of methane and ethane	27
3.6 Discussion	30
Chapter IV: Soliton pulse pairs at multiple colors in normal dispersion microresonators	32
4.1 Introduction	32
4.2 Recurring spectral windows	34
4.3 Dispersion measurements and soliton pulse pair generation	35
4.4 Pulse pairs and multi-partite states	40
4.5 Additional measurements	42
4.6 Dynamics and numerical simulations of the soliton pulse pair	44
4.7 Discussion	45
Chapter V: Brillouin backaction thermometry for modal temperature control	47
5.1 Introduction	47
5.2 Illustration for the cascaded Brillouin laser induced backaction	48
5.3 Measurement of Brillouin backaction and active locking	51
5.4 Theoretical analysis on cascade Brillouin laser backaction	55
5.5 Discussion	58
Chapter VI: The linewidth enhancement factor in a microcavity Brillouin laser	59
6.1 Introduction	59

6.2	Experiment setup and illustration for α factor	60
6.3	Measurement on α factor and Brillouin phase mismatch	62
6.4	Measurement on the α factor enhanced fundamental linewidth	64
6.5	Theoretical analysis	66
6.6	Additional measurements and information	73
6.7	Discussion	76
Chapter VII: Petermann-factor sensitivity limit near an exceptional point in a Brillouin ring laser gyroscope		
7.1	Introduction	77
7.2	Biorthogonal Noise Enhancement Theory	78
7.3	Measurement on the Petermann factor enhanced fundamental noise	81
7.4	Adler analysis on the enhanced noise and locking bandwidth	83
7.5	Additional information	85
7.6	Discussion	86
Chapter VIII: Correlated self-heterodyne method for ultra-low-noise laser linewidth measurements		
8.1	Introduction	88
8.2	Measurement setup	89
8.3	Modeling of the measurement process	91
8.4	Characterization of the measurement setup	96
8.5	Discussion	103
8.6	Conclusion	105
Chapter IX: High-coherence hybrid-integrated 780 nm source by self-injection-locked second-harmonic generation in a high-Q silicon-nitride resonator		
9.1	Introduction	106
9.2	Characterization on the second-harmonic generation	106
9.3	Frequency noise characterization on the generated SIL 780 nm source	109
9.4	Coupler design principle	111
9.5	Conclusion	112
Bibliography		113

LIST OF ILLUSTRATIONS

<i>Number</i>	<i>Page</i>
2.1 Image of silica wedge resonator.	12
2.2 Image and characterization of thin film silicon nitride resonator.	13
2.3 Phase diagram with normalized pump power and laser-cavity detuning.	14
2.4 Active capture and stabilization of solitons with a continuous wave laser.	15
2.5 Experimental setup for soliton microcomb formation with self-injection locking.	17
3.1 Illustration for interleaved difference-frequency-generation (iDFG).	20
3.2 Experimental setup of the GHz-mid-IR DCS system.	22
3.3 Interferograms and multi-heterodyne spectra of the iDFG densified mid-IR combs.	26
3.4 Dual-comb spectroscopy of methane and ethane mixture using iDFG mid-IR combs.	28
4.1 Soliton pulse pair generation in two- and three-coupled-ring microresonators.	33
4.2 Mode number non-conservation coupling and dispersion for bright soliton formation.	36
4.3 Stable soliton operation in the two-ring resonator measured over 4 h.	38
4.4 Additional optical spectra of the solitons in the two-ring coupled resonator.	39
4.5 Temporal evolution of the soliton pulse pair in the two-ring coupled resonator.	40
4.6 Observation of bipartite and tripartite multi soliton states in two- and three-coupled-ring microresonators.	41
4.7 C and S resonances and autocorrelation measurements of solitons in the coupled-ring resonator.	43
4.8 Comparisons between simulated soliton spectra and experimental measurements.	45
5.1 Experimental setup and illustrations of the cascaded Brillouin laser induced backaction.	49
5.2 Measurement of Brillouin backaction.	52

5.3	Thermal tuning of the backaction with power dithering.	53
5.4	Allan Deviation of SBL beating frequency $\Delta\omega_s$	54
6.1	SBL phase mismatch illustration and experimental setup.	61
6.2	Measured Brillouin gain phase mismatch and α factor.	63
6.3	Measured SBL frequency noise enhancement from the α factor. . . .	65
6.4	Illustration for SBL noise measurement and fitting.	73
6.5	SBL frequency noise enhancement measured using a second device. . .	75
7.1	Brillouin laser linewidth enhancement near an exceptional point. . . .	79
7.2	Measured linewidth enhancement of SBLs near the exceptional point.	82
7.3	Locking zone bandwidth versus SBL amplitude ratio.	84
8.1	Schematic of the correlated self-heterodyne (COSH) measurement setup.	90
8.2	Characterization on RIN suppression.	98
8.3	Measurement dynamic range (lasers with high frequency noise). . . .	100
8.4	Measurement noise floor (DFB laser with SIL).	102
8.5	Frequency noise measurement with and without acoustic shield. . . .	103
8.6	Frequency noise measurement with a short delay line.	104
9.1	Experimental setups and characterization of the Si_3N_4 resonator and SH generation performance.	107
9.2	Frequency noise measurement for SIL pump laser and generated SH laser.	109
9.3	Self-injection locked laser response with pump current induced fre- quency tuning.	110
9.4	Resonator total and intrinsic Q factor measurements plotted versus wavelength.	111

Chapter 1

INTRODUCTION

1.1 Optical microresonators

Like its acoustic counterpart which can store acoustic energy, the optical microresonator (or microcavity) is a structure designed to confine light within small volumes through resonant recirculation [1]. In contrast to traditional bulky bench-top resonators, the term ‘micro’ refers to the small geometric size of such structures, typically in the range of tens of micrometers. In practical terms, resonators with dimensions in the millimeter scale are also classified as microresonators, as long as their mode area is at the micrometer square level.

Within an optical resonator (cavity), electromagnetic waves undergo repeated reflections or circulations, interfering with themselves. Only electromagnetic waves with specific discrete frequencies (resonance frequencies) and particular cross-section patterns exhibit constructive interference, storing energy in the resonator and generating modes. Due to the periodic conditions of the resonator, modes differing only in frequency can be categorized as distinct longitudinal modes, where the round-trip length is an integer multiple (referred to as the mode number) of the laser wavelength. Conversely, modes with different intensity patterns across the cross-section are termed different transverse modes.

Microresonators can be realized in various configurations [1], such as the Fabry–Pérot cavity (composed of two opposing mirrors), whispering-gallery cavity (light circulates around its circumference due to total internal reflection), waveguide ring cavity (where the waveguide cross section confines light and connects its head with its tail), and photonic crystal cavity (featuring a periodic arrangement of structures with band gaps and embedded energy levels). In this thesis, we focus on a SiO_2 wedge microresonator (whispering-gallery cavity) and a thin-film Si_3N_4 microresonator (waveguide ring cavity). Detailed characterization of these two microresonators is presented in section 2.2.

The operational principle of microresonators aligns with that of traditional larger optical resonators. Light with ultra-low propagation loss accumulates a significantly stronger optical field (enhanced by thousands compared to waveguide propagation) and demonstrates an extended photon lifetime. This enhanced light-matter interac-

tion leads to various phenomena, including cavity quantum electrodynamics (cavity QED) [2, 3], optomechanics [4, 5], and biosensing [6]. Moreover, nonlinear effects are magnified by orders of magnitude due to the strong light confinement, as discussed in the subsequent sections.

The compact form factor of the microcavity is advantageous for optical system integration on a semiconductor chip, offering benefits such as mass production, low power consumption, and a small footprint. Quantum effects may also manifest due to the small dimensions of the system. For instance, the small cavity mode volume and low loss enhance the Purcell effect, altering the spontaneous emission rate and behavior of atoms [7].

1.2 Optical nonlinearity

Nonlinear optical effects elucidate the behavior of light in nonlinear media and are often associated with frequency (or wavelength) conversion. Their physics and applications have garnered substantial interest over the past century, with a notable breakthrough — optical frequency comb technology — earning the Nobel Prize in Physics in 2005. Optical nonlinearities manifest in various platforms, including crystalline materials, optical fibers, and other waveguide devices.

In such media, the material's response to the electromagnetic field can be described by the dielectric polarization density $\mathbf{P}(t)$ [8]:

$$\mathbf{P}(t) = \epsilon_0(\chi^{(1)}\mathbf{E}(t) + \chi^{(2)}\mathbf{E}^2(t) + \chi^{(3)}\mathbf{E}^3(t) + \dots), \quad (1.1)$$

where $\mathbf{E}(t)$ is the electric field, and the coefficient $\chi^{(n)}$ represent the n -th order susceptibility of the medium. The first term corresponds to the linear response of the material, and the presence of higher-order terms is indicative of nonlinear response. Strictly speaking, $\chi^{(n)}$ is an $(n + 1)$ -th rank tensor, reflecting the polarization-dependent nature of the parametric interaction and anisotropic nonlinear response, as seen in crystalline materials. In the materials covered in this thesis, these coefficients are typically simplified to scalar values.

Various nonlinear processes entail different levels of light-matter interaction. For instance, stimulated Raman scattering (SRS) and stimulated Brillouin scattering (SBS) processes involve the excitation and generation of phonons within the materials. Conversely, in processes like four-wave mixing and second harmonic generation, energy exchange occurs solely among photons, leaving the quantum state of the nonlinear material unchanged by the interaction with the optical field. In both cases,

energy and momentum conservation are crucial, a condition referred to as the phase matching condition, which ensures the efficient accumulation of the frequency conversion. If the total momentum (or wavevector \mathbf{k}) is not conserved, the nonlinear process becomes oscillatory, and frequency conversion is not efficiently accumulated. In microresonators, wavevectors are typically replaced by the azimuthal mode number, and the phase matching condition remains a critical consideration. The phase matching for different processes will be introduced in the following sections.

Kerr nonlinearity and optical frequency comb

The optical Kerr effect refers to the change of the material's refractive index which is directly proportional to the intensity of the light field. The term 'Kerr' is used analogously to the Kerr electro-optical effect, wherein the change in refractive index is proportional to the square of the external electric field. The third-order nonlinear susceptibility $\chi^{(3)}$ primarily contributes to the Kerr nonlinearities, and the refractive index of the material, in the presence of Kerr effect, can be expressed as [8]

$$n = n_0 + n_2 I, \quad (1.2)$$

where I is the intensity of the electromagnetic wave, n_0 is the linear refractive index, and n_2 is the nonlinear refractive index of the material. The optical Kerr effect directly induces self-phase modulation (SPM) and cross-phase modulation (XPM), with the nonlinear refractive index n_2 in XPM being twice as large as that in SPM.

Assuming two optical frequency components co-propagate in the nonlinear media, the Kerr-induced refractive index modulation will create additional frequency components. This process is known as four-wave mixing, typically occurring within different longitudinal modes in one transverse mode family in a microresonator. For example, in degenerate four-wave mixing, two photons in the pump mode m_0 can be annihilated, and two photons will be created at side modes $m_0 + \Delta m$ and $m_0 - \Delta m$. In more general cases, non-degenerate four-wave mixing occurs in four different modes (mode numbers m, n, p, q , respectively). For phase matching condition, energy conservation, and momentum conservation, $\omega_m + \omega_n = \omega_p + \omega_q$ and $m + n = p + q$, respectively, are required. Starting from one pump mode and cascading this process, an optical frequency comb [9] with hundreds or thousands of comb lines will eventually form. Note that Kerr nonlinearity in resonators is not the only way to obtain frequency combs; other methods, such as electro-optic modulation, are beyond the scope of this thesis.

The optical frequency comb is a collection of phase-locked, coherent laser lines featuring equally spaced frequencies:

$$f_n = f_0 + n f_r, \quad (1.3)$$

where n is an integer, f_0 is an offset frequency common to all comb lines, and f_r is the repetition rate of the comb, the frequency difference between two adjacent comb lines. Optical frequency combs find applications in science and technology, including optical frequency synthesis [10, 11, 12], timekeeping [13, 14], microwave synthesis [15], ranging [16], spectroscopy [17], and astronomical calibration [18].

With appropriate dispersion and nonlinearity, the Kerr frequency comb may satisfy the soliton solution in the nonlinear Schrödinger equation. Solitons are solitary, self-reinforcing, localized wave packets that maintain their shape and speed during propagation. In microresonators, such solitons maintain their shape by balancing anomalous dispersion with Kerr nonlinearity, while the external pump compensates for propagation loss. When coupled out from the cavity, pulses from different round trips form a periodic pulse train, each separated by the round trip time of the soliton within the resonator. When viewed from the frequency domain, these soliton pulses form a frequency comb (soliton microcomb) [19]. Soliton microcombs have been demonstrated in various materials, such as magnesium fluoride [20], diamond [21], silicon nitride [22, 23, 24, 25], silica [26], III-V semiconductors [27, 28], and lithium niobate [29].

Brillouin scattering and stimulated Brillouin laser

Stimulated Brillouin scattering (SBS) is an inelastic scattering process wherein light interacts with acoustic waves. In contrast to the Kerr effect, resulting from the optical field-induced distortion of the electron cloud, the mechanism of SBS is attributed to electrostriction [8]. It can be regarded as a third-order nonlinear optical process and is present in all dielectric materials.

From a classical perspective, when a coherent light wave propagates inside a material, the amplitude of the light wave exerts a force on the atoms, causing a local change in the refractive index. If another light wave with a different frequency propagates in the opposite direction, the interference of the two light waves generates a moving grating, acting as acoustic waves. This moving refractive index grating, in turn, reflects the pump and strengthens the Doppler-shifted laser field. From a quantum mechanical viewpoint, a pump photon may either emit a phonon and generate a photon with a lower frequency (the Stokes process) or absorb a phonon

and generate a photon with a higher frequency (the anti-Stokes process). With a strong optical pump and a relatively short lifetime of phonons, we focus on the Stokes Brillouin process within the scope of this thesis.

To satisfy the phase matching condition, both energy and momentum should be conserved from the pump photon to the created phonon and Stokes photon. In a whispering-gallery mode (WGM) or ring-shaped resonator, light and acoustic waves can only propagate forward and backward. The scattered light can only travel in the opposite direction, as photons have much larger energy and smaller momentum than phonons. The Brillouin shift frequency Ω can be solved as:

$$\Omega = \frac{2v_A}{v_A + v_P} \omega_P, \quad (1.4)$$

where v_A (v_P) is the speed of sound (light) in the material, and ω_P is the angular frequency of the pump light. Since $v_P \gg v_A$, this equation is usually expressed as:

$$\Omega \approx \frac{2v_A}{v_P} \omega_P = \frac{4\pi n v_A}{\lambda_P}, \quad (1.5)$$

where λ_P is the pump light wavelength in vacuum. Taking silica as an example, the Brillouin phonon frequency is around 10.8 GHz, with a bandwidth of 20 - 60 MHz [30]. To enable Brillouin scattering in a resonator, there should be an optical mode with a resonance frequency close to the Stokes wave frequency. This could be achieved by carefully selecting the size of the microresonator (matching cavity free-spectral-range with Brillouin shift frequency) or tuning temperature and pump wavelength to select a suitable pair of modes.

The Brillouin scattering process is a parametric process. Since the acoustic field decay rate is much larger than that of the optical field, the damped acoustic phonons are adiabatically eliminated from the system, and the Stokes photons are amplified. Therefore, the parametric process turns into a stimulated scattering process. Coherent SBS photons start to lase when the pump intensity is above the lasing threshold, generating a Stimulated Brillouin laser (SBL) [31, 32, 33]. SBLs have been demonstrated in multiple microresonator platforms [34, 35, 36, 37, 38, 39, 40, 41]. Due to their high power efficiency [42], flexible operating wavelengths [43], and narrow linewidth [42, 41], SBLs have been applied in a range of applications, including radio-frequency synthesizers [44, 45], ring-laser gyroscopes [46, 41, 47], atomic clocks [48], and high-coherence reference sources [38].

χ^2 nonlinearity and second harmonic generation

As depicted in Eq. 1.1, the second-order optical nonlinearity ($\chi^{(2)}$) arises from the quadratic nonlinear polarization response of the material [8]. Three-wave mixing is facilitated during light interaction with second-order nonlinear materials, and this parametric process is commonly employed for generating lasers at new frequencies. Multiple three-wave mixing processes include sum frequency generation (SFG), difference frequency generation (DFG), second harmonic generation (SHG), and optical parametric oscillation (OPO). Among these, SHG [49] can be considered a degenerate case of SFG where two photons with identical frequency are converted into one photon at twice the frequency (also known as frequency doubling).

Since second harmonic generation is prohibited in media with inversion symmetry, most investigations focus on noncentrosymmetric crystalline materials, such as lithium niobate (LN) [50, 51] and III-V semiconductors [52]. Meanwhile, SHG also occurs in centrosymmetric materials with asymmetric structures. For instance, surfaces and interfaces lead to inversion symmetry breaking and serve as good platforms to study second harmonic generation [53].

In addition to energy conservation, momentum conservation must also be satisfied in the SHG process. However, due to the existence of broadband dispersion, this condition is usually not met. In the waveguide, $2k_\omega = k_{2\omega}$ is not automatically satisfied, where k is the momentum and ω is the pump laser frequency. With a propagation distance z , a nonzero phase difference ($\Delta\phi = (k_{2\omega} - 2k_\omega)z$) accumulates, preventing efficient energy transfer when $\Delta\phi$ reaches π . However, if the sign of $\chi^{(2)}$ is flipped every one period ($\Lambda = \pi/(k_{2\omega} - 2k_\omega)$), then efficient SHG becomes achievable. This method is referred to as quasi-phase matching (QPM). Periodical poling on ferroelectric crystals [54] serves as a good method to modulate $\chi^{(2)}$ and achieve QPM.

In a microresonator, the doubly resonant condition significantly enhances SHG efficiency but also requires the SHG mode frequency to be twice that of the pump mode frequency. Meanwhile, the phase matching condition is expressed as:

$$m_{2\omega} = 2m_\omega + \Delta m. \quad (1.6)$$

Here, $\Delta m \neq 0$ refers to the quasi-phase matching condition, first demonstrated in LN in microresonators [55]. Conversely, $\Delta m = 0$ refers to the critical phase matching condition and usually has higher efficiency. This is achieved by selecting different transverse mode families [56].

1.3 Chapter overview

Chapter 2 provides additional background information on the characterization of optical microresonators and detailed calibrations on the two types of resonators used in later sections. The chapter also introduces two common methods for capturing and stabilizing soliton microcombs.

Chapter 3 explores an application of soliton microcombs in mid-infrared spectroscopy. Interleaved difference frequency generation (iDFG) is utilized to convert near-IR comb light into mid-IR light and also densify the spectral line spacing to accommodate gas absorption features. Dual comb spectroscopy is implemented for fast acquisition, and also inherits frequency stability from near-IR combs. Methane and ethane spectra are measured over intervals as short as 0.5 ms as a demonstration.

Chapter 4 focuses on the generation of bright soliton pulse pairs in an ultra-low-loss thin film Si_3N_4 resonator. Unlike conventional microcombs, pulses in this system cannot exist alone; instead, they phase-lock in pairs through interaction at the coupling section. The recurring dispersion also enables the generation of multi-color pulse pairs in a single coupled resonator.

Chapters 5 to 8 delve into the various characteristics of Brillouin lasers in microresonators, emphasizing their linewidth performance. In **Chapter 5**, the mode-pulling effect and cascade Brillouin backaction are studied. Brillouin backaction is used to measure and phase-sensitively lock modal temperature to a reference temperature defined by the Brillouin phase matching condition. With feedback to environmental thermal fluctuations, long-term frequency-stable operation is achieved.

Chapter 6 and **Chapter 7** verify two correction factors for the fundamental linewidth formula of stimulated Brillouin lasers (Schawlow–Townes linewidth). **Chapter 6** studies the linewidth enhancement factor (also known as the Henry factor) of the Brillouin laser, showing its equality to the normalized phase mismatch of the Brillouin process. A large Henry factor significantly increases the laser linewidth and should be carefully controlled to minimize linewidth. **Chapter 7** studies the Petermann factor which affects the laser linewidth when two or more lasing modes are present. The larger effective noises can be attributed to the non-orthogonality of lasing modes. These results are linked to exceptional point sensors, where the signal enhancement factor is exactly canceled by the increasing noise when working near an exceptional point, providing no fundamental signal-to-noise ratio improvement.

Chapter 8 mainly introduces a correlated self-heterodyne (COSH) method to measure ultra-narrow laser linewidth. This method is capable of measuring frequency noise as low as $0.01 \text{ Hz}^2/\text{Hz}$ at a 1 MHz offset frequency and also features low optical power requirements, fast acquisition time, and high-intensity noise rejection. Ultra-narrow linewidth self-injection-locked laser noises are calibrated as a demonstration.

Chapter 9 investigates second harmonic generation in silicon nitride microresonators. The chapter introduces the photogalvanic effect and its induced second-order nonlinearity. By self-injection-locking a 1560 nm distributed feedback semiconductor laser to a high- Q resonator, a record-low frequency noise floor of $4 \text{ Hz}^2/\text{Hz}$ is achieved for the 780 nm emission using the COSH method.

Chapter 2

MICRORESONATOR CHARACTERIZATION AND SOLITON GENERATION

2.1 Characterization of microresonators

Q Factor and Loss Rate

Nonlinear optics benefits from the high power stored in a microresonator, and the ability to store energy can be characterized by a dimensionless parameter, the quality factor (Q). For a specific cavity mode, the Q factor is defined as the ratio of the initial energy stored in the resonator to the energy lost in one radian of the cycle of oscillation, and is equal to:

$$Q = \frac{\omega}{\kappa_t}, \quad (2.1)$$

where ω is the angular frequency of the pump light, and κ_t is the total loss rate of the cavity mode. The total loss rate κ_t has two sources: intrinsic loss rate κ_0 and external loss rate κ_{ex} :

$$\kappa_t = \kappa_0 + \kappa_{\text{ex}}. \quad (2.2)$$

The intrinsic loss rate usually results from material absorption and scattering, while external coupling loss rate refers to energy exchange with the environment, such as transmission from the mirrors in the Fabry–Pérot resonator or light tunneling from the cavity evanescent field to a nearby waveguide. It is worthwhile to note that ‘intrinsic’ and ‘external’ are also related to the definition of the system and environment. Similarly, external quality factor (Q_{ex}) and intrinsic quality factor (Q_0) can be defined as:

$$Q_{\text{ex}} = \frac{\omega}{\kappa_{\text{ex}}}, Q_0 = \frac{\omega}{\kappa_0}. \quad (2.3)$$

When $\kappa_{\text{ex}} = \kappa_0 = \kappa_t/2$, all incoming light is coupled into the cavity, and there is no light bypassing the cavity. This condition is known as the critical coupling condition. The critical coupling condition leverages the total Q factor and efficiency of energy coupling, which is crucial in actual practice.

State-of-the-art microresonators typically have a Q factor ranging from 10^6 to 10^9 and accumulate high circulation light intensity under small input power. The circulation power I_{circ} can be calculated as:

$$I_{\text{circ}} = \int_t^{t+\tau} \frac{cP_{\text{in}}}{V_{\text{mode}}} dt' \approx \frac{Q}{V_{\text{mode}}} \frac{c}{\omega} P_{\text{in}}. \quad (2.4)$$

For instance, in a 3 mm diameter silica wedge resonator ($V_{\text{mode}} \approx 5 \times 10^5 \mu\text{m}^3$), at 1550 nm pump wavelength with 1 mW input power (P_{in}), I is calculated to be 10 MW/cm² when $Q = 200$ million. This high energy flux is beneficial for triggering nonlinear optical effects.

Besides a high Q factor, the power density is greatly enhanced when the light is confined in a small volume. Here, the effective mode volume in the previous equation is defined as:

$$V_{\text{mode}} = \frac{(\int |\mathbf{E}|^2 dV)^2}{\int |\mathbf{E}|^4 dV}, \quad (2.5)$$

where \mathbf{E} is the modal field distribution. It is worthwhile to note that when multiple materials are involved in the resonator, the integral needs to be weighted by material nonlinearities. Since, in most resonators we are working with, the system possesses rotational symmetry, the transverse mode family is mainly distinguished by the cross-section pattern. Similarly, we can define the effective mode area as:

$$A_{\text{mode}} = \frac{(\int |\mathbf{E}|^2 dA)^2}{\int |\mathbf{E}|^4 dA}. \quad (2.6)$$

FSR and dispersion

Another key parameter of the microresonator is the free-spectral range (FSR), defined as the frequency difference between adjacent modes in the same transverse mode family. In a microresonator, the FSR can be calculated as:

$$\frac{2\pi mc}{\omega_m} = m\lambda_m = n_g L, \quad (2.7)$$

$$\text{FSR} = \omega_{m+1} - \omega_m = \frac{2\pi c}{n_g L}, \quad (2.8)$$

where m is the azimuthal mode number, ω_m (λ_m) is the frequency (wavelength) of the m -th mode, c is the speed of light in the vacuum, n_g is the group refractive index of the resonator mode, and L is the round trip length of the resonator. FSR is also related to the round trip time of a resonator mode.

In the absence of dispersion (equivalently, n_g is constant at different wavelengths), the resonance frequencies ω_m are equally separated by the FSR of the microcavity. However, when dispersion is considered, FSR (equivalently, the group velocity) changes with wavelength. The resonant frequencies of the mode family are usually approximated as a Taylor series in mode number:

$$\omega_m = \omega_{m_0} + D_1(m - m_0) + \frac{1}{2}D_2(m - m_0)^2 + \sum_{j>2} \frac{1}{j!}D_j(m - m_0)^j, \quad (2.9)$$

where D_j is the j -th order dispersion coefficient. Specifically, $D_1/2\pi$ equals to the FSR at mode m_0 , D_2 is the second-order dispersion coefficient, and higher-order terms are often neglected. When $D_2 > 0$ ($D_2 < 0$), the dispersion relation is referred to as anomalous (normal) dispersion. The sign of D_2 is not crucial when considering phase matching between a few cavity modes (such as Brillouin scattering and second harmonic generation), but it becomes crucial when considering four-wave mixing and the possible generation of optical frequency comb. Only under the condition of anomalous dispersion, the nonlinear frequency shift can be compensated by the dispersion to generate sidebands.

2.2 Silica wedge resonator and thin film silicon nitride resonator

In this section, we will briefly introduce the fabrication and basic characterization of the two optical microresonators used in our group and this thesis.

Silica Wedge Microresonator

The silica wedge resonator fabrication process was developed in our group in 2012 [37] (see Fig. 2.1). The side views show that it belongs to the whispering-gallery mode resonator, and the optical field is mainly confined within the wedge area. The concept of a whispering gallery arose in the late 19th century, in the context of the propagation of sound waves confined in galleries, with the most famous example being the dome of St. Paul's Cathedral in London. Sound can be guided near the wall of a circular chamber, so a whisper from one side of the room is clearly heard at the other side.

During the fabrication process, SiO_2 is thermally grown to an 8 μm thickness on a 4-inch high-purity float-zone silicon wafer. After photolithography, the unwanted silica is wet etched with buffered HF, and underneath silicon is dry etched with XeF_2 to form a pillar and reduce optical loss. The detailed fabrication process is described in Ref. [37].

With a constant finesse and low material loss, the intrinsic Q factors were characterized by linewidth measurement to be around 400 million. Benefiting from later process improvement, an intrinsic Q factor as high as 1 billion was demonstrated [57]. Based on different photolithography patterns, FSR has been obtained ranging from around 1 GHz [58] to less than 100 GHz [37]. Leveraging high Q factors and suitable repetition rates for radio frequency (RF) generation, an FSR of 10 - 20 GHz (corresponding to a cavity diameter of 3-6 mm) is most frequently used in soliton generation. On the other hand, in Brillouin laser generation and gyro

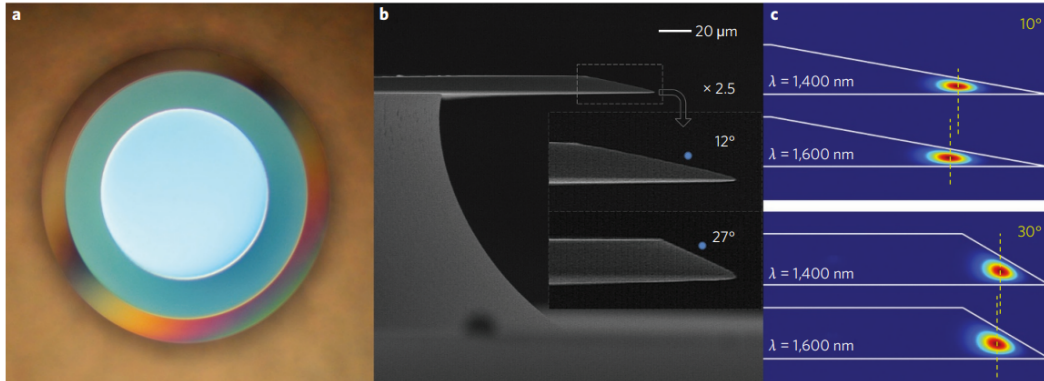


Figure 2.1: **Image of silica wedge resonator.** (a) Top view of a 1-mm diameter wedge resonator. (b) Scanning electron micrograph of the side view of the wedge resonator. Insets: slightly magnified micrographs of resonators with different wedge angles. (c) Simulated optical mode profiles of the fundamental mode. The figure is from Ref. [37].

applications, the Brillouin shift should be an integer multiple of FSR to satisfy the phase matching condition, and high sensitivity benefits from a large surface area. Thus, an FSR of 1.8 GHz (36 mm diameter) is preferred [59]. Due to the thickness of the microresonator, a relatively large mode area often lies within $45 - 60 \mu\text{m}^2$ and the microresonators hold many transverse mode families. Their coupling and hybridization may distort the mode spectrum and lead the generation of dispersive waves during soliton formation [60, 26]. Within the telecommunication band (near 1550 nm), the mode dispersion is usually anomalous. Normal dispersion appears at shorter wavelengths, and a smaller oxide thickness or mode hybridization is needed to generate a soliton microcomb [61].

Since the refractive index of silica is small compared with most dielectric materials, cladding materials are not allowed for silica wedge resonators. In most cases and throughout this thesis, we coupled light into the resonator with fiber tapers [62, 63]. When the taper width is comparable to the laser wavelength, the evanescent field of the taper will couple to the WGM in the cavity. Detailed taper fabrication and characterization are described in Ref. [64]. The coupling between the tapered fiber and the resonator can be tuned by their relative location with a 3-dimensional translation stage or otherwise fastened in a packaged device [65].

Thin film Si_3N_4 ring microresonator

In recent years, to enhance the integration capabilities of microresonators, ultra-low-loss thin film silicon nitride waveguides fabricated in a high-volume complementary

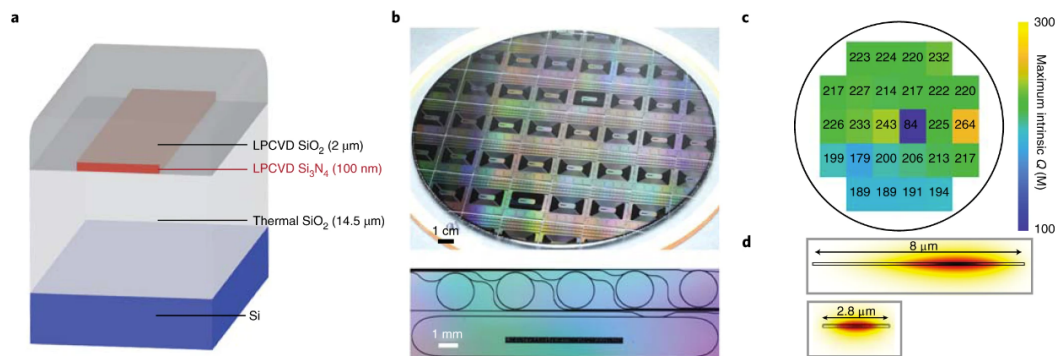


Figure 2.2: Image and characterization of thin film silicon nitride resonator. (a) Cross-sectional diagram of the ultra-low-loss waveguide consisting of Si₃N₄ as the core material, silica as the cladding and silicon as the substrate. (b) Top: photograph of a CMOS-foundry-fabricated 200-mm-diameter wafer after dicing. Bottom: a top view showing the 30 GHz FSR ring resonators and a 5 GHz FSR racetrack resonator. (c) The average Q factors for each of three 30 GHz FSR ring resonators on each of the 26 dies of the wafer. (d) Simulated optical mode profiles of a 30 GHz FSR ring resonator (top) and a 5 GHz FSR racetrack resonator (bottom). The figure is from Ref. [66].

metal–oxide–semiconductor (CMOS) foundry have become a hot topic since 2021 [66, 67] (see Fig. 2.2).

In the foundry, thermal silica is first grown on the silicon substrate, and silicon nitride is deposited on the top (usually 100 nm thickness) using low-pressure chemical vapor deposition (LPCVD). After photolithography, plasma etching is performed to shape the layer of silicon nitride into the target geometric structure, such as a ring or a racetrack. Another layer of silica is then deposited on the top as the guiding material and also as cladding to protect the waveguide. The whole device is then annealed at 1000 °C to let the hydrogen inside the silicon nitride core and cladding silica diffuse out. The detailed fabrication process is described in Ref. [66].

As shown in the mode profiles (Fig. 2.2(d)), about 90% of the mode is in the silica cladding. This type of resonator is therefore called a low confinement silicon nitride resonator. Since silica has much lower loss than silicon nitride, low confinement silicon nitride waveguides tend to be less lossy than their high confinement counterparts, where the majority of the mode is confined inside the silicon nitride core [68]. Over the silicon wafer, these resonators possess consistent and repeatable high Q factors of over 200 million (Fig. 2.2(c)). Within the scope of this thesis, these kinds of thin film Si₃N₄ resonators are mostly single-mode TE resonators. It is worthwhile to note that single-mode TM resonators with a similar process have been reported

with higher Q factors (over 700 million) due to less scattering loss [69].

The dispersion of these low confinement silicon nitride resonators is found to be normal dispersion across the telecommunication C-band [66]. Due to the single-mode nature of the waveguide, the dispersion exhibits no avoided mode crossings. Bright soliton formation is therefore forbidden without any special dispersion engineering. In Chapter 4, we will alter the dispersion by introducing mode coupling with another nearby resonator. Besides resonators, an integrated waveguide coupler is also available during fabrication and effectively couples the light into/out of the cavity with proper simulation. The precision of the lithography guarantees the actual device resembles the design. Light is coupled into/out of the semiconductor chip and coupler waveguide through butt coupling on the chip edge with lensed fibers.

2.3 Soliton capture and stabilization

In this section, we will introduce two methods to capture and stabilize soliton states.

Continuous wave pumping

Under an anomalous dispersion relation, the bright soliton state is a stable solution to the Lugiato-Lefever equation (LLE). However, thermal effects from the resonator make it challenging to achieve and stabilize the soliton state. As shown in the phase

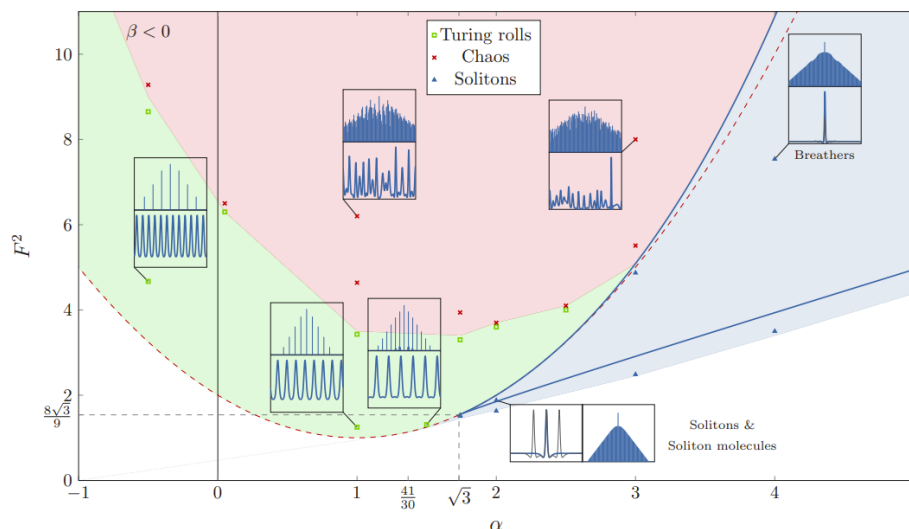


Figure 2.3: **Phase diagram with normalized pump power and laser-cavity detuning.** Stable solutions to the Lugiato-Lefever equation at anomalous dispersion are Turing patterns (green area), modulation instability (red area), solitons, soliton molecules, and breathers (blue area). The figure is from Ref. [70].

diagram [70] (Fig. 2.3), solitons become solutions to the LLE under the red-detuned condition (laser frequency smaller than the hot cavity resonance). To achieve the soliton state, the pump laser frequency needs to scan from the blue side of the cavity resonance to the red side. Modulation instability (chaos) is first obtained, during which four-wave mixing creates incoherent comb lines and forms the noisy comb state. When the laser is further red-detuned, the soliton state is achieved, showing abrupt, “step-like” features in the intracavity power [20, 71] (Fig. 2.4(a)).

A significant and sudden reduction in intracavity power drop is observed when entering the soliton step (Fig. 2.4(a)). The resulting thermal effect may lead to a blue shift of the cavity resonance and cause the laser to operate out of cavity mode, therefore jeopardizing soliton capture. Several different methods have been demonstrated to overcome this thermal effect-induced destabilization. When the thermal effect is relatively weak, such as in magnesium fluoride (MgF_2) resonators, the red-detuned soliton regime can be achieved by changing the sweep speed of the pump laser [20]. When the thermal effect is stronger, modulation on the pump power using the ‘power-kicking’ method [24, 71] or adding an auxiliary laser [72] are developed to compensate for the total intracavity power decrease when entering the soliton state.

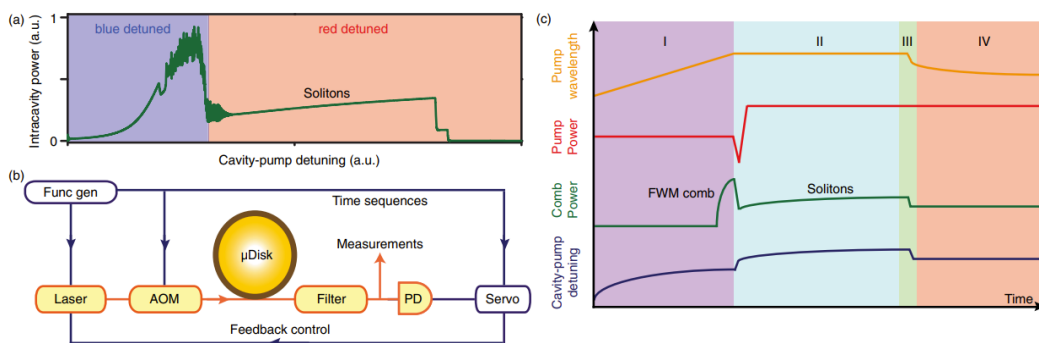


Figure 2.4: Active capture and stabilization of solitons with a continuous wave laser. (a) Simulated intracavity power change when the pump laser scans over the resonance from the blue side to the red side. The steps on the red-detuned side indicate soliton formation. (b) Schematic of experimental setup. (c) Four phases of feedback-controlled soliton excitation: (I) pump laser scans into cavity resonance from the blue-detuned side; (II) laser scan stops and pump power is reduced (around $10 \mu\text{s}$) to trigger solitons, and then increased (around $100 \mu\text{s}$) to extend soliton existence range; (III) servo control is engaged to actively lock the soliton power by feedback control of laser frequency; (IV) lock sustains and solitons are fully stabilized. The figure is from Ref. [71].

In our group, the ‘power-kicking’ technique is mostly used. The pump laser is first sent into an acousto-optic modulator (AOM) and then coupled into the resonator (Fig. 2.4(b)). The function generator produces a waveform and sends it into the AOM to control the pump power change (red trace in Fig. 2.4(c)). All the instruments are synchronized. At the beginning of the scanning, not all pump power is transmitted through the AOM. When the scanning stops at the soliton state, the pump power quickly drops and then recovers the maximum power, compensating for the intracavity power drop.

The above methods compensate for the thermal effect and obtain a soliton ‘step’. However, long-term drifts of the cavity resonance or pump laser frequencies may still lead to the loss of the soliton state. Therefore, active feedback is necessary to guarantee long-term stable operation. One key parameter, the laser-cavity detuning $\delta\omega$, is one-to-one related to the soliton power through the following expression [26]:

$$P_{\text{sol}} = \frac{2\eta A_{\text{mode}}}{n_2 Q} \sqrt{-2nc\beta_2\delta\omega}, \quad (2.10)$$

where $\eta = Q/Q_{\text{ex}}$ is the coupling efficiency, and $\beta_2 = -nD_2/cD_1^2$ is the group velocity dispersion. In practice, the pump comb line is filtered with a fiber Bragg grating (FBG), and the remaining comb power is sent to a photodiode (PD). After subtracting a set point in the servo control box, an error signal is generated and sent to the piezo controller of the laser for long-term locking.

Self-injection locking

Besides traditional pumping the cavity with a continuous-wave laser, a new and more integrated method for generating soliton microcombs was reported in 2020 [73].

In the experiment, a high- Q microresonator is butt-coupled to a commercial distributed-feedback (DFB) laser via inverse tapers (Fig. 2.5(a)). The laser is driven by a DC current source. Approximately 30-50 mW of optical power from the DFB laser is launched into the microresonator, and the backscattered pump light couples back into the resonator mode of the DFB laser. Due to self-injection locking, the semiconductor laser is locked to the resonator mode, and the laser linewidth also narrows down [74]. The operation does not require complex startup and feedback protocols that necessitate difficult-to-integrate optical and electrical components. Instead, the detuning between the feedback-locked laser and the cavity resonance can be controlled by the phase ϕ accumulated in the feedback path. The air gap between the

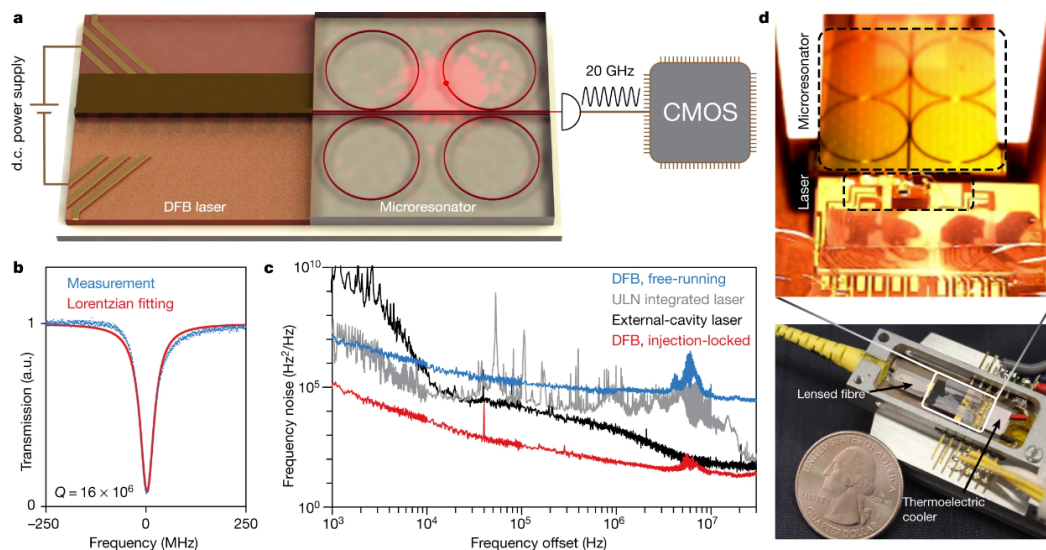


Figure 2.5: Experimental setup for soliton microcomb formation with self-injection locking. (a) Rendering of the soliton microcomb chip driven by a DC power source, producing soliton pulse signals at electronic-circuit rates. (b) Transmission signal when scanning the laser across a cavity resonance (blue). (c) Frequency noise spectral densities of the DFB laser when it is free-running (blue) and feedback-locked to a high- Q Si_3N_4 microresonator. (d) Images of a pump/microcomb in a compact butterfly package. The figure is from Ref. [73].

chip and the DFB laser is controlled by the underneath translation piezo stages to change this feedback phase. Given its compact footprint and the absence of control electronics, the pump-laser/microcomb system was mounted into a butterfly package (Fig. 2.5(d)) to facilitate measurements and also enable portability.

When considering the nonlinear effect, there is a single operating point at the intersection of the laser tuning curve and the intracavity power curve. This behavior enables soliton mode-locking by the simple power-on of the pump laser (i.e., no triggering or complex tuning schemes). Since the entire soliton initiation and stabilization are described and realized by the physical dynamics of laser self-injection locking in combination with the nonlinear resonator response, this kind of self-injection locking-induced soliton formation is automatic and robust. Without any external feedback control, the soliton generation is capable of existing for a few hours. Meanwhile, by periodically switching on and off the laser current, the soliton resembles the pump laser state and shows turnkey operation.

ARCHITECTURE FOR MICROCOMB-BASED GHZ-MID-INFRARED DUAL-COMB SPECTROSCOPY

3.1 Introduction

¹ Over the past two decades, frequency combs have revolutionized numerous applications spanning from time keeping, frequency synthesis, spectroscopy, low noise microwave generation, LIDAR, and exoplanet exploration, among other areas. As an adaptation of frequency combs to spectroscopy, is the dual-comb spectroscopy (DCS) method. Dual-comb spectroscopy works by mapping an optical comb of frequencies into radio-frequencies by multi-heterodyne beat with a second comb having a slightly different repetition rate. Because the two combs sample absorption spectra with a resolution set by their line spacing (or repetition rate), analysis of the corresponding comb of radio frequencies reveals these spectra in a multiplexed fashion without the need for bulky spectrometers or mechanical moving part [77, 78, 79].

And DCS in the mid-infrared (mid-IR) is of keen interest because of inherently strong molecular spectroscopic signatures in these bands. Comb generation in the mid-infrared has traditionally used methods that rely upon mode locked pulse generation, including difference-frequency-generation (DFG), optical parametric oscillation, and supercontinuum generation [80, 79]; and there is considerable progress using such systems for mid-IR DCS [81, 82, 83, 84, 85, 86, 87, 88, 89, 90]. More recently, mid-IR comb generation by DFG using electro-optic frequency combs (EO-comb) has also been demonstrated [91, 92]. In contrast to conventional mode locking, this approach offers rate tunability to the X-band range (8-12 GHz) and higher [92]. With the advent of thin-film lithium niobate technology, EO-combs have potential for chip-integration [93]. Indeed, on-chip lithium niobate microcavity-based EO-combs have been used for DCS in the near-IR [94].

Also offering high repetition rates and chip integration are soliton microcombs [20, 19]. On account of their compact size, these devices operate readily in the

¹Work presented in this chapter has been published in [75] “Interleaved difference-frequency generation for microcomb spectral densification in the mid-infrared.” *Optica* 7.4 (2020), pp. 309–315; [76] “Architecture for microcomb-based GHz-mid-infrared dual-comb spectroscopy.” *Nature Communications* 12.1 (2021), p. 6573.

X to millimeter-wave bands. Here, we report microcomb-based DCS with GHz resolution in the mid-IR band. The two GHz-rate mid-IR combs are generated by interleaved difference-frequency-generation (iDFG) applied to four near-IR combs. These four combs are linked to counter-propagating (CP) solitons [95] formed within a single microcavity. Because all four combs required to generate the two mid-IR combs rely upon stability derived from a single high-Q microcavity, the system architecture is both simplified and does not require external frequency locking. The near-infrared phase stability is successfully transferred to the mid-IR for DCS. DCS measurements of methane and ethane near $3.3 \mu\text{m}$ are performed and the spectral resolution can be tuned on demand. Normalized precision as high as $1.0 \text{ ppm} \cdot \text{m} \cdot \sqrt{s}$ is demonstrated. Although at an early phase of development, the results are a step towards mid-IR gas sensors with chip-based architectures for chemical threat detection, breath analysis, combustion studies, and outdoor observation of trace gases.

3.2 Spectroscopy with GHz resolution and interleaved difference-frequency-generation (iDFG)

In Ref. [96], the optical frequency resolution for DCS was discussed. On the one hand, since most gas species have absorption peaks with $\sim 10 \text{ GHz}$ bandwidth, too large line spacing ($> 10 \text{ GHz}$) will cause undersampling of the spectral signatures for gases (see inset of Fig. 3.1). On the other hand, high repetition rate of the frequency comb suggests high acquisition rate of spectroscopy with shorter single frame time and relatively broad bandwidth. Meanwhile, The saturation power for a certain PD is fixed. With small repetition rate (such as $\sim 100 \text{ MHz}$ in fiber laser combs), high comb line numbers will decrease the average power per comb line and therefore decrease the maximum signal-to-noise ratio (SNR) per comb line. For balance between acquisition rate and spectral resolution, DCS at GHz rates is considered to be relatively optimal for sensing of ambient gases (with linewidths narrower than 10s of GHz) [96, 97]. In their demonstration [96], a 200 MHz fiber laser comb was selectively filtered by a fiber cavity to form a 1 GHz repetition rate comb and performed DCS in the near-IR.

Previously, microcomb-based DCS has been reported at rates of 22 GHz and 450 GHz in the near-IR [98, 99] and 127 GHz in the mid-IR [81]. These high repetition rates result from their small form factors. While offering extremely short acquisition times, these rates are too high for spectroscopy of many species. Special efforts have been directed to reduce near-IR microcomb rates to the single-digit GHz range

resolution remains quite challenging for chip-based devices, including quantum cascaded laser frequency combs [103, 104].

To address this problem, a 1.5 micron soliton microcomb [26] and a 1 micron electro-optic comb (EO-comb) [105] having different repetition rates are used here to provide pumping for mid-IR comb generation. Due to this repetition rate difference (Δf_r), the interaction of soliton and EO-comb pulses generates 3.3 micron light pulses that (subject to conditions described below) can repeat after $1/\Delta f_r$ (Fig. 3.1(a)) thereby creating a temporal interleaving effect. Thus, iDFG not only converts the near-IR combs into the mid-IR, but also reduces the repetition rate and thereby densifies the mid-IR comb spectrum, making them suitable for methane spectroscopy. The line spacing is also tunable by adjustment of Δf_r .

During iDFG, a uniform line spacing of the iDFG-generated mid-IR comb requires that $\Delta f_r = m f_r / n$ where m, n are mutually-prime (see Fig. 3.1(b)). To ensure this condition, the soliton stream is detected to generate a 22 GHz microwave signal f_r and is then electrically processed to create the EO-comb drive signal frequency equal to $f_r^{\text{EO}} = (N - 1) f_r / N$ (Fig. 3.1(a)). This ensures $\Delta f_r = f_r / N$ where N is an integer (typically 16, 32) and guarantees a strict frequency (and phase) relationship between the EO-comb and soliton comb repetition rates. Significantly, the approach also leverages the excellent microwave stability of the soliton microcomb to replace a bulk microwave source that is normally required to drive the EO-comb.

3.3 Architecture of the DCS system

To perform DCS, two iDFG systems with close but non-identical repetition rates should be able to work simultaneously. Counter-propagating solitons [95] in silica resonators act as a good candidate for the two near-IR microcomb sources for both close repetition rates and high mutual coherence.

The experimental setup is illustrated in Fig. 3.2(a). It shows two 3.3 μm frequency combs generated in upper and lower branches of the optical train, followed by combining (far right in the figure) for input to the test gas cell. The two combs are photodetected after passage through the gas cell, and this multi-heterodyne process creates a radio-frequency spectrum that contains the mid-IR absorption spectrum of the gas. The spectrum is obtained by fast Fourier transform (FFT) of the time-domain interferogram signal of the dual combs. The gas cell (Wavelength Reference) has a length of 5 cm and contains $\sim 2\%$ methane (CH_4) and $\sim 0.5\%$ ethane (C_2H_6) buffered by nitrogen to a total pressure of 760 Torr (parameters can have

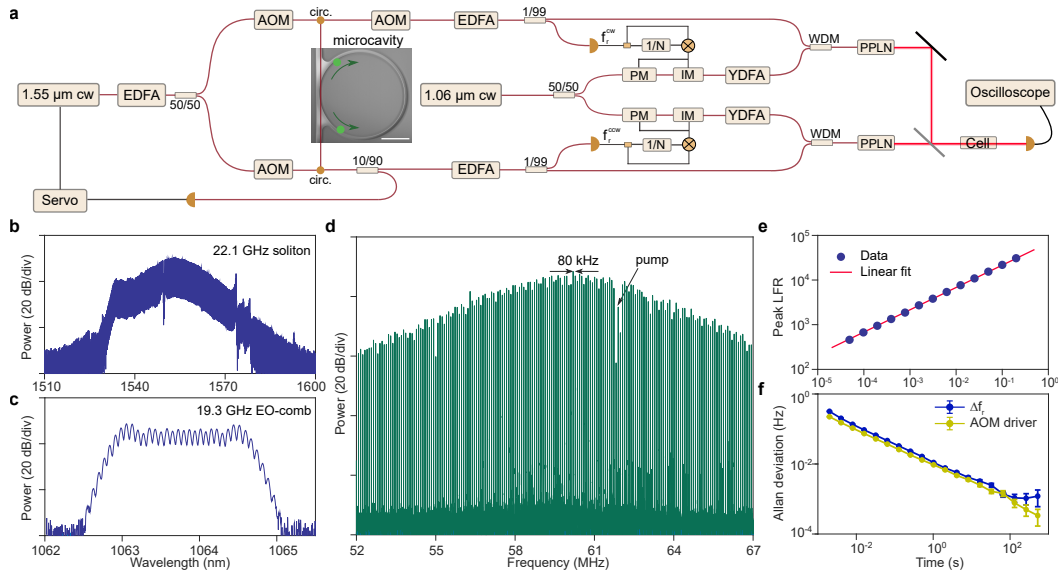


Figure 3.2: Experimental setup of the GHz-mid-IR DCS system. (a) Counter-propagating (CP) solitons at $1.55 \mu\text{m}$ are generated in a silica microcavity to provide two of four comb signals. These solitons are photo-detected and the resulting signals are processed to create the two other comb signals by electro-optic modulation at $1.06 \mu\text{m}$. These near-IR combs are combined in pairs to pump PPLN crystals for generation of GHz line spacing mid-IR combs by interleaved difference frequency generation. These mid-IR comb sources pass through a gas cell and are detected for dual-comb spectroscopy. f_r^{cw} (f_r^{ccw}) corresponds to the cw (ccw) soliton repetition rates. AOM: acousto-optical modulator, circ: circulator, PM: phase modulator, IM: intensity modulator, EDFA: erbium-doped fibre amplifier, YDFA: ytterbium-doped fibre amplifier, WDM: wavelength division multiplexer, PPLN: periodically poled Lithium Niobate. Scale bar: 1 mm. (b) Optical spectrum of $1.55 \mu\text{m}$ soliton comb. (c) Optical spectrum of $1.06 \mu\text{m}$ EO-comb. (d) Multi-heterodyne beat between two CP soliton microcombs (repetition rate difference, Δf_r , is 80 kHz). The beat note produced by the counter-pumps is identified. One of the microcombs is shifted by 55 MHz using the AOM placed after the cavity. (e) Peak LFR of the comb lines in panel (d) as a function of averaging time τ . The solid line is a fit of the $\sqrt{\tau}$ trend. (f) Measured Allan deviation of Δf_r is close to the stability of the AOM driver. The frequency of the AOM driver (a radio frequency function generator) was set to be Δf_r in this measurement. The error bar corresponds to the standard deviation of the Allan deviation.

$\pm 5\%$ uncertainty). Such a methane concentration is equivalent to about 1 ppm in an ambient environment when passing the comb light through a 1 km open path for field measurements.

Each mid-IR comb is generated by iDFG in a PPLN crystal (4 cm long, NTT Electronics) of two near-IR combs: a soliton microcomb at $1.55 \mu\text{m}$ (Fig. 3.3(b)) and

an EO-comb (Fig. 3.3(c)) at $1.06 \mu\text{m}$. Counter-pumped clockwise (cw) and counter-clockwise (ccw) solitons formed in a single silica resonator [37] are input to upper and lower branches of the optical train. On account of the silica Raman response, the soliton repetition rates (f_r^{cw} or f_r^{ccw}) can be independently fine-controlled by two acousto-optical modulators (AOMs) placed before the resonator [95]. Their approximate repetition rate is 22 GHz. Another AOM after the microcavity, driven by a fixed 55 MHz signal, is used to shift the frequencies of one of the microcombs so as to avoid spectral aliasing upon multi-heterodyne beating of the two combs in both the near-IR and the mid-IR. Each EO-comb drive frequency is derived from a corresponding photo-detected soliton repetition frequency and set to be $(N - 1)f_r^{\text{cw(ccw)}}/N$ (N is an integer). This results in interleaving of the near-IR combs and densifies the mid-IR comb line spacing to $22 \text{ GHz}/N$ as described in the previous section. 2.8 GHz and 1.4 GHz mid-IR line spacings are demonstrated, corresponding to $N=8$ or 16.

For high precision measurements, the two mid-IR comb spectra must have excellent relative frequency stability. Several features of the current system architecture ensure this result while also reducing the system complexity. First, the upper and lower optical trains share common near-IR continuous-wave pumping lasers. These pumps or their AOM-shifted replicas become comb lines in each of the four near-IR combs. EO-combs therefore have identical center frequencies, while soliton combs have offset frequencies that are related by the difference in the AOM frequency shifts ($\Delta\nu_P$) applied to the soliton pumps. Second, by tuning the relative counter-pumping frequency $\Delta\nu_P$, the repetition rates of the two microcombs (f_r^{cw} and f_r^{ccw}) become phase locked such that $\Delta f_r = \Delta\nu_P/M$ ($\Delta f_r = f_r^{\text{cw}} - f_r^{\text{ccw}}$ and M is an integer) [95]. Because the EO-comb rates are derived from the soliton comb rates, all four combs, despite having different repetition rates, have their rates phase locked. This feature in combination with the common optical pumps means that the two mid-IR combs have an offset frequency noise equal to the fluctuations in the difference frequency of the $1.55 \mu\text{m}$ and $1.06 \mu\text{m}$ pumps as their primary source of frequency instability. Significantly, however, this is a common-mode fluctuation to the mid-IR combs and will therefore cancel out in the multi-heterodyne DCS detection process. As a result, the frequency stability of the mid-IR comb interferogram is extremely high, being primarily determined by the relative stability of the two CP solitons. This stability is accomplished without the need for frequency locking procedures, because of the above mentioned features of the system architecture.

To illustrate the frequency stability that is possible using this architecture, a portion of the Fourier transform of the measured dual-soliton interferogram (measured on a balanced receiver over 200 ms) is shown in Fig. 3.2(d). Defining the line-to-floor ratio (LFR) as the square root of the ratio of signal power to the average noise floor power, Fig. 3.2(e) shows that the highest LFR of the radio-frequency comb scales as $6.3 \times 10^4 \sqrt{\tau} / \sqrt{s}$ (τ is the measurement time). This value gives a measure of dynamic range available for absorption measurement. The mutual stability of the two microwave signals generated by photodetecting the soliton streams was also tested by mixing f_r^{cw} and f_r^{ccw} . The measured Allan deviation of their difference frequency Δf_r (Fig. 3.2(f)) shows that the two soliton microwave rates reach a relative frequency fluctuation less than 1 Hz at around a millisecond of averaging time. Then, the stability further improves to about 1 mHz at 100 s. This Allan deviation is found to be close to that of the frequency fluctuation of the AOM driver when setting its output frequency close to Δf_r (see Fig. 3.2(f)).

3.4 Characterization of the DCS system

The transfer of mutual coherence of the CP solitons to the mid-IR is verified in Fig. 3.3(a) where measured interferograms of the mid-IR combs are displayed. The mid-IR interferograms are collected by a fast photodetector (600 MHz bandwidth, PVI-4TE-4, Vigo System SA), and the optical power is around $60 \mu\text{W}$ to avoid detector nonlinearity. For comparison, interferograms are shown using conventional DFG (EO-comb drives turned off for soliton mixing with the $1.06 \mu\text{m}$ continuous-wave laser) as well as iDFG with $N=8$ and $N=16$. In the DFG case, interferogram pulses repeat at the rate of Δf_r , while in the iDFG case the pulses repeat at the rate of $\Delta f_r/N$. Note that even for the iDFG case, there are pulses appearing at the rate Δf_r and it is the envelope modulation of these pulses that reflects the interleaving process. This non-ideal behavior is mainly the result of three effects that could be corrected in the future. First, the EO-comb pulses themselves were not fully compressed (i.e., not transform limited), because of lack of a second dispersion control system. The Dual-EO-comb interferogram suggests the extinction ratio of the EO-pulses is about 8 dB. Second, based on the group refractive index difference and length of the commercial PPLN crystal, the temporal walk-off between two near-IR pulses is estimated to be up to ~ 4 ps. Third, the PPLN phase-matching bandwidth for this long crystal is quite narrow (< 300 GHz) at $1.5 \mu\text{m}$ and leads to an effectively wider soliton pulse width. A criterion for minimal residual pulses in iDFG can be given

as,

$$t_s + t_{\text{EO}} + |\Delta t_{\text{wkf}}| < T_s/N, \quad (3.1)$$

where t_s (t_{EO}) is the effective width of the soliton (EO) pulse, Δt_{wkf} is the walk-off between the near-IR pulses in the crystal, and T_s is the 1.55 μm soliton period. The use of fully compressed EO-combs in combination with a more optimal PPLN would eliminate the residual RF pulses in the interferograms. In such an optimized arrangement only one RF pulse would appear in the time period of $N/\Delta f_r$. This would also eliminate spectral envelope modulation in the interferogram FFT.

FFT of the interferograms yields the radio-frequency combs shown in Fig. 3.3(b). Digital correction (CoCoA method) [106] was used here to compensate fluctuations induced by fibres connecting comb generation and gas cell spectroscopy setups, which resided in different laboratories. Co-location of the setups to a single table (or ultimately integration of the components) should avoid this fluctuation and simplify data processing. In the spectra, the conventional DFG case has a line spacing of Δf_r , while the iDFG cases have a line spacing narrowed to $\Delta f_r/N$. Spectral envelope modulation appearing for $N=8$ and $N=16$ (compare to conventional DFG spectrum) results from the non-ideal residual pulses discussed in Fig. 3.3(a). A zoom in of the RF comb spectra in Fig. 3.3(c) shows the densification of the comb lines.

To measure the absolute frequency stability of the dual-comb interferogram spectra, the Allan deviation of a single multi-heterodyne beat frequency is calculated in Fig. 3.3(d) for mid-IR, CP and EO generated spectra. Using conventional DFG the frequency stability is comparable to that of the near-IR CP solitons. Here, the stability is better than 1 Hz within 100 ms averaging time as a result of stability linked to the single microcavity. A slight degradation is observed for the iDFG $N=8$ and iDFG $N=16$ cases, that may result from additional noise contributed by the EO-combs. This is substantiated in Fig. 3.3(d) by Allan deviation measurement of a single frequency within a multi-heterodyne spectrum produced using only two 1.06 μm EO combs.

To further confirm the mutual phase coherence in the mid-IR, the LFR of the mid-IR interferogram spectra (calculated using the strongest spectral peak) is analyzed in Fig. 3.3(e). In all three cases (DFG, iDFG $N=8$ and iDFG $N=16$), the LFR shows a $\sqrt{\tau}$ trend (after digital correction), and scales as $2.0 \times 10^4 \sqrt{\tau}/\sqrt{s}$, $6.8 \times 10^3 \sqrt{\tau}/\sqrt{s}$, and $4.0 \times 10^3 \sqrt{\tau}/\sqrt{s}$, respectively. Data obtained without digital correction (squares) for iDFG $N=8$ are also presented and show that the mutual coherence is preserved

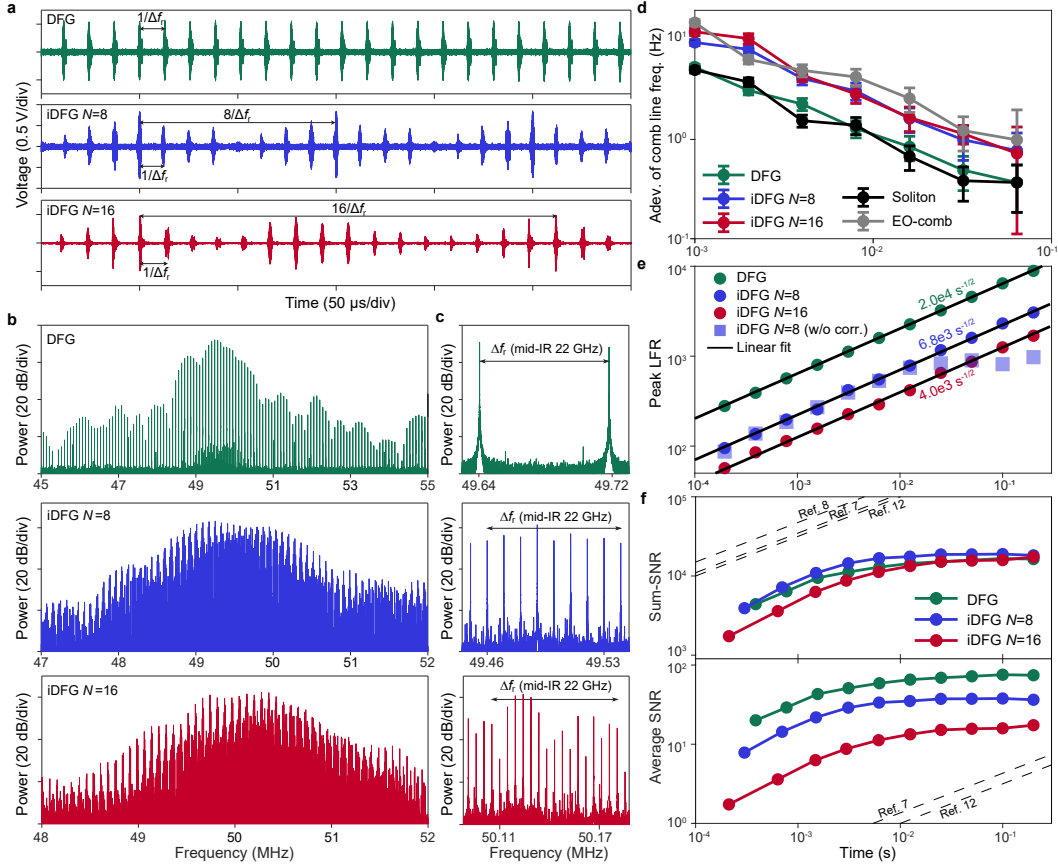


Figure 3.3: Interferograms and multi-heterodyne spectra of the iDFG densified mid-IR combs. (a) Interferogram of the mid-IR combs using DFG and iDFG. (b) Dual-comb spectra formed by fast Fourier transform of the measured interferograms. (c) Zoom-in of the radio-frequency combs in panel (b). (d) Allan deviation of the frequency of a single line measured at the center of the multi-heterodyne spectra plotted versus the measurement time. The error bar corresponds to the standard deviation of the Allan deviation. (e) Plot of the LFR versus measurement time τ for strongest spectral line using conventional and interleaved DFG. The solid lines are linear fits ($\sqrt{\tau}$ trend in the log-log plot). All circular points are digitally corrected. Squares points show the uncorrected results for $N=8$. (f) Plot of the sum- and average SNR of our mid-IR DCS system versus the measurement time τ . Black dashed lines are SNR for reported mid-IR DCS systems.

up to 10 ms until the aforementioned fibre fluctuations cause deterioration. The high LFR can enable high dynamic range spectroscopic measurements.

To further characterize the DCS system, the signal-to-noise ratio (SNR: square root of the ratio of the signal to the standard-deviation of the fluctuations)[84, 85, 91, 83, 78] of lines in the FFT of the interferogram is calculated. These values are then used to compute the sum-SNR (upper panel of Fig. 3.3(f)) and average

SNR (lower panel of Fig. 3.3(f)) versus integration time over lines within 40 dB of the strongest line[78]. The sum-SNR initially increases as $\sqrt{\tau}$ within 2 ms, but then saturates at longer averaging times. For comparison, the sum-SNRs for other reported mid-IR DCS systems are plotted as dashed lines. Considering the good frequency stability of the present system, the relatively low sum-SNR is likely limited by the amplitude noise of the mid-IR combs. It is possible that this could result from use of fibre-taper optical coupling to the resonator, which can introduce a mechanism for environmental noise to impact coupling. Use of a fully integrated microcomb would avoid this problem. Moreover, the use of a reference mid-IR photodetector would enable monitoring of power fluctuations [98] and could help to boost the sum-SNR. Although the sum-SNR is relatively low, the average SNR of the spectrum is relatively high and enables a fast measurement. This results from fewer usable lines in the current system compared with the fibre-based mid-IR systems.

3.5 Mid-IR DCS of methane and ethane

The mid-IR DCS system was used to measure the absorbance spectra of a mixture of methane and ethane gas. The dual-comb spectrum with the gas cell inserted (T) was first measured and then normalized by the reference spectrum measured without the gas cell (T_0). The absorbance is then calculated as $-\ln(T/T_0)$. The wavelength of the 1.06 μm laser (an external cavity diode laser) was tuned to access rovibrational transitions belonging to different branches in the ν_3 band of methane [107]. The Q -branch of methane around 3015 cm^{-1} was first measured. The absorbance spectra measured by DFG and iDFG $N=8$ DCS are presented in Fig. 3.4(a). We compare the measured spectra to the HITRAN database using the gas cell information given above (the absolute frequency offset was used as a free parameter for the best fit). While both absorbance spectra are in a good agreement with the HITRAN database [108] the DFG spectrum undersamples the methane spectral features due to its relatively wide 22 GHz comb line spacing, and only 3 data points (green points) appear for the zoom-in spectrum in Fig. 3.4(a). On the other hand, this spectral undersampling is avoided by using iDFG DCS with a reduced comb line spacing of 2.8 GHz corresponding to iDFG with $N=8$. The residuals between the measured spectrum and HITRAN database are plotted in the lower panel.

Additional data obtained for the P -branch of methane (e.g., $P(3)$, $P(6)$ and $P(7)$) are presented in Figs. 3.4(b, c). The measured spectra are also in good agreement with HITRAN database. The ethane absorption spectrum in the ν_7 band [109] was

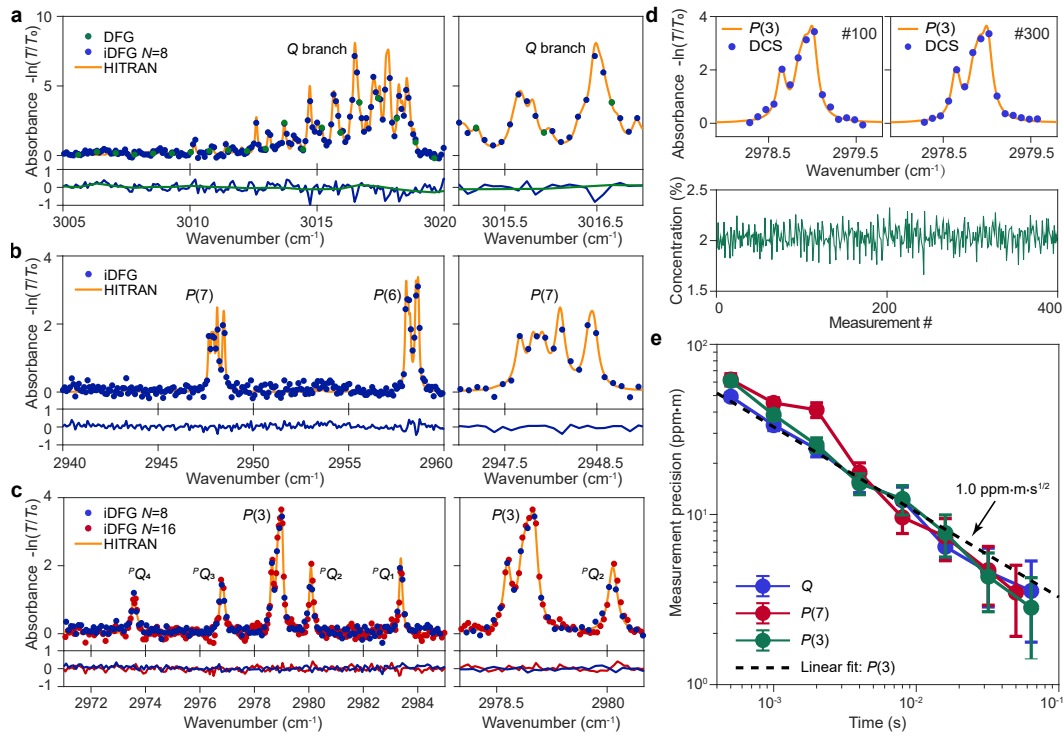


Figure 3.4: Dual-comb spectroscopy of methane and ethane mixture using iDFG mid-IR combs. (a) Absorbance spectrum for the methane ν_3 band Q branch using DFG and iDFG ($N=8$). iDFG improves the spectral resolution compared to the 22 GHz mid-IR generated by conventional DFG. HITRAN data indicated by the yellow line. The right panel (and in (b, c)) is a zoom-in of absorption features. The ‘observed-HITRAN’ residuals are shown in the lower panel (also in (b, c)). (b) DCS absorbance spectrum of the methane $P(6)$ and $P(7)$ branches in the ν_3 band measured using iDFG with $N=8$. (c) Absorbance spectrum of the methane $P(3)$ branch in the ν_3 band together with the ethane rovibrational transitions in the ν_7 band. Since ethane has a narrower absorption linewidth, iDFG with $N=16$ was also used to further improve the spectral resolution. (d) Top panels are DCS spectra of the methane $P(3)$ branch (iDFG $N=8$), each measured over 0.5 ms duration within a 200 ms measurement window. 100th and 300th spectra of 400 total are displayed. Fitting the spectrum to the HITRAN database yields the methane concentration. The lower panel plots the concentration for the 400 time slots. (e) Normalized measurement precision of methane concentration evaluated by Allan deviation using different rovibrational transitions belonging to different branches with iDFG $N=8$. The error bar corresponds to the standard deviation of the Allan deviation. The Allan deviation of the measured concentration (e.g., lower panel in (d)) is calculated and normalized to a 1 m optical path. The precision scales nearly as $1/\sqrt{\tau}$ and the dashed line is the corresponding linear fit using a $1/\sqrt{\tau}$ trend line (log-log) for the $P(3)$ branch. A precision of $1.0 \text{ ppm}\cdot\text{m}\cdot\sqrt{\text{s}}$ is fitted.

also measured in Fig. 3.4(c). Such an ability to measure the methane and ethane simultaneously is important to distinguish if the methane emission comes from gas wells [110].

A feature of iDFG DCS is that the spectral resolution can be adjusted by changing the division ratio N . For instance, the full-width at half-maximum (FWHM) of methane $P(3)$ to $P(7)$ transition groups in the ν_3 band are within 10 GHz to 26 GHz, while the FWHM of ethane PQ_1 to PQ_4 transitions in the ν_7 band are within 4.2 GHz to 6.9 GHz according to the HITRAN database. Improved resolution of the ethane absorbance via iDFG DCS in the ν_7 band (which features narrower absorption in comparison to methane) is shown as the red dots in Fig. 3.4(c). Here, a finer resolution of 1.4 GHz is achieved by selecting $N=16$. In principle, the resolution of the DCS system could be adjusted in steps from GHz to 22 GHz, making it possible to optimize resolution and SNR depending upon the characteristics of the gas sample.

The GHz DCS system also enabled fast and precise measurement of the absorbance spectrum. Measurement precision is evaluated using the Allan deviation of the measured methane concentration in the 5 cm cell. 200 ms interferograms were separated into 400 slots and the methane concentration was calculated in each resulting 0.5 ms slot (corresponding to about 5 interferogram periods for iDFG $N=8$). Figure 3.4(d) details the evaluation process for the $P(3)$ branch measurement with iDFG $N=8$. The top panels are representative spectra from two 0.5 ms time slots (numbers 100 and 300) without any digital correction as mutual coherence is preserved. They illustrate fast acquisition of the methane absorption spectrum, which can result from the relative high average SNR achieved in short time.

Fitting each absorbance spectrum to the HITRAN database yields the measured methane concentration in each time slot (lower panel of Fig. 3.4(d)). Since about 20~30 comb lines in the absorption spectra are used to fit for the concentration, the residuals between the observation and HITRAN are found to not significantly degrade the measurement precision. This measured concentration sequence was then used to calculate the Allan deviation of the measured methane concentration, which was further normalized by the gas cell length to derive the normalized measurement precision in Fig. 3.4(e) (all for the iDFG $N=8$ case). The Allan deviation ($P(3)$ branch measurement) reaches a precision of ~ 2.8 ppm·m within 64 ms. In fitting the Allan deviation of the $P(3)$ branch measurement to a $1/\sqrt{\tau}$ trend line, a normalized measurement precision of 1.0 ppm·m· \sqrt{s} can be obtained. Measurements

of rovibrational transitions in other branches produce similar results. This sub-ms measurement time may make this system suitable for studies of transient events in combustion [111].

The measurement acquisition times of 200 ms for Figs. 3.4(a, c) and 100 ms for Fig. 3.4(b) are shorter than for fibre-comb based mid-IR DCS systems, which generally require an acquisition time longer than tens of seconds [84, 87, 88] (usually those systems have a much larger comb line number). Even shorter acquisition times should be possible that are comparable to EO-comb based systems, where mid-IR DCS has also been demonstrated [91]. To attain shorter acquisition time, CP solitons with a larger Δf_r generated on distinct mode families could be utilized [112].

3.6 Discussion

We have demonstrated microcomb-based DCS in the mid-IR with GHz resolution. This represents a 100-fold improvement in spectral resolution compared with previous mid-IR microcomb DCS. Mutual coherence of near-IR CP solitons enables precise methane absorption measurements reaching a normalized precision of $1.0 \text{ ppm}\cdot\text{m}\cdot\sqrt{\text{s}}$. While the demonstrated system still relies upon fibre optics, further integration of the system on a photonic chip is feasible. Along this direction, both near-IR combs as well as the DFG crystal can potentially be monolithically or hybridly integrated in the future. Using solitons as opposed to EO-combs can offer higher peak power and therefore more efficient iDFG. However, their application for iDFG may also limit the rate reconfigurability. EO-combs could also be integrated to retain this reconfigurability. Also, cavity enhanced DCS [113] can be used to further increase the measurement sensitivity for the proposed mid-IR chip-based sensor (folding of the light path will be needed to reduce the footprint of the GHz enhancement cavity).

Moreover, rapid progress in the overall subject of microcomb systems should ultimately address gaps in the current platform required for complete integration. Such photonic integration can bring opportunities to improve the system performance. For example, the tight mode confinement of on-chip PPLN waveguides can allow dispersion engineering to achieve more optimal phase-matching for increased broadband spectral coverage in the mid-IR [114]. Tight mode confinement can also increase the conversion efficiency. Ultimately, integration of the DCS system would enable miniature (potentially hand-held) gas sensors with high resolution capability for detection of gases in a cluttered environment. Such a robust sensor technology

would be suitable for widespread spectroscopy applications in laboratories and field measurements.

SOLITON PULSE PAIRS AT MULTIPLE COLORS IN NORMAL DISPERSION MICRORESONATORS

4.1 Introduction

¹ Soliton microcombs are helping to advance the miniaturization of a range of comb systems. They exist through a balance of optical nonlinearity and dispersion, which must be anomalous for bright soliton generation [19, 20, 26]. Moreover, microresonators must feature high optical Q factors for low pump power operation of the resulting microcomb. While these challenges have been addressed at telecommunications wavelengths using a range of material systems [19], ultra-low-loss Si_3N_4 resonators (introduced in section 2.2) [66, 67] do not yet support bright solitons as their waveguides feature normal dispersion [66]. Furthermore, all resonators are dominated by normal dispersion at shorter wavelengths. While it is possible to form normal dispersion combs [116], the temporally-short pulse nature and highly reproducible spectral envelopes of anomalous dispersion soliton combs [19] has generated keen interest in methods to induce anomalous dispersion for bright soliton generation in normal dispersion systems. Such methods have in common the engineering of dispersion through coupling of resonator mode families, including those associated with concentric resonator modes [117, 118], polarization [119, 61] or transverse modes [120, 121]. As an aside, such coupled resonators have also been used to improve normal dispersion comb formation [122, 123] and to boost the power efficiency of bright combs [124].

Here, we engineer anomalous dispersion in ultra-low-loss Si_3N_4 resonators by partially-coupling resonators as illustrated in Fig. 4.1(a). This geometry introduces unusual new features to bright soliton generation. For example, spectra resembling single soliton pulse microcombs form instead from coherent pulse pairs (Fig. 4.1(a)). The pulse pairs circulate in a mirror-image fashion in the coupled rings to form coherent comb spectra (Fig. 4.1(b)) with highly stable microwave beat notes (Fig. 4.1(c)). Unlike conventional microcombs, pulses in this system cannot exist alone, and instead phase lock in pairs wherein pulses in each pair feature different optical spectra. The interaction of the pulses in the coupling section between the

¹Work presented in this chapter has been published in [115] “Soliton pulse pairs at multiple colors in normal dispersion microresonators.” *Nature Photonics* 610.11 (2023), pp. 977–98.

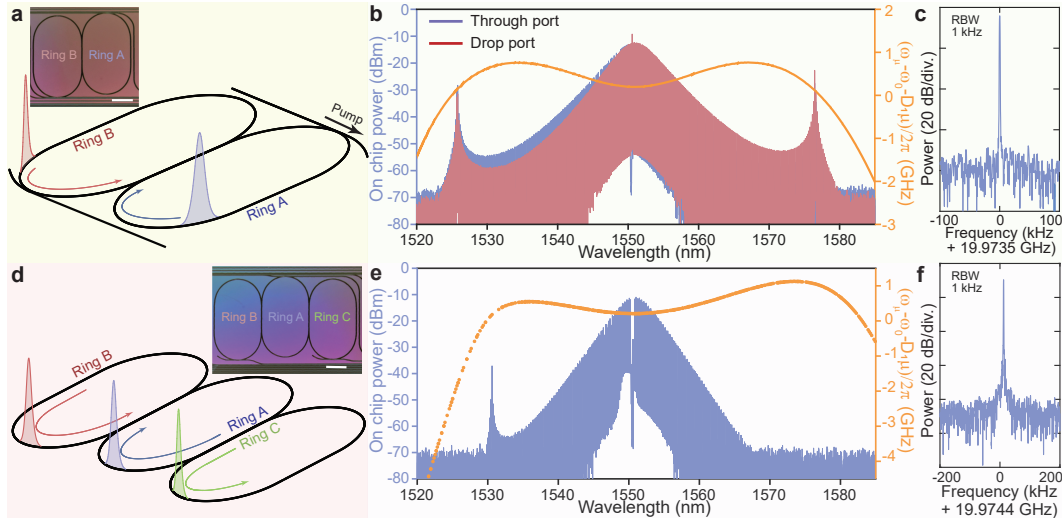


Figure 4.1: **Soliton pulse pair generation in two- and three-coupled-ring microresonators.** (a) Schematic showing coherent pulse pairs that form a composite excitation. Inset: Photomicrograph of the two-coupled-ring resonator used in the experiments. Rings A and B are indicated. The scale bar is 1 mm. (b) Simultaneous measurement of optical spectra collected from the through port (pumping port) and drop port in the coupled-ring resonator of panel (a). The measured mode dispersion is also plotted. Two dispersive waves are observed at spectral locations corresponding to the phase matching condition as indicated by the dispersion curve. (c) Radiofrequency spectrum of microcomb beatnote (RBW: resolution bandwidth). (d) Illustration of 3 pulse generation in a three-coupled-ring microresonator wherein pulses alternately pair. Inset: Photomicrograph of the three-coupled-ring microresonator used in the experiments. The scale bar is 1 mm. (e) Measurement of optical spectrum of the three pulse microcomb. The measured mode dispersion is also plotted. The pump laser wavelength is several nanometers away from the anomalous dispersion center frequency, and, as a result, the spectrum features only one dispersive wave at the shorter wavelength side. (f) Radiofrequency spectrum of the microcomb beatnote.

rings is shown to induce anomalous dispersion that compensates for the overall normal dispersion of each ring. This pairwise compensation spectrally recurs thereby opening multiple anomalous dispersion windows for the formation of multi-color soliton pairs. These windows can be engineered during resonator design. Furthermore, the spectral composition of each pulse in a pair is different. Fig. 4.1(b), for example, shows through-port and drop-port spectra that reflect the distinct spectral compositions of pulses in ring A and ring B of Fig. 4.1(a). This peculiar effect is also associated with Dirac solitons [125] and it is shown that the 2-ring pulse pair represents a new embodiment of a Dirac soliton as the underlying dynamical equation resembles the nonlinear Dirac equation in 1 + 1 dimensions. Pulse pairing

is also extendable to higher-dimensional designs with additional normal dispersion rings. For example, in Fig. 4.1(d-f), 3 pulses in 3 coupled rings alternately pair to compensate for the normal dispersion of each ring. In presenting the results, it is convenient to resolve the ambiguity created by pulse-pair spectra in 2 and 3 coupled rings that nonetheless resemble single-pulse soliton spectra. To accomplish this, we denote these cases as bipartite and tripartite soliton microcombs, respectively. The need for such nomenclature is made clear by the demonstration of multiple pulse-pair states, including a 2-ring microcomb state containing 4 pulses that behaves as a 2-pulse soliton crystal, and a 3-ring state with 12 pulses that behaves as a 4-pulse soliton crystal [126].

Moreover, due to recurring spectral windows, pulse pairs can also form at different wavelength bands. The ability to generate multi-color pulse pairs over multiple rings is an important new feature for microcombs. It can extend the concept of all-optical soliton buffers and memories to multiple storage rings that multiplex pulses with respect to soliton color and that are spatially addressable. The results also suggest a new platform for the study of topological photonics and quantum combs.

4.2 Recurring spectral windows

Before addressing pulse pair propagation in the 2-ring and 3-ring systems, the conventional mode-family coupling approach is considered [117, 61, 118]. As a representative example, the case of a concentric resonator system is chosen as illustrated in the upper left panel of Fig. 4.2(a). The characteristics of this system are identical to other methods. First, a phase matching condition must be satisfied such that the absolute mode number of each ring (or each coupled mode) must be equal at the same optical frequency. This mode number determines the wavelength where soliton formation is possible. Second, the free-spectral-range values, FSR_A and FSR_B , of the uncoupled mode families of ring A and ring B must be close in value compared to their average $FSR = (FSR_A + FSR_B)/2$ so that phase matching occurs over a large number of modes. With these conditions satisfied, the resulting dispersion will be as illustrated schematically in the lower panel of Fig. 4.2(a) (green curves). Comparison to the uncoupled dispersion curves (center dashed blue and red lines) shows that anomalous dispersion is possible for the upper mode family branch.

Next, consider the case where two rings are placed side-by-side and coupled together as illustrated in the upper right panel of Fig. 4.2(a). The two ring cavities differ only

in length, with ring B slightly longer than ring A so that $FSR_A > FSR_B$. Considering the straight coupling section from a coupled-mode perspective, modes of the two rings will strongly couple if they have matching wavevectors (or equivalently, resonance frequencies), while there are no requirements on mode number matching of the rings (i.e., mode number is not conserved). In comparison to the concentric ring configuration, this dramatically modifies the dispersion relation as illustrated in the lower panel in Fig 4.2(a), where the orange curves give the resulting dispersion. Due to the loss of mode number conservation, inter-ring coupling pushes the resonance frequencies away from that of the individual rings (blue and red dashed lines) at all frequency degeneracies, so that recurring anomalous dispersion windows with period $M = FSR / (FSR_A - FSR_B)$ now appear in the spectrum. These result from spectral folding that occurs because of the frequency Vernier between the cavity resonances. As an aside, because mode number is not conserved, modeling of this dispersion proceeds differently relative to the standard coupled-mode family approach.

4.3 Dispersion measurements and soliton pulse pair generation

2-ring and 3-ring resonators consist of thin, single-mode Si_3N_4 waveguides (see optical images in Fig. 4.1(a) and 4.1(d) insets). For the coupled 2-ring device, the circumference of ring A is 9.5 mm ($FSR \sim 20$ GHz) and ring B is 0.5% longer than ring A. For the 3-ring device, the rightmost ring has a circumference of 9.5 mm, and each other ring is 0.3% longer than its right neighbor. The rings feature high intrinsic Q factors exceeding 75×10^6 . Individually, each ring does not support bright soliton formation around 1550 nm due to the strong normal dispersion associated with the low confinement waveguide structure.

The measured frequency dispersion (green points) for the 2-ring system with comparison to theory (solid lines) is shown in Fig. 4.2(b). The measurement is performed using a radio-frequency calibrated interferometer in combination with a wavelength-tunable laser [26]. The coupled resonators feature two frequency bands in which three anomalous dispersion windows are highlighted. At each window, soliton steps are observed when scanning the laser frequency over a cavity resonance. Zoom-in views of the steps are presented as insets in Fig. 4.2(b). Operation at the longest and shortest wavelength windows (1584.5 nm and 1525.5 nm) was challenging due to low laser power, and as a result the time duration of the soliton steps for these wavelengths is relatively shorter.

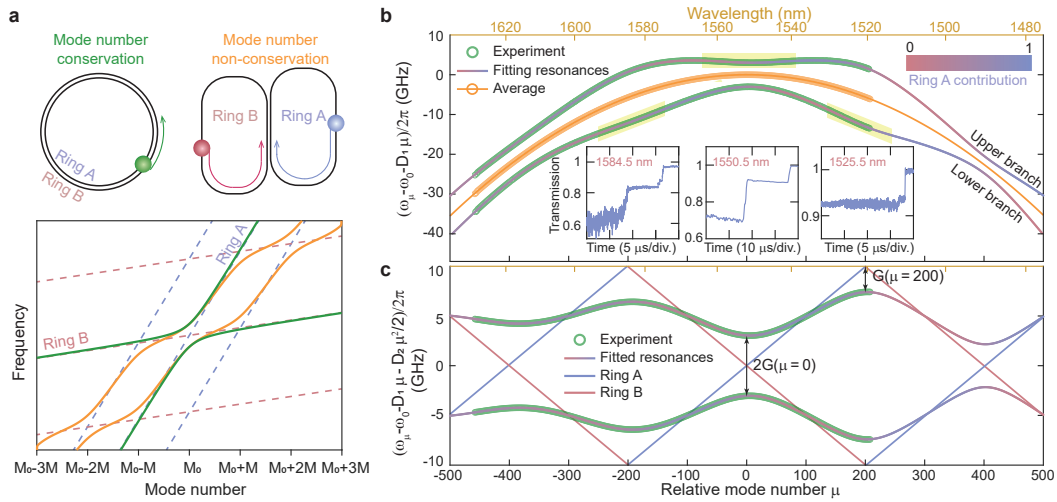


Figure 4.2: Mode number non-conservation coupling and dispersion for bright soliton formation. (a) Dispersion properties for two resonator coupling schemes. Concentric rings (upper left panel) induce coupling wherein mode number is conserved. The center blue and red dashed lines (lower panel) represent the resonance frequencies of the coupled rings having slightly different FSRs. A single coupling-induced gap is opened at their intersection (mode number M_0) corresponding to phase matching of the concentric ring modes. Two hybrid mode branches are thereby created (green curves) with a single anomalous dispersion window. In this work (top right panel), inter-ring coupling occurs from resonance frequency matching instead of mode number matching (i.e., mode number is not conserved). In contrast to the concentric case, dispersion is altered at all frequency degeneracies. Spectral folding (allowed by non-conservation of mode number) is illustrated by the multiple dashed lines (lower panel) and induces multiple gaps. These recur with period M (set by the Vernier in the FSRs) creating multiple anomalous dispersion windows. (b) Measured frequency dispersion of the coupled resonator (green circles) versus relative mode number μ . Here $D_1/(2\pi) = 19.9766$ GHz, and ω_0 is chosen so that $\mu = 0$ is at the crossing center (1552.3 nm). Multiple anomalous dispersion windows appear around $\mu = 0$ and 400 for the upper branch and $\mu = -200$ and 200 for the lower branch. The anomalous dispersion windows near $\mu = -200, 0$ and 200 have been highlighted. The average of the upper and lower branch mode frequencies is plotted as orange circles and fitted by a second-order dispersion model (orange curve, described by Eq. 4.1). Inset: transmission observed when scanning a laser over resonances in the anomalous dispersion windows. Soliton steps are observed around $\mu = -200, 0$ and 200. (c) Measured relative frequency dispersion of the coupled resonator (green circles) versus relative mode number μ . Here $D_2/(2\pi) = -283.0$ kHz, and other parameters are the same as panel b. Solid curves are the theoretical fittings described by Eq. (4.2). Fitted mode frequency dispersion diagrams of the single rings without coupling are shown as red and blue lines.

Analysis shows that the average frequency of the two bands (i.e., $\omega_\mu \equiv (\omega_{\mu,+} + \omega_{\mu,-})/2$) is given by the mode frequency for a length-averaged resonator at the same mode number. This average frequency can be described by a second-order dispersion model:

$$\omega_\mu \approx \omega_0 + D_1\mu + \frac{1}{2}D_2\mu^2, \quad (4.1)$$

where ω_0 is the mode frequency at $\mu = 0$ and μ is a relative mode number referenced to the frequency degeneracy at 1552.3 nm. D_1 is the length-averaged FSR for the resonator at $\mu = 0$, $D_2 = -cD_1^2\beta_2/n_g$ is the second-order dispersion parameter at $\mu = 0$ with group velocity dispersion β_2 and waveguide group index n_g . Averaging the frequencies removes the effect of the coupling entirely, and the resulting average dispersion (orange points in Fig. 4.2(b)) closely matches a parabolic-shaped dispersion curve (orange curve).

The effect of the coupling is made clearer by plotting the mode frequencies relative to the averaged frequency (i.e., relative mode frequency $\omega_{\mu,\pm} - \omega_\mu$) as shown in Fig. 4.2(c). The relative mode frequencies of uncoupled rings appear as straight lines. Their positive and negative slopes result from removing a linear component of dispersion in this plot given by the average FSR, D_1 . Mode number walk-off causes the lines to vertically wrap at $\pm D_1/2$. Because the length of ring B is 0.5% longer than ring A, frequency degeneracy of the rings occurs every 200 ring A modes (or every 201 ring B modes). The introduction of coupling opens gaps at frequency degeneracies, regardless of whether the absolute mode number is matched.

Analysis shows that the gap widths equal $2G \equiv g_{co}L_{co}D_1/\pi$ where g_{co} is the coupling strength per unit length and L_{co} is the effective coupler length. The full dispersion relation is [115]:

$$\omega_{\mu,\pm} = \omega_\mu \pm \frac{D_1}{2\pi} \arccos [\cos(g_{co}L_{co}) \cos(2\pi\epsilon\mu)], \quad (4.2)$$

where $\epsilon = (L_B - L_A)/(L_B + L_A) = (2M)^{-1}$ is the length contrast of the rings, and L_A (L_B) is the length of ring A (B). For the current design $\epsilon = 1/401$, and the gap is modulated with respect to mode number with period $\epsilon^{-1} = 401$ (corresponding to 8 THz in the spectrum). The small length contrast ϵ guarantees the wide spectral range of the anomalous dispersion window. Overall, there is very good agreement between the model and the measured data in Fig. 4.2(b) and Fig. 4.2(c), and the fitting allows determination of key resonator parameters (see figure caption). The fractional energy contribution from ring A is used to color the hybrid modes in Fig. 4.2(b, c).

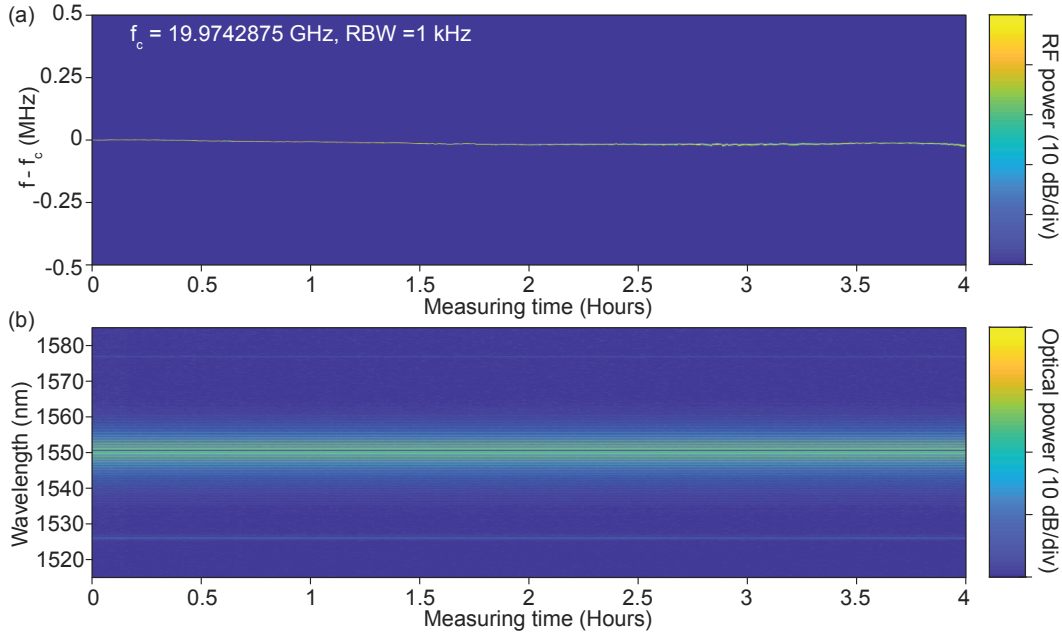


Figure 4.3: Stable soliton operation in the two-ring resonator measured over 4 h. (a) Continuous measurement of the RF beat note of a pulse pair soliton microcomb over 4 h. The RF beatnote peak drift over 4 h is within 25.7 kHz (1.29 PPM). f : RF frequency, f_c : centre RF frequency, RBW: resolution bandwidth. (b) Simultaneous measurement of the optical spectrum of the pulse pair soliton microcomb in a over 4 h.

As an aside, the spectral gap is smaller at larger mode numbers, which is attributed to the wavelength dependence of g_{co} , as shorter wavelength results in stronger mode confinement, and hence smaller coupling with the adjacent waveguide. When combined with the original normal dispersion of each ring, the net dispersion for coupled system remains anomalous around $\mu = 0$ and 400 for the upper branch and around $\mu = -200$ and 200 for the lower branch.

Besides the observation of soliton steps, soliton was stabilized by measuring comb power from the through port and feeding back to the pump laser frequency (section 2.3). The microcomb spectra measured around 1550 nm for through port (ring A) and drop port (ring B) are presented in Fig. 4.1(b). The comb exhibits excellent stability and measurements of comb spectra and repetition rate over 4 hours of operation are provided in Fig. 4.3. The theoretical pulse width of the comb spectra in the figure is estimated to be ~ 250 fs. Microcomb spectra measured at other pump-cavity offset frequencies, and using another device are presented in Fig. 4.4. Comb coherence and soliton pulse behavior were confirmed in several ways. The radio-frequency spectrum of the soliton beatnote is presented in Fig. 4.1(c).

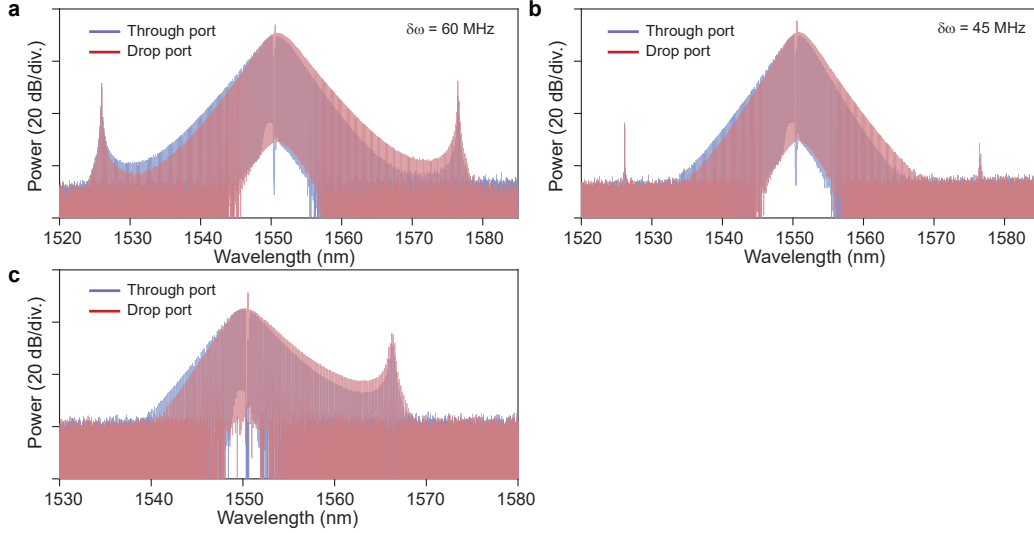


Figure 4.4: **Additional optical spectra of the solitons in the two-ring coupled resonator.** (a, b) Soliton optical spectra in two-ring coupled resonator at different pump laser detunings ($\delta\omega$), for comparison to the optical spectra in Fig. 4.1(b) (where $\delta\omega = 75$ MHz). (c) Soliton pulse pair optical spectra generated in another device wherein the coupling centre wavelength is several nanometres away from the pump laser wavelength. As a result, the spectra feature only one dispersive wave on the longer wavelength side.

Comb generation in the 3-ring system is shown in Fig. 4.1(d). Fig. 4.1(e) shows the soliton spectrum measured from the center ring. The measured dispersion is also included in the figure. The pump laser wavelength is several nanometers away from the anomalous dispersion center frequency, and, as a result, the spectrum features only one dispersive wave at the shorter wavelength side. The radio-frequency spectrum of the soliton beatnote is presented in Fig. 4.1(f), indicating good coherence.

Through port and drop port spectra correspond to pulses in ring A and ring B, and show that these pulses are both different from each other and deviate from the conventional sech^2 shape of Kerr solitons. The through port spectrum is stronger (weaker) than the drop port at shorter (longer) wavelengths. This is a result of this system representing a new version of the Dirac soliton [125] as discussed in the Methods section. In Fig.4.1(b), two strong dispersive waves (DWs) are observed near 1526 nm and 1577 nm where modes of the coupled resonator phase-match to the soliton comb. For comparison, the dispersion in the vicinity of the comb spectrum is overlaid in the figure. The DWs broaden the soliton spectrum and provide higher power comb lines (1.5 μW on-chip power at shorter wavelength and 5.4 μW at longer wavelength), which is advantageous for application to optical

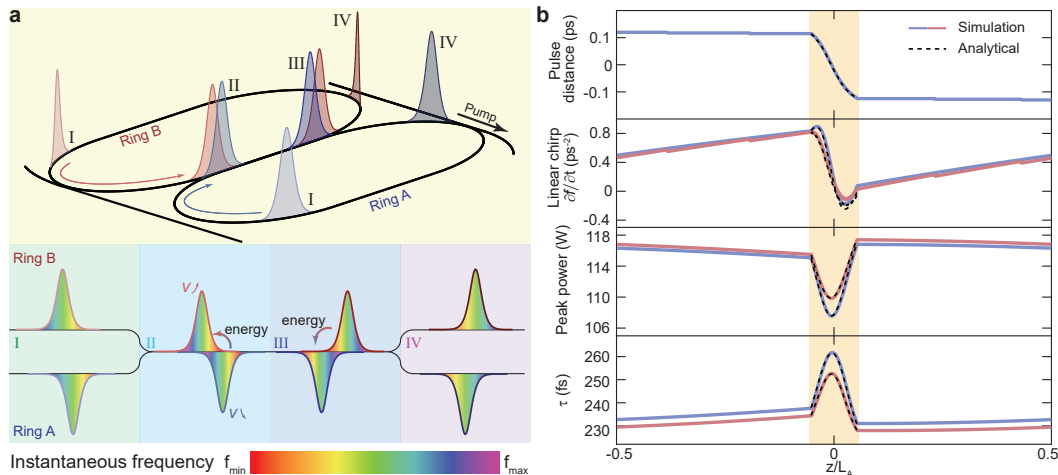


Figure 4.5: Temporal evolution of the soliton pulse pair in the two-ring coupled resonator. (a) Upper panel: Illustration of the time evolution of the soliton pair inside the two rings during one round trip time. Lower panel: Snapshots of the pulses at different positions. In the non-coupled regions (I and IV), pulses accumulate positive chirp due to nonlinearity and normal dispersion of the waveguide. Pulse in ring A is leading in time at I due to shorter ring circumference. When the pulses enter the coupling region (II), the pulses exchange energy, which leads to relative position shifts as well as chirp compensation (III). The pulses exit the coupled region (IV) with position shifts and chirping compensated. (b) Simulated pulse pair properties are plotted versus pulse position in each ring during one round trip. The two rings are aligned at the coupling region center, and the surplus length in ring B is omitted in the figure. The yellow shaded area represents the coupling region. The quantities are, from top to bottom: pulse timing difference (pulse center-to-center), linear chirp, peak power, and theoretical pulse width τ . The blue (red) lines represent simulation results for the pulse in ring A (B). The dashed lines are analytical results from a linear coupling model, and are consistent with simulation results.

frequency division [9].

4.4 Pulse pairs and multi-partite states

Both autocorrelation measurements and simulations show that microcombs form as phase-locked pulse pairs where the pulses have opposite phases. The pair viewpoint provides a powerful framework for visualization of mode locking that readily explains observable multi pulse-pair states and higher dimensional systems comprising multiple coupled cavities.

Simulations of pulse propagation in the 2-ring system are presented in Fig. 4.5(a). Here, the ring FSRs and couplings are those of the experimental system studied in Fig. 4.2(b,c), and excitation occurs for the mode $\mu = 0$. As shown in Fig. 4.5(b),

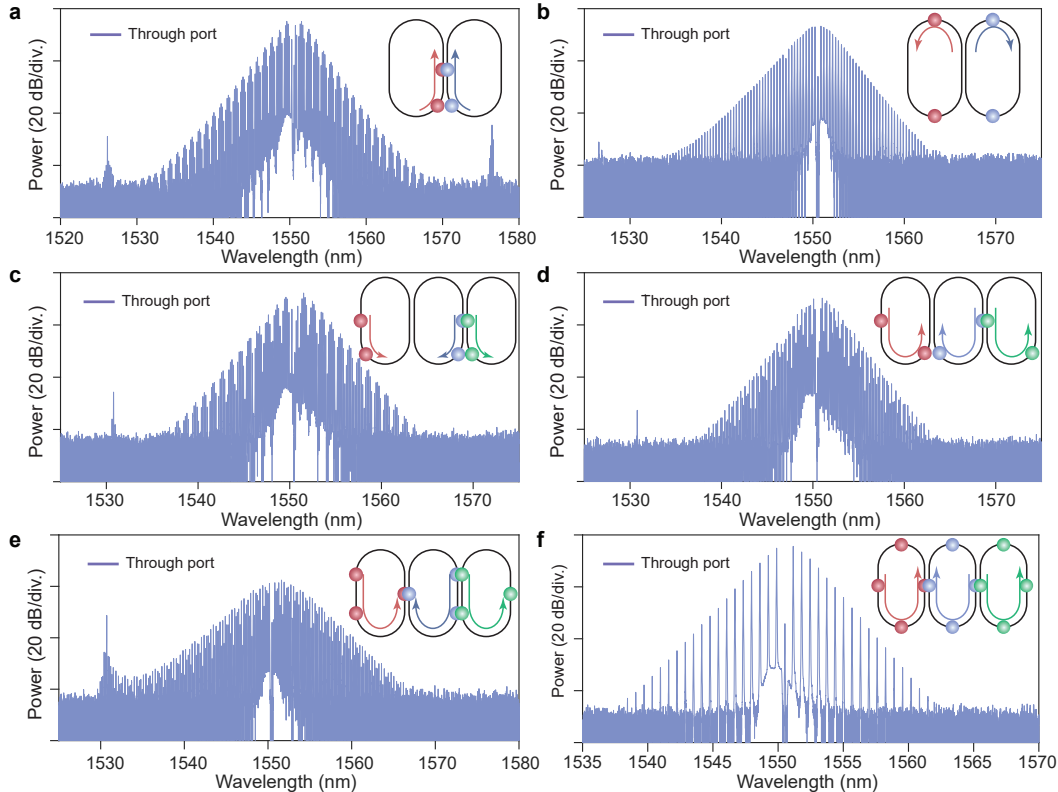


Figure 4.6: Observation of bipartite and tripartite multi soliton states in two- and three-coupled-ring microresonators. (a, b) Through port optical spectra of bipartite two-soliton states with different relative soliton positions. The state in panel (b) is a two-soliton crystal state. Insets: relative position of the two solitons inside each microresonator. (c, d) Through port optical spectra of tripartite two-soliton states with different relative positions. Inset: relative position of the two solitons inside each microresonator. (e) Optical spectrum of a tripartite three-soliton state. Inset: relative position of the three solitons inside each microresonator. (f) Optical spectrum of a tripartite four-soliton crystal. Inset: relative position of the four solitons inside each microresonator.

each pulse undergoes shape, chirp, and pulse width variations that repeat upon each round trip. Before entering the coupling region (point I in Fig. 4.5(a)), the chirp of both pulses has increased due to uncompensated Kerr nonlinearity from propagation in normal dispersion waveguides of each ring. Pulse chirp is indicated in the lower panel of Fig. 4.5(a), where the color represents instantaneous frequency. The pulse in ring B (red) also lags behind its counterpart in ring A (blue) due to the difference in ring lengths. However, upon entering the coupling region (point II), the ring B (A) pulse accelerates (decelerates) and becomes the leading (lagging) pulse when exiting the coupling region (point III). The chirp of both pulses decreases through

the coupling region. Upon exiting the coupling region, the pulses propagate in their respective waveguides (point IV) where chirp increases as the pulses circle back through point I. Detailed numerical simulations (see section 4.6) are used to further explore and confirm the pulse pair evolution (see Fig. 4.5(b)).

This picture of pairwise round-trip compensation of normal dispersion explains how compensation works for multi-pair systems as well as for higher dimensions with additional ring cavities. Specifically, it constrains how comb states form. For example, consider the coupled-ring states in Fig. 4.6(a,b) wherein 2 pulse pairs circulate in a mirror-image like fashion to form the observed spectra. Here, to reduce confusion with corresponding multi-pulse soliton systems, we adopt the nomenclature that a single pulse pair in a 2 ring system is a bipartite single soliton (see Fig. 4.1(a,b)), while multi-pair states in the same are bipartite multi soliton systems. Accordingly, the states in Fig. 4.6(a,b) are bipartite 2 soliton states. The state in Fig. 4.6(b) is moreover a bipartite 2-soliton crystal. Autocorrelation characterization for this bipartite crystal state is presented in Fig. 4.7 for comparison to single pulse pair state in the same figure. Notice that the requirements imposed on pulse pairing allow a one-to-one correspondence between conventional multi-soliton states and bipartite states, since the pulse configurations in each ring resonator mirror image the neighboring ring.

The same is true for higher dimensional systems. For example, three pulses compensate normal dispersion by alternating their pairwise coupling as illustrated in Fig. 4.1(d). Moreover, the pairwise compensation works when additional pulses are added to each cavity. For example, measurement of tripartite 2 soliton, 3 soliton and a 4 soliton crystal state (containing respectively 6, 9, and 12 pulses) are presented in Fig. 4.6(c-f). Notice that the measured comb line spacing (79.93 GHz) for the crystal state is four times the FSR of a single ring as is consistent with a conventional 4 soliton crystal state. Backscattering inside the cavity and coupling to the external waveguide might contribute to this self-organization behaviour.

4.5 Additional measurements

To confirm the short pulse nature of the generated pulse pairs, the soliton S -resonance and C -resonance [127, 128] were measured using a vector network analyzer. Plots of their relative frequencies versus laser-cavity detuning are given in Fig. 4.7(a). Finally, time domain autocorrelation measurements are also given in Fig. 4.7.

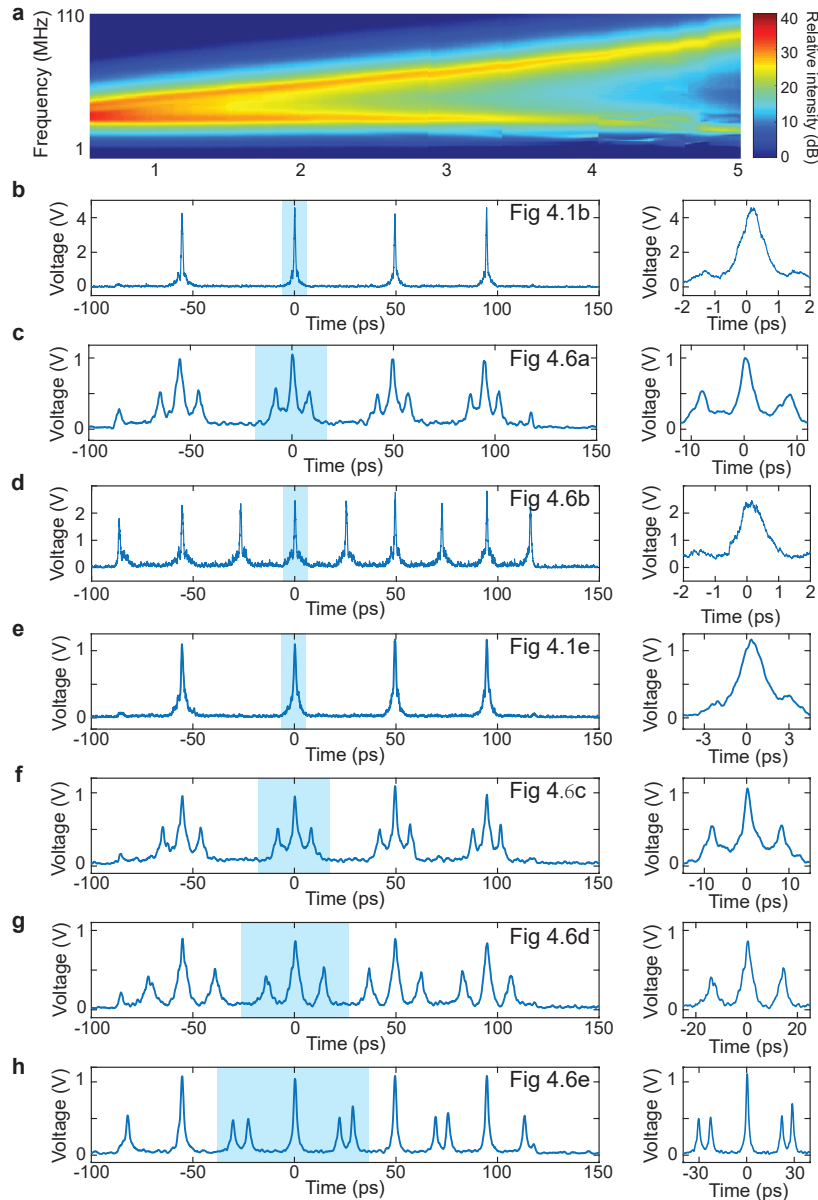


Figure 4.7: *C* and *S* resonances and autocorrelation measurements of solitons in the coupled-ring resonator. (a) The relative frequency of the *C* and *S* resonances are measured using a vector network analyzer and plotted versus tuning voltage in the two-ring resonator. (b-h) Experimental autocorrelation measurements of: (b) single soliton state in a two-ring resonator (state in Fig. 4.1(b)); (c) two soliton state in a two-ring resonator (state in Fig. 4.6(a)); (d) two soliton crystal state in a two-ring resonator (state in Fig. 4.6(b)); (e) single soliton state in a three-ring resonator (state in Fig. 4.1(e)); (f) two soliton state in a three-ring resonator (state in Fig. 4.6(c)); (g) two soliton state in a three-ring resonator (state in Fig. 4.6(d)); (h) three soliton state in a three-ring resonator (state in Fig. 4.6(e)). The resolution of the autocorrelation setup is 100 fs. The zoom-in of each autocorrelation measurements are shown in corresponding right panel.

4.6 Dynamics and numerical simulations of the soliton pulse pair

The optical fields in the two rings are governed by the coupled nonlinear wave equations:

$$\begin{aligned} \frac{\partial E_A}{\partial t} = & - \left(\frac{\kappa}{2} + i\delta\omega_A \right) E_A - v_g \frac{\partial E_A}{\partial z} - i \frac{\beta_2 v_g^3}{2} \frac{\partial^2 E_A}{\partial z^2} \\ & + i g_{\text{co}} v_g \chi_{\text{co}}(z) E_B + i g_{\text{NL}} |E_A|^2 E_A + F \end{aligned} \quad (4.3)$$

$$\begin{aligned} \frac{\partial E_B}{\partial t} = & - \left(\frac{\kappa}{2} + i\delta\omega_B \right) E_B - v_g \frac{\partial E_B}{\partial z} - i \frac{\beta_2 v_g^3}{2} \frac{\partial^2 E_B}{\partial z^2} \\ & + i g_{\text{co}} v_g \chi_{\text{co}}(z) E_A + i g_{\text{NL}} |E_B|^2 E_B \end{aligned} \quad (4.4)$$

accompanied by periodic boundary conditions in the z direction, where $E_{A,B}$ denotes the optical field in the two rings normalized to photon numbers in the corresponding length-averaged ring, $\kappa = \kappa_0 + \kappa_{\text{ex}}$ is the loss rate (sum of intrinsic and external loss) for the individual rings (assumed to be identical for ring A and B). Also, $\delta\omega_{A,B} = \omega_{0A,B} - \omega_p$ is the pump laser detuning, $v_g = c/n_g$ is the group velocity of the waveguide, $z \in [0, L_{A,B})$ is the resonator coordinate with $L_{A,B}$ the ring length, β_2 is the waveguide group velocity dispersion, g_{co} is the coupling strength between the two waveguides in the coupling region, $\chi_{\text{co}}(z)$ is the indicator function with value 1 in the coupling region and 0 elsewhere, $g_{\text{NL}} = \hbar\omega_0^2 D_1 n_2 / (2\pi n_g A_{\text{eff}})$ is the nonlinear coefficient with A_{eff} being the effective mode area, and $F = \sqrt{\kappa_{\text{ex}} P_{\text{in}} / \hbar\omega_0}$ is the pump term where P_{in} is the on-chip pump power. For simplicity, the pump and loss terms are averaged over the entire resonator without considering the detailed coupling geometry between the rings and the bus waveguides, and the coupling is assumed to be wavelength independent ($g_{\text{co}} = g_{\text{co},0}$). A similar coupled equation set holds for the three-coupled-ring device.

Numerical simulations have been performed based on the above nonlinear wave equations. For the evolution of intracavity waveforms, we utilize the fourth-order Runge–Kutta method to update the fields in slow time t , in which discrete Fourier transformation is used to calculate the fast time derivative terms (with respect to the resonator coordinate z). The results are used to plot Fig. 4.5(b) and compare with the optical spectra in Fig. 4.1(b) and e (see Fig. 4.8). Parameters used for numerical simulations are: $\omega_0 = 2\pi \times 193.34$ THz, $Q_{\text{in}} = 75 \times 10^6$, $Q_{\text{ex}} = 45 \times 10^6$, $\delta\omega_A = \delta\omega_B = 10\kappa - G$ where G is the half gap created by the coupling (pump is red-detuned with respect to the upper branch resonance by 10κ), $D_1 = 2\pi \times 19.9766$ GHz, $D_2 = -2\pi \times 283.0$ kHz, $n_g = 1.575$, $P_{\text{in}} = 200$ mW, $g_{\text{NL}} = 0.0277$ s⁻¹, and $g_{\text{co},0} = 0.954$ mm⁻¹.

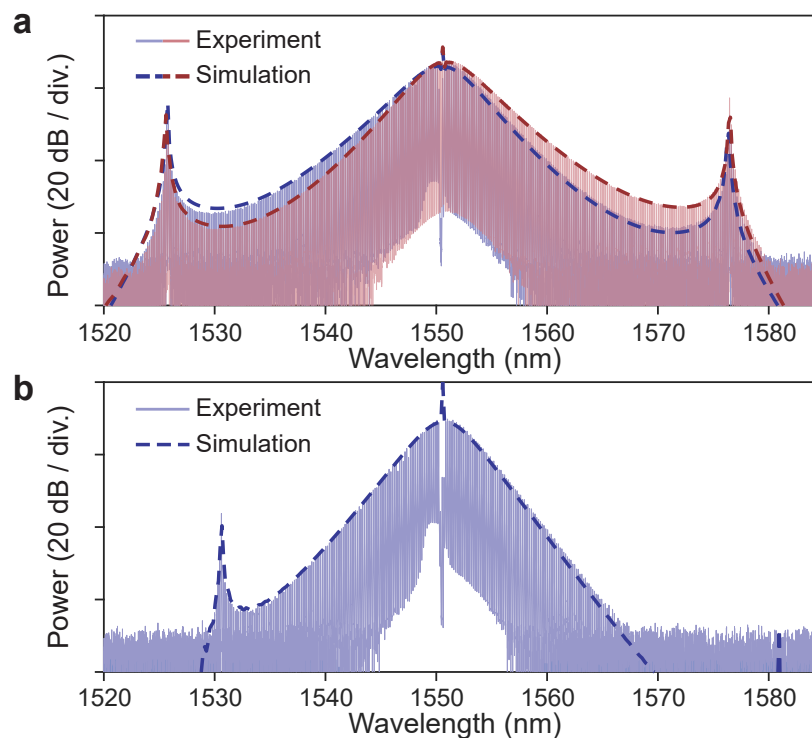


Figure 4.8: **Comparisons between simulated soliton spectra and experimental measurements.** (a) Simulated and measured optical spectra in a two-ring coupled resonator. The experimental results reproduce Fig. 4.1(b). The blue (red) traces represent the through (drop) port spectrum. (b) Simulated and measured optical spectrum in a three-ring coupled resonator. The experimental results reproduce Fig. 4.1(e).

4.7 Discussion

In summary, we have observed a new type of microcavity soliton that mode locks as pulse pairs distributed spatially over multiple ring resonators. The requirement to compensate overall normal dispersion of the rings requires that the pulses in each ring arrange themselves as a mirror image of the pulses in neighboring rings. Partial coupling of the resonators creates a situation in which ring resonator mode number is not conserved and this enables recurring spectral windows where the pairs can be formed. The presented bright soliton results use the CMOS-ready process that has previously been restricted to only dark pulse generation. This methodology can be generalized to other material platforms.

Critically, the combination of pulsed parametric oscillation, ultra-low optical loss and full CMOS compatibility brings a high level of integration complexity to many applications. More complex, optical-frequency-division systems and spectroscopy

systems are possible using the short pulse combs. Comb dividers could also use the strong dispersive waves in the soliton spectrum, when locked to a cavity reference, to produce low-noise radio frequency signals. Meanwhile, high- Q factor in this platform will benefit quantum comb applications [129, 130, 131] including squeezed quantum combs [132, 133]. Here, the full CMOS compatibility and ultra-low-loss waveguides can readily facilitate chip integration of delay line and beam splitter functions that have been applied recently to create large cluster states by time domain multiplexing and entanglement [134, 135]. It is also worth noting that the pulse pair systems demonstrated here exist across multiple coupled rings, suggesting connections to topological photonics [136, 137, 138]. Theoretical studies of topological phenomena in coupled-ring parametric oscillators showcase the range of intriguing phenomena that are possible [139]. Finally, the ability to distribute coherent pulses over multiple rings with individual taps and with simultaneous pulse formation at multiple wavelengths presents new opportunities for soliton science and microcomb applications, including new realizations optical buffers as originally proposed for coherently pumped solitons [140, 141].

BRILLOUIN BACKACTION THERMOMETRY FOR MODAL TEMPERATURE CONTROL

5.1 Introduction

¹ Stimulated Brillouin scattering provides optical gain for efficient and narrow-linewidth lasers in high-Q microresonator systems. The realization of microresonator-based Brillouin lasers [35, 34, 37, 143, 39, 46, 40, 41] has generated interest in their potential application to compact and potentially integrated Brillouin systems [33]. Moreover, high-coherence Brillouin lasers, featuring short-term linewidths below 1 Hz [37, 35, 143, 41], have been used for precision measurement and signal generation. This includes microwave synthesis [44, 45], interrogation of atomic clocks [48], and rotation measurement [46, 47, 41]. However, the thermal dependence of the Brillouin process, as well as the microresonator, impose strict temperature control requirements for long-term frequency-stable operation.

Here, we demonstrate a new method for temperature stabilization of Brillouin lasers based on backaction produced by the Brillouin anti-Stokes process. This process is shown to provide for phase sensitive locking to a temperature set point T_0 given by the following condition, which expresses the Brillouin phase matching condition (see Fig. 5.1) [37, 35]:

$$\Omega_B(T_0) = m \times \text{FSR}(T_0), \quad (5.1)$$

where $\Omega_B(T)$ is the Brillouin shift at temperature T (Eq. 1.5) and $m \times \text{FSR}(T)$ is an integer multiple (m) of the resonator free-spectral-range ($\text{FSR}(T)$) at temperature T . The actual temperature T_0 can be set by micro-fabrication control of FSR at a specified operating wavelength.

The short term frequency stability of a stimulated Brillouin laser (SBL) is set by fundamental noise associated with the thermal occupancy of photons involved in the Brillouin process [35]. In high-Q microresonators, this adds a white noise contribution to frequency noise with an equivalent short time linewidth less than 1 Hz [35, 46, 41]. However, on longer time scales the frequency stability is most often set by temperature variations. Here, thermo-optical and thermo-mechanical

¹Work presented in this chapter has been published in [142] “Brillouin backaction thermometry for modal temperature control.” *Optica* 9.7 (2022), pp. 701–705.

effects change the cavity resonant frequency [144, 145, 146], while the temperature dependence of the sound velocity causes drifts in the Brillouin frequency shift [147]. The latter couples temperature to the lasing frequency through mode pulling [35] and can also induce short term linewidth variation through the Brillouin α parameter [148] (Chapter 6). To compensate temperature drift, measurement of cavity temperature using modes belonging to different polarizations was demonstrated [149, 150] and has been recently employed in fiber optic Brillouin laser systems and silicon-nitride chip-resonator systems to stabilize frequency [151, 48, 152]. These dual-polarization modes feature different frequency tuning rates versus temperature, thereby providing a way to convert change in modal temperature to measurement of a frequency change. In contrast to this method which relies upon an external frequency reference to establish locking, the backaction method described here features an intrinsic reference temperature T_0 given by Eq. (5.1). Its sensitivity limit is also determined by the fundamental white frequency noise of the laser as opposed to the integrated laser linewidth.

Therefore, we study Brillouin back action and use it to both measure and phase-sensitively lock modal temperature to a reference temperature defined by the Brillouin phase-matching condition. At a specific lasing wavelength, the reference temperature can be precisely set by adjusting resonator free spectral range. This backaction control method is demonstrated in a chip-based Brillouin laser, but can be applied in all Brillouin laser platforms. It offers a new approach for frequency-stable operation of Brillouin lasers in atomic clock, frequency metrology, and gyroscope applications.

5.2 Illustration for the cascaded Brillouin laser induced backaction

We consider a Brillouin ring laser geometry shown in Fig. 5.1(a) wherein two pumping waves (dark and light grey arrows) are coupled from a waveguide into clockwise and counter-clockwise directions of the resonator. The frequencies of the pumping waves are close to a resonance, but are not necessarily on resonance. Exact details of this geometry and explanations of the Brillouin process are provided in reference [59]. Briefly, each pump wave provides power that is sufficient to excite corresponding Stokes laser waves (SBL1 and SBL2 shown as green and blue arrows in Fig. 5.1(a) that propagate opposite to their pumping wave and with a lower (Brillouin-shifted) frequency as a result of the phase matching condition. Power transfer from the pumping waves occurs by way of the Stokes scattering process. After laser action occurs, however, a strong anti-Stokes process occurs

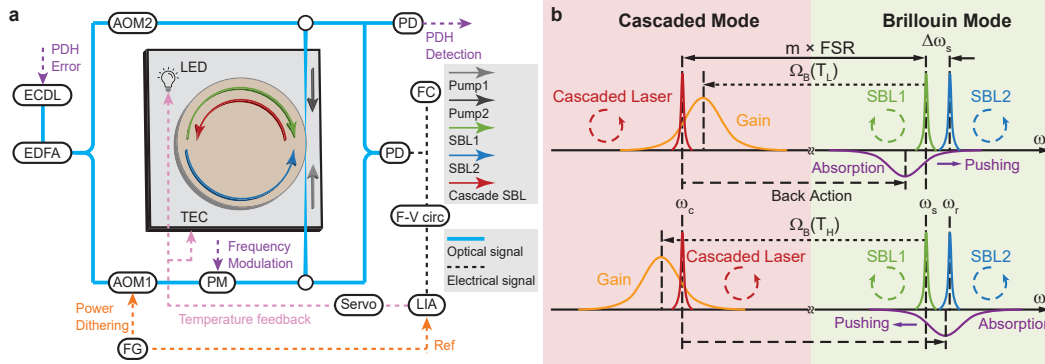


Figure 5.1: Experimental setup and illustrations of the cascaded Brillouin laser induced backaction. (a) Pump1 (counterclockwise, grey) and Pump2 (clockwise, black) waves are generated from an external cavity diode laser (ECDL) amplified by an Erbium doped fiber amplifier (EDFA). Both the pump1 and pump2 frequencies are shifted using acousto-optic modulators (AOM) to create a relative frequency offset. The frequency of Pump1 is further Pound-Drever-Hall (PDH) locked to the cavity resonance using a phase modulator (PM). Green (blue) arrow refers to Brillouin laser waves SBL1 (SBL2) discussed in panel (b). Pump1 has a slightly higher power so that the cascaded SBL is generated in the counter-clockwise direction (red). The beat signal of SBL1 and SBL2 is generated by a photodetector (PD) and its frequency is measured by a frequency counter (FC) and then frequency discriminated using a frequency tracking circuit (F-V circ) for subsequent phase sensitive detection by a lock-in amplifier (LIA), and temperature control using a light emitting diode (LED) and thermal electrical cooler (TEC). (b) Upper panel (low temperature case, T_L): the Brillouin shift $\Omega_B(T_L)$ is smaller than the mode frequency difference ($m \times \text{FSR}$, where m the mode number difference and FSR is the free spectral range in angular frequency). Backaction on SBL1 pushes its frequency away from the backaction absorption (purple) maximum, thereby increasing its frequency. This decreases the SBL1-SBL2 beating frequency ($\Delta\omega_s/2\pi$), when the cascaded laser power increases. Note: SBL2's frequency is not affected by the mode-pushing effect because the backaction absorption is directional according to the phase-matching condition. Lower panel (high temperature case, T_H): the Brillouin shift $\Omega_B(T_H)$ is larger than the mode frequency difference so that SBL1 has its frequency pushed lower. This increases the SBL1-SBL2 beating frequency ($\Delta\omega_s/2\pi$), when the cascaded laser power increases.

that is driven by the lasing fields. This anti-Stokes process creates absorption near the pumps, and the absorption strength is proportional to laser power, and this absorptive backaction clamps their circulating powers and hence the laser gain. The exact lasing frequencies can be controlled by tuning of the pumping frequencies, which causes frequency pulling of the laser frequencies such that about 1 MHz of pump frequency tuning induces 10s of kHz of Brillouin laser frequency pulling

$(\Delta\omega_s/2\pi)$. This configuration (non-degenerate, counter-propagating SBLs) is the starting point for implementation of the back-action temperature control method and a schematic of the key spectral features is provided in Fig. 5.1(b).

Now suppose that the power of SBL1 is increased so that it begins to function as a pumping wave for a new laser wave (the cascaded laser wave shown in red in Fig. 5.1(b)). The power of SBL2 is intentionally kept below threshold so that no cascading occurs. As noted above for the original pumping waves, the onset of laser action, now in the cascaded wave, induces absorptive backaction on its pump, SBL1, that is proportional to the cascaded laser power. It is important to note that on account of the phase matching condition, this absorption acts only on SBL1 (i.e., it is directional and does not affect SBL2). The spectrum of the absorption experienced by SBL1 is shown in purple in Fig. 5.1(b) and compensates SBL1 optical gain (not shown in the figure) provided by the original Pump1. As a result, SBL1 power is held constant, which is equivalent to the gain of the cascaded laser field (shown in orange in Fig. 5.1(b)) being clamped (even if Pump1 power is increased). The backaction absorption spectrum has a similar spectral profile to the Brillouin gain and the location of its maximum relative to the frequency of SBL 1 is determined by the phase matching condition for the backaction process. Specifically, maximum nonlinear absorption occurs for the condition of perfect phase matching given by Eq. (5.1).

Associated with the backaction absorption is a dispersion contribution that pushes the frequency of SBL1 away from the absorption center. At $T = T_0$ the pushing is zero since this temperature corresponds to perfect phase matching for which the SBL1 frequency is at the absorption maximum. However, cases where $T < T_0$ and $T > T_0$ (upper and lower panels in Fig. 5.1(b)) result in slight phase mismatch. Defining a phase mismatch parameter as $\Delta\omega \equiv m \times \text{FSR} - \Omega_B(T)$, for $\Delta\omega > 0$ (upper panel) and $\Delta\omega < 0$ (lower panel) the SBL 1 frequency is pushed higher and lower, respectively. Importantly, since the SBL1 and SBL2 are counter-propagating waves, the frequency of SBL2 is not affected by the cascade laser backaction due to the phase matching condition. Thus measurement of the frequency difference of SBL1 and SBL2 gives a direct way to measure $T - T_0$. As an aside, in reaching this conclusion, it is important to note that cavity resonant frequency tuning with respect to temperature is common mode for SBL1 and SBL2 as they share the same cavity longitudinal mode.

5.3 Measurement of Brillouin backaction and active locking

To implement this measurement it is convenient to use the power dependence of the frequency pushing. Specifically, a weak modulation of the pump 1 power (P) will induce a corresponding frequency modulation of SBL1 through modulation of the backaction dispersion. The resulting pump power (P) dependence of the SBL2-SBL1 beat frequency ($\Delta\omega_s$) is given by the following equation (section 5.4):

$$\frac{\partial\Delta\omega_s}{\partial P} \approx \frac{4g_0\gamma_{ex}}{\hbar\omega_p\gamma^2\Gamma} \frac{d\Omega_B}{dT} (T - T_0), \quad (5.2)$$

where $\Delta\omega_s \equiv \omega_r - \omega_s$, ω_s (ω_r) is the absolute angular frequency of SBL1 (SBL2), g_0 is the Brillouin gain, ω_p is the pump angular frequency, γ_{ex} is the external coupling rate, γ is the total cavity loss rate, and Γ is the Brillouin gain bandwidth. This result shows that frequency discrimination of $\Delta\omega_s$ combined with subsequent phase sensitive detection will provide an error signal whose magnitude and sign vary as $T - T_0$.

In the experiment, we used a 36 mm-diameter silica wedge resonator on silicon [37] with 8 μm thickness and wedge angle of 30 degrees. The resonator is packaged (similar to ref. [47]) with a thermal electrical cooler (TEC), a light emitting diode, and a thermistor. The TEC and thermistor are used for coarse temperature control and monitoring. The ultra-high-quality factor of the microcavity and the precisely controlled resonator size enable efficient generation of stimulated Brillouin laser action in the opposite propagation directions (operating wavelengths close to $\lambda \approx 1553.3$ nm). The intrinsic Q factor is 300 million and the SBL threshold is 0.9 mW. Details on the optical pumping as well as generation of SBL1, SBL2 and the cascaded laser wave are provided in the Figure 5.1(a) caption.

To setup the phase-sensitive servo temperature control, the beat frequency of SBL1 and SBL2 is dithered by modulating pump1 (and in turn the cascaded SBL power) using a power modulator (orange dashed line). The frequency of the beat signal is monitored using a frequency counter. A frequency tracking circuit demodulates the dithered signal and phase sensitive measurement is performed using a lock-in amplifier (Stanford Research SR830) to generate the error signal. Temperature control applies the feedback signal to a light emitting diode (fine control) and a thermal electrical cooler (coarse control).

Figure 5.2(a) shows the measured SBL1/SBL2 beating frequency ($\Delta\omega_s/2\pi$) when sweeping the pump power 1 from below to above cascaded laser operation. Sweeps are performed at a series of temperatures as indicated. As expected, when the pump

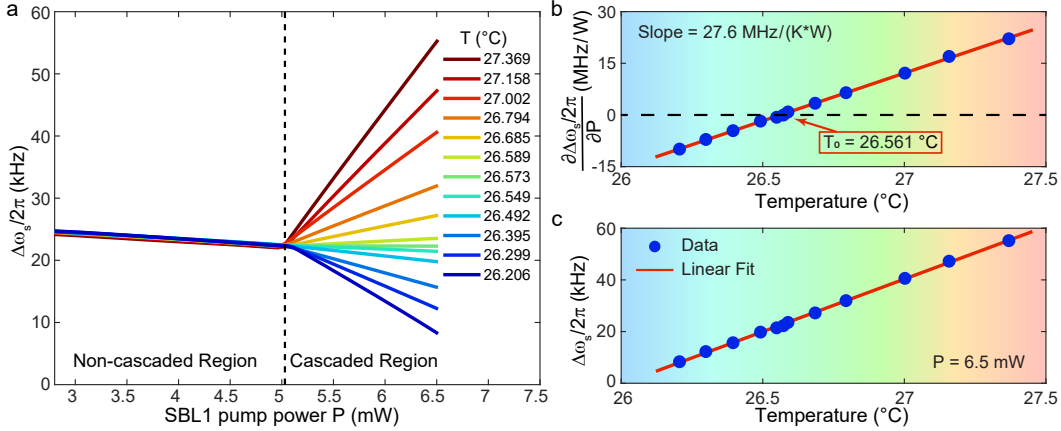


Figure 5.2: Measurement of Brillouin backaction. (a) The beating frequency of the counter-propagating SBLs is plotted versus pump1 power at a series of resonator temperatures as indicated. Frequencies at all temperatures closely track one another in the noncascaded regime with a slight power dependence is induced by the Kerr effect. In the cascaded regime, Brillouin backaction resolves the temperature differences with beating frequency showing a distinct dependence upon pump power. The slope of this dependence changes sign at T_0 (approximately 26.561 °C). (b) Measured SBL beating frequency change per unit pump power plotted versus temperature tuning. The temperature at perfect phase matching condition (T_0) is indicated. (c) Measured SBL beating frequency change plotted versus temperature. Slope is 41 kHz/K at 6.5 mW pump power.

power is low in the non-cascaded regime, all temperatures provide identical traces. The observed slope on all of these traces is the result of frequency shift provided by the Kerr effect [153]. On the other hand, for higher pump powers in the cascaded regime, the back-action effect is apparent with each temperature showing a distinctly different linear dependence on power. Significantly, the slope of this dependence is observed to change sign as discussed above, corresponding to temperatures above and below T_0 in Eq. (5.2). This sign change is essential for implementation of the phase sensitive detection servo control. An experimental plot showing the sign change in slope is provided in Fig. 5.2(b), where the absolute temperature reference $T_0=26.561$ °C is also measured. The beating frequency is observed to show a linear power dependence on temperature over the narrow range measured (see Fig. 5.2(c) measured at 6.5 mW pump power). The temperature tuning rate is smaller than the corresponding value provided by the dual-polarization approach [151]. Nonetheless, it should be possible to substantially increase this rate in resonators designed for forward-Brillouin scattering, wherein the reduced Brillouin-shift is accompanied by much narrower linewidths (see section 5.4). By fitting these

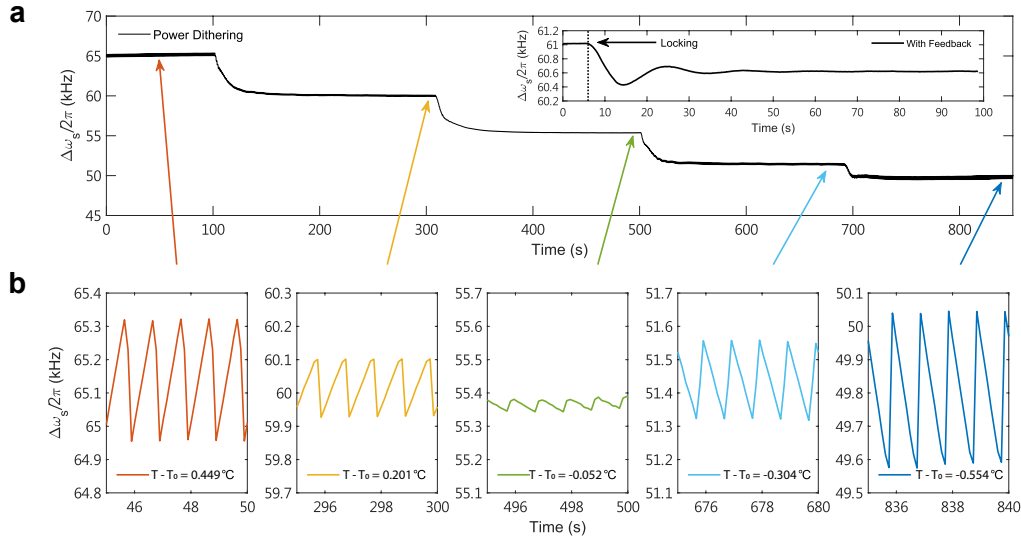


Figure 5.3: **Thermal tuning of the backaction with power dithering.** (a) The open-loop SBL beat frequency (backaction regime of Fig. 5.2) is measured versus time at a series of chip temperatures. A weak saw-tooth power modulation is applied to Pump 1. Inset: temperature stabilization of the resonator with servo control activated. (b) Zoom-ins of the plot in panel (a) showing how the polarity and amplitude of the sawtooth beat frequency modulation depends on temperature.

data sets, the experimental back-action strength $\partial^2\Delta\omega_s/(\partial P\partial T)$ is measured to be $2\pi \times 27.6 \text{ MHz}/(\text{W}\cdot\text{K})$, and is consistent with the theory from Eq. (5.2) ($2\pi \times 22.5 \text{ MHz}/(\text{W}\cdot\text{K})$, see section 5.4).

The linear power and temperature dependence of the backaction are further illustrated in Figure 5.3(a) where the beating frequency is measured versus time at a series of temperatures. To illustrate the change in slope with power at each temperature a weak and slowly-varying saw-tooth power modulation is applied. Zoom-in views of the corresponding saw-tooth modulation in the beat frequency are presented in Fig. 5.3(b). The change in polarity and amplitude of the backaction-induced modulation are apparent as the temperature is set to values above and below T_0 .

Finally, long term temperature stabilization of the system is demonstrated by closing the servo control loop. Here, a faster sinusoidal power modulation (200 to 500 Hz) is used to generate a small frequency dither on the SBL beating frequency. It is demodulated by a frequency to voltage conversion circuit and the error signal is generated by phase-sensitive detection with a lock-in amplifier as before. The output of a proportional-integral (PI) servo drives a 1 W white LED (see Figure 5.1(a)) for faster fine-control of temperature. The temperature is also controlled by a TEC that

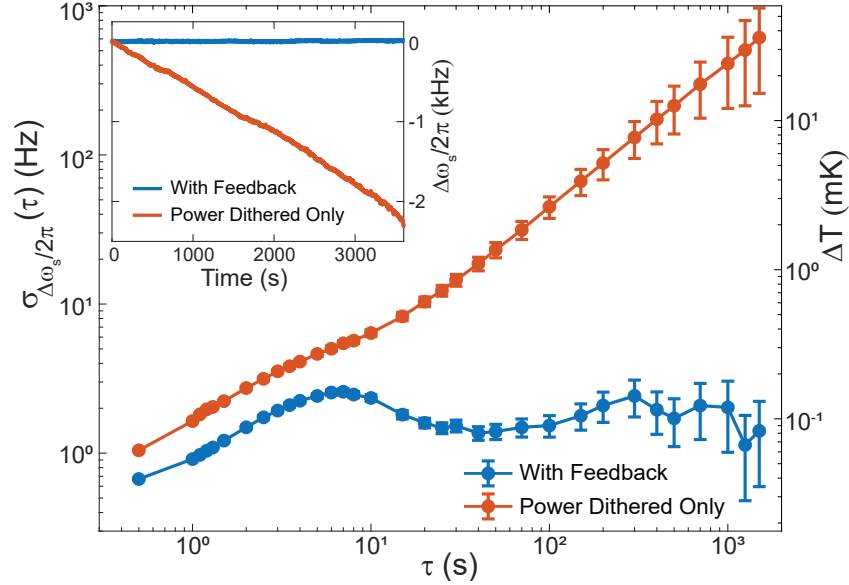


Figure 5.4: **Allan Deviation of SBL beating frequency $\Delta\omega_s$.** Allan Deviations of SBL beating frequency with (blue) and without (red) servo control. The error bar gives the standard deviation. Inset: SBL beating frequency versus time with (blue) and without (red) servo control.

provides slower feedback. The temperature feedback result is shown in the inset of Fig. 5.3(a). After an initial relaxation oscillation, the long term temperature drift (> 10 seconds) is stabilized.

With the servo-control loop disconnected, but with the power dither active, the beating frequency exhibits a continuous drift as large as 2.3 kHz in an hour, corresponding to around 0.13 °C temperature change per hour. This is apparent in both the measured SBL beat frequency (see Fig. 5.4 inset) and its Allan Deviation (ADEV) measurement presented in the main panel in Fig. 5.4). However, with the servo-control loop connected there is no observable drift in the beating frequency over an hour of measurement (see Fig. 5.4 inset). Also, over 1500 s averaging time (limited by data size of 1 hour) the Allan Deviation remains around 2 Hz, corresponding to about 0.1 mK temperature variation. In the short term, the drift suppression is believed to be limited by the thermal response of the cavity to the LED. In the future, a faster form of temperature feedback (e.g., an integrated resistive heater placed near the resonator) should further reduce this response time. Feed forward frequency correction could also be employed.

5.4 Theoretical analysis on cascade Brillouin laser backaction

Below we derive the temperature dependence of the frequency shift in SBL1 induced by power-dithering of the cascaded SBL. In the cavity-mode rotating frame, we write the pump, SBL, and cascaded SBL in the following form:

$$\dot{A} = \left[i(\omega_p - \omega_0) - \frac{\gamma}{2} \right] A - g_s^* |\alpha|^2 A + \sqrt{\frac{\gamma_{ex} P}{\hbar \omega_p}}, \quad (5.3)$$

$$\dot{\alpha} = \left[i(\omega_s - \omega_1) - \frac{\gamma}{2} \right] \alpha + g_s |A|^2 \alpha - g_c^* |\beta|^2 \alpha, \quad (5.4)$$

$$\dot{\beta} = \left[i(\omega_c - \omega_2) - \frac{\gamma}{2} \right] \beta + g_c |\alpha|^2 \beta, \quad (5.5)$$

where A , α , β are the normalized photon number amplitudes of the pump, SBL1, and cascaded SBL, respectively. Here we have adiabatically eliminated the phonon fields as described elsewhere [35]. We also note that the term involving g_c^* in Eq. 5.4 results from anti-Stokes scattering of the cascaded laser field β . The ω_p , ω_s , and ω_c are the lasing angular frequencies, and the ω_0 , ω_1 , ω_2 are the cavity angular frequencies. P is the input pump power (i.e., pump1 in Fig. 5.1). $g_{s,c}$ are defined by:

$$g_{s,c} = \frac{g_0}{1 + \frac{2i\Delta\Omega_{s,c}}{\Gamma}}, \quad (5.6)$$

$$\Delta\Omega_s = \omega_p - \omega_s - \Omega_s, \quad (5.7)$$

$$\Delta\Omega_c = \omega_s - \omega_c - \Omega_c, \quad (5.8)$$

$$\Omega_B \equiv \Omega_s \approx \Omega_c, \quad (5.9)$$

where Ω_s and Ω_c are the phonon angular frequencies associated with SBL1 and the cascaded SBL, respectively. Ω_B is the Brillouin shift, which is equal to $4\pi n c_s / \lambda_p$ (n is the refractive index, c_s is the speed of sound in silica, and λ_p is the pump wavelength). g_0 is the Brillouin nonlinear coefficient [35], γ_{ex} is the external coupling coefficient, Γ is the phonon damping rate.

In steady-state, if we assume good phase matching ($\Delta\Omega_{s,c} \ll \Gamma$), then the real parts and imaginary parts of Eq. (5.4) and Eq. (5.5) give:

$$\frac{\gamma}{2} = g_0 (|A|^2 - |\beta|^2) = g_0 |\alpha|^2, \quad (5.10)$$

$$\omega_s - \omega_1 = \frac{2g_0}{\Gamma} (|A|^2 \Delta\Omega_s + |\beta|^2 \Delta\Omega_c), \quad (5.11)$$

$$\omega_c - \omega_2 = \frac{2g_0}{\Gamma} |\alpha|^2 \Delta\Omega_c. \quad (5.12)$$

From Eq. (5.10) we get a photon number relation $|A|^2 = |\alpha|^2 + |\beta|^2$ as well as the clamping condition for the Stokes wave, $|\alpha|^2 = \gamma/2g_0$. These can be used to eliminate $|\alpha|^2$ and $|\beta|^2$ in Eq. (5.11) and Eq. (5.12), which yields,

$$\omega_s - \omega_1 = \frac{2g_0}{\Gamma} |A|^2 (\Delta\Omega_s + \Delta\Omega_c) - \frac{\gamma}{\Gamma} \Delta\Omega_c, \quad (5.13)$$

$$\omega_c - \omega_2 = \frac{\gamma}{\Gamma} \Delta\Omega_c. \quad (5.14)$$

To study the dependence of ω_s on the input power, we take the partial derivative with respect to $|A|^2$. Since $\omega_1, \omega_2, \omega_p, \Omega_B$ are independent of power the following hold,

$$\frac{\partial \omega_c}{\partial |A|^2} = \frac{\gamma}{\Gamma} \frac{\partial \Delta\Omega_c}{\partial |A|^2} = \frac{\gamma/\Gamma}{1 + \gamma/\Gamma} \frac{\partial \omega_s}{\partial |A|^2}, \quad (5.15)$$

$$\begin{aligned} \frac{\partial \omega_s}{\partial |A|^2} &= \frac{2g_0}{\Gamma} (\omega_p - \omega_c - 2\Omega_B) \\ &+ \frac{2g_0}{\Gamma} |A|^2 \frac{\partial (\Delta\Omega_s + \Delta\Omega_c)}{\partial |A|^2} - \frac{\gamma}{\Gamma} \frac{\partial \Delta\Omega_c}{\partial |A|^2} \\ &= \frac{2g_0}{\Gamma} \frac{\omega_p - \omega_c - 2\Omega_B}{1 + \frac{\gamma/\Gamma}{1 + \gamma/\Gamma} \left(1 + \frac{2g_0|A|^2}{\Gamma}\right)}. \end{aligned} \quad (5.16)$$

Eq. (5.15) gives the mode pulling induced in the cascaded Brillouin laser frequency [59] caused by changes in the SBL1 frequency. This effect moves the cascaded wave's frequency towards its cavity mode frequency. Next, we assume for simplicity that operation is only slightly above the cascaded threshold, such that Eq. (5.10) gives $2g_0 |A|^2 \approx \gamma$. In this case Eq. (5.16) simplifies into,

$$\frac{\partial \omega_s}{\partial |A|^2} = \frac{1}{1 + \gamma/\Gamma} \frac{2g_0}{\Gamma} (\omega_p - \omega_c - 2\Omega_B). \quad (5.17)$$

The correction factor γ/Γ is small ($\gamma/\Gamma \ll 1$) in this system since the cavity linewidth is typically much smaller than the phonon damping rate (i.e., justification for adiabatic approximation above). Therefore, we drop the correction factor in Eq. (5.17). Next, the $|A|^2$ can be further replaced by $P = \hbar\omega_p\gamma^2 |A|^2 / \gamma_{ex}$, which is the input pump power above cascade threshold (obtained by solving the steady state of Eq. (5.3) with clamping conditions for $|\alpha|^2$). Then, Eq. (5.17) simplifies to the following:

$$\frac{\partial \omega_s}{\partial P} = \frac{2g_0\gamma_{ex}}{\hbar\omega_p\gamma^2\Gamma} (\omega_p - \omega_c - 2\Omega_B). \quad (5.18)$$

The derivative with respect to temperature is now taken in this expression to arrive at the following,

$$\frac{\partial^2 \omega_s}{\partial P \partial T} \approx -\frac{4g_0 \gamma_{ex}}{\hbar \omega_p \gamma^2 \Gamma} \frac{d\Omega_B}{dT}. \quad (5.19)$$

In writing this expression the temperature dependence of $\omega_p - \omega_c \approx \omega_0 - \omega_2 \approx 2m \times \text{FSR}$ is neglected. This term's temperature dependence is dominated by the thermorefractive and thermoexpansion effects, which are much weaker than the temperature dependence of the Brillouin frequency. For example, in silica glass the thermoexpansion coefficient is $\alpha_L = 0.51 \times 10^{-6}/\text{K}$ and the thermorefractive coefficient is $dn/dT = 11.6 \times 10^{-6}/\text{K}$, so that $d(\omega_p - \omega_c)/dT \approx 2\pi \times 180 \text{ kHz/K}$. This compares to $d\Omega_B/dT \approx 2\pi \times 1.16 \text{ MHz/K}$ at 1550 nm (estimated from 1.36 MHz/K at 1320 nm [146]), and justifies the simplification involved in Eq. (5.19).

Now, if we introduce an independent backward propagating SBL as a reference with higher angular frequency ω_r , the result is,

$$\frac{\partial^2 \Delta\omega_s}{\partial P \partial T} = \frac{\partial^2 (\omega_r - \omega_s)}{\partial P \partial T} = \frac{4g_0 \gamma_{ex}}{\hbar \omega_p \gamma^2 \Gamma} \frac{d\Omega_B}{dT}, \quad (5.20)$$

which is the temperature derivative of Eq. 5.2. The silica resonator has $g_0/2\pi = 0.61 \text{ mHz}$, $\Gamma/2\pi = 30 \text{ MHz}$, $\gamma_{ex}/2\pi = 110 \text{ kHz}$, $\gamma/2\pi = 860 \text{ kHz}$, $\omega_p/2\pi = 193 \text{ THz}$, giving a theoretical estimation of $\partial^2 \Delta\omega_s/\partial P \partial T = 2\pi \times 22.5 \text{ MHz/(W.K)}$, which compares favorably with the experimental value in Fig. 5.2 of $2\pi \times 27.6 \text{ MHz/(W.K)}$. The difference here mainly originates from the uncertainty of certain parameters.

As an aside, Eqs. (5.19) and (5.20) show that frequency tuning response with respect to temperature depends inversely upon the Brillouin damping rate Γ . Along these lines, forward Brillouin scattering in high-Q silica microresonators has produced damping rates much smaller than for back scattering on account of the smaller required Brillouin shift for backscattering [34, 154]. We intend to investigate this approach as a means to increase the backaction response.

To estimate g_0 above (in the unit of rad/s), we use the following equations [155]:

$$g_0 \approx \frac{\hbar \omega^3}{2P_{\text{clamp}} Q_T Q_E} \quad (5.21)$$

$$\approx \frac{2\pi \Delta\nu_{\text{clamp}}}{n_{th}}, \quad (5.22)$$

where P_{clamp} is the clamped power of SBL1 at the cascading threshold, Q_T (Q_E) is the total (external) quality factor, $\Delta\nu_{\text{clamp}}$ is the full-width-half-maximum of

the fundamental SBL1 linewidth under cascaded clamping conditions, n_{th} is the number of thermal phonon quanta at the operating temperature. For the 36 mm silica resonator at room temperature, we measured $\Delta\nu_{\text{clamp}} = 0.35$ Hz and used the theoretical $n_T \approx 577$.

5.5 Discussion

In summary, we have investigated Brillouin backaction and shown that it provides a way to phase sensitively lock an optical resonator to an absolute temperature defined by the phase matching condition. The back-action has been shown to induce both linear power and temperature dependences in a readily measured optical beat frequency. The polarity of the power dependence depends upon operation above or below the phase matching temperature. This feature and the high stability of the beat frequency were used to servo control the optical mode temperature to 0.1 mK stability levels. While not yet at the temperature stability level of the cross polarization method when applied to microcavities (0.008 mK) [156], cross-polarization stabilization has existed for a decade. And we believe the initial results presented here can be substantially improved. An important aspect of the phase sensitive control is that the noise limit is determined by SBL frequency noise at large offset frequencies set by backaction modulation. Here, the rate is 500 Hz, but could be set even higher if necessary to avoid laser frequency noise. Moreover, characterization of the absolute optical frequency stability that is achievable by this method is a possible area of investigation. The range of material systems on which Brillouin laser action has been demonstrated (including integrable platforms) suggests that this method can find wide use.

THE LINEWIDTH ENHANCEMENT FACTOR IN A MICROCAVITY BRILLOUIN LASER

6.1 Introduction

¹ The linewidth of stimulated Brillouin lasers (SBLs) has received considerable attention for some time. SBLs based on optical fiber [157], for example, feature narrow linewidths that are useful for generation of highly stable microwave sources [158, 159]. More recently, broad interest in micro and nanoscale Brillouin devices [33] has focused attention on tiny, often chip-scale, SBLs in several systems [34, 35, 36, 37, 38, 39, 40, 41]. These devices have high power efficiency [42], provide flexible operating wavelengths [43], and their fundamental linewidth can be reduced to less than 1 Hz [42, 41]. For these reasons they are being applied in a range of applications including radio-frequency synthesizers [44, 45], ring-laser gyroscopes [46, 41, 47] and high-coherence reference sources [38].

SBLs derive gain through a process that is parametric in nature and for which scattering of an optical pump into a Stokes wave from an acoustic phonon must be phase-matched [160, 8]. When the phonon field is strongly damped, the process mimics stimulated emission. Nonetheless, phonon participation introduces dramatic differences into SBL linewidth behavior compared with conventional lasers. For example, while the conventional Schawlow-Townes laser linewidth [161] is insensitive to temperature, the fundamental SBL linewidth is proportional to the number of thermo-mechanical quanta in the phonon mode and therefore to the Boltzmann energy $k_B T$ [42]. This dependence has been verified from cryogenic to room temperature [155]. Brillouin lasers can also oscillate on multiple lines through the process of cascade [42], in which an initial Stokes wave can serve to pump a second Stokes wave and so forth. Cascading introduces additional contributions to the SBL linewidth [162]. Finally, the parametric nature of the process means that pump phase noise couples through to the laser linewidth, although it is strongly suppressed by the phonon damping [163].

The fundamental linewidth of lasers is increased by the well-known linewidth en-

¹Work presented in this chapter has been published in [148] “The linewidth enhancement factor in a microcavity Brillouin laser.” *Optica* 7.9 (2020), pp. 1150–1153.

hancement factor α that characterizes amplitude-phase coupling of the field [164]. This quantity is best known for its impact on the linewidth of semiconductor lasers [165], and its understanding, control and measurement have long been subjects of interest [166, 167, 168]. Here, the linewidth enhancement factor is studied in SBLs. The parametric nature of Brillouin gain is shown to strongly influence this parameter. Phase mismatch causes a non-zero α factor. Measurements of SBL frequency noise are used to determine α versus controlled amounts of phase mismatch, and the results are in good agreement with theory. Significant enhancements to the linewidth are predicted and measured even when the SBL is operated only modestly away from perfect phase matching.

6.2 Experiment setup and illustration for α factor

Amplitude-phase coupling occurs at a specified optical frequency when the real and imaginary parts of the optical susceptibility (equivalently refractive index and gain) experience correlated variations subject to a third parameter. The ratio of the real to imaginary variation is the α parameter [165]. With a non-zero α -parameter, noise that normally couples only into the laser field amplitude can also couple into the phase. And because phase fluctuations are responsible for the finite laser linewidth [164], the non-zero α -factor thereby causes linewidth enhancement. For a physical understanding of how a non zero α parameter arises within the SBL system consider Fig. 6.1(a).

Optical pumping at frequency ω_P on a cavity mode causes a Lorentzian-shaped gain spectrum through the Brillouin process. The Brillouin gain spectrum is frequency down-shifted by the phonon frequency Ω (Brillouin shift frequency) relative to the pumping frequency. Laser action at frequency ω_L is possible when a second cavity mode lies within the gain spectrum, which requires that $\Delta\omega \equiv \omega_P - \omega_L$ is close in value to Ω . Perfect phase matching corresponds to laser oscillation at the peak of the gain (i.e., $\Delta\omega = \Omega$). Also shown in Fig. 6.1(a) is the refractive index spectrum associated with the gain spectrum according to the Kramers-Kronig relations. It is apparent that α (the ratio of variation of real to imaginary susceptibility) will be zero for phase-matched operation, while it increases with increased frequency detuning relative to perfect phase matching.

Analysis (section 6.5) shows that the α -factor enhancement of the fundamental SBL linewidth $\Delta\nu_{\text{SBL}}$ is,

$$\Delta\nu_{\text{SBL}} = \Delta\nu_0(1 + \alpha^2), \quad (6.1)$$

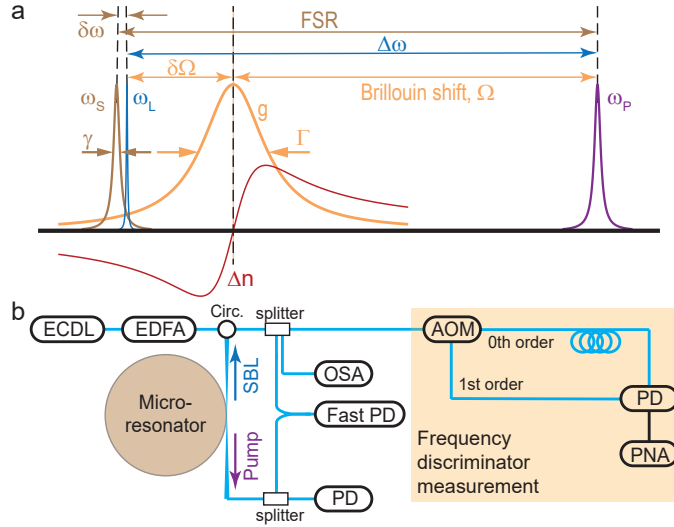


Figure 6.1: SBL phase mismatch illustration and experimental setup. (a) Brillouin gain process in the frequency domain. Purple (brown) curve refers to pump (Stokes) cavity mode at frequency ω_P (ω_S). Blue curve refers to the SBL laser signal at frequency ω_L . Orange and red curves correspond to gain (g) spectrum and refractive index (Δn), respectively. Brillouin shift frequency (Ω), gain spectrum linewidth (Γ), and cavity linewidth (γ) are also indicated. Frequency detunings $\delta\omega$ and $\delta\Omega$ are defined in the text. (b) Experimental setup for α and linewidth measurement.

where $\Delta\nu_0$ is the non-enhanced ($\alpha = 0$) SBL linewidth given below as Eq. 6.3, and where the linewidth enhancement factor can be expressed using two equivalent frequency-detuning quantities relative to perfect phase matching:

$$\alpha = \frac{2\delta\Omega}{\Gamma} = \frac{2\delta\omega}{\gamma}. \quad (6.2)$$

In the first equality, phonon mode detuning $\delta\Omega \equiv \Omega - \Delta\omega$ is normalized by Γ , the Brillouin gain bandwidth (i.e., phonon decay rate constant). In the second equality, optical mode detuning $\delta\omega \equiv \Delta\omega - \text{FSR}$ (FSR is the unpumped cavity free-spectral-range) is normalized by γ , the photon decay rate constant. Note that the sign of α changes to either side of perfect phase matching. Also, as an aside, $\delta\omega$ is the mode pulling induced by the Brillouin gain spectrum [42]. $\Delta\nu_0$ is given by:

$$\Delta\nu_0 = \left(\frac{\Gamma}{\gamma + \Gamma} \right)^2 \frac{\hbar\omega_L^3 n_{\text{th}}}{4\pi Q_{\text{T}} Q_{\text{ex}} P_{\text{SBL}}}. \quad (6.3)$$

where \hbar is the reduced Planck's constant, P_{SBL} is the SBL output power, and n_{th} is the number of thermal quanta in the phonon mode. This expression is the same as that derived in ref. [42], except for omission of the zero-point energy terms and

also inclusion of the near-unity correction factor $[\Gamma/(\gamma + \Gamma)]^2$ relating to the finite damping rate of the phonons (derivation in section 6.5).

As a first step towards verification of Eqs. (6.1) and (6.2), it is necessary to measure the phase mismatch detuning at each point where linewidth will be measured. As shown in Fig. 6.1(b), an external cavity diode laser (ECDL) (Newport, TLB-6728) near 1550 nm passes through an erbium-doped fiber amplifier (EDFA) and is coupled to the microcavity using a tapered fiber. Its frequency is Pound-Drever-Hall locked (not shown) to the center of cavity resonance. Pump power is controlled using an acousto-optic modulator (AOM) as an attenuator in combination with a feedback loop (not shown). The resonator diameter is around 7.1 mm, corresponding to an FSR of 10.8 GHz, which is selected to closely match the Brillouin shift frequency in silica at 1550 nm. The resonator chip temperature is actively stabilized to $26.5000 \pm 0.0005^\circ\text{C}$ using a temperature controller. The SBL emission propagates opposite to the direction of pumping on account of the phase-matching condition. The emission is coupled to a series of measurement instruments through a circulator. An optical spectrum analyzer (OSA) is used to record the laser and pump spectra as well as to measure SBL power. Pump and SBL signals are mixed on a fast photodetector (PD) (Thorlabs, DXM30AF) to measure their frequency difference. Another PD monitors the pumping power.

6.3 Measurement on α factor and Brillouin phase mismatch

To vary the phase mismatch detuning, the pump laser wavelength λ_P is tuned, which is achieved by selecting different longitudinal modes within the same transverse mode family as pump and Stokes modes. This has the effect of varying Ω through the relationship $\Omega = 4\pi n c_s / \lambda_P$ (n : refractive index, c_s : speed of sound in the microcavity). Since Ω is not directly measurable in the experiment, we instead obtained information on the phase mismatch using $\delta\omega$, which requires measurement of $\Delta\omega$ and FSR.

The frequency $\Delta\omega$ is determined by first measuring the beating frequency of the pump and the SBL using a fast photodetector, followed by measurement of the detected current on an electrical spectrum analyzer. Beyond being influenced by mode pulling as noted above, this beating frequency is also slightly shifted via backaction of the amplitude-phase coupling (section 6.5) and the optical Kerr effect [153], both of which are proportional to the SBL powers. Therefore, to account for these effects, the beatnote frequencies were measured at 5 different SBL power

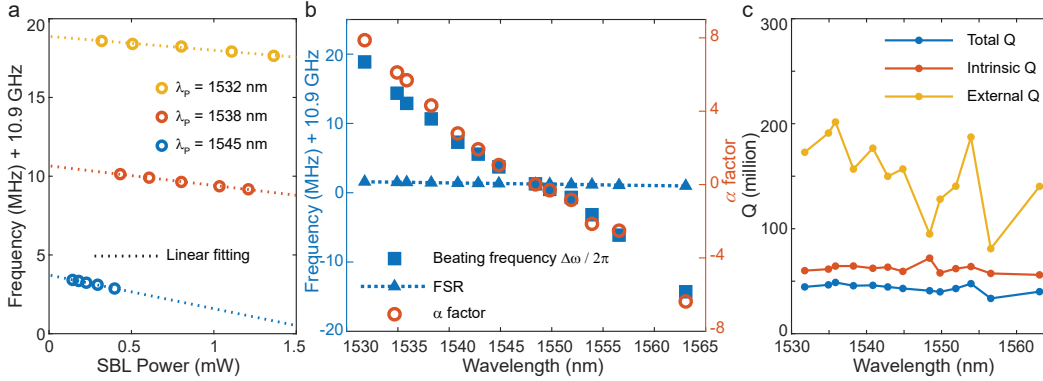


Figure 6.2: Measured Brillouin gain phase mismatch and α factor. (a) Beating frequency between the pump laser and the SBL is plotted as a function of SBL power. Linear fitting is applied to eliminate the influence of the Kerr effect and α factor backaction, and the y-axis intercept is plotted as $\Delta\omega$ in panel (b). Blue, red and yellow traces correspond to measurements at 1545 nm, 1538 nm and 1532 nm, respectively. (b) The extrapolated beating frequency (squares) and FSR (triangles) are plotted versus wavelength. The calculated α factor (red circles) is plotted versus wavelength using Eq. (6.2). The Brillouin gain center occurs at around 1548 nm where $\text{FSR} = \Delta\omega$. (c) Total (Q_T), intrinsic (Q_0) and external (Q_{ex}) quality factors are plotted versus wavelength. The values are measured in the same transverse mode family.

levels. Representative measurements performed at three pump wavelengths are shown in Fig. 6.2(a). The y-intercept of these plots provides the required beating frequency in the absence of the above effects and a summary plot of a series of such measurements is provided as the blue-square data points in Fig. 6.2(b). As an aside, the data point near 1559 nm is missing because of strong mode crossings at this wavelength in the SBL microcavity (i.e., higher-order mode families become degenerate with the SBL mode family).

To determine the FSR at each pumping wavelength, the mode spectrum of the resonator is measured by scanning a tunable laser whose frequency is measured using a radio-frequency calibrated interferometer [26]. The measured FSR is plotted versus wavelength as the dotted line in Fig. 6.2(b). Measurement of the FSR this way also ensured that pumping was performed on the same transverse mode family as the pumping wavelength was tuned. This is important since mode volume would change strongly were mode family to change. In Fig. 6.2(b), the phase-matching condition (gain center) occurs when $\text{FSR} = \Delta\omega$ ($\delta\omega = 0$) at around 1548 nm pump wavelength. We can also use the Brillouin shift at gain center to infer that $c_s = 5845$ m/s, which is consistent with the material properties of silica [169].

Finally, γ is determined by measurement of the cavity linewidth at each wavelength (equivalently, the total Q-factor Q_T of the resonator). By measurement of both linewidth and transmission on cavity resonance it is possible to extract both the intrinsic Q-factor Q_0 and external coupling Q-factor Q_{ex} at each wavelength ($1/Q_T = 1/Q_0 + 1/Q_{ex}$). A plot of the results is provided in Fig. 6.2(c). The Q_0 values inferred this way are relatively constant across the measured modes, while the Q_{ex} exhibits variation that reflects wavelength dependency of the coupling condition. The Q factors are significantly lower than state-of-the-art resonators of the same kind [37], which is intentional and increases the sensitivity of noise measurement that follows. Using Eq. 6.2, the theoretical α factor as a function of wavelength from 1532 nm to 1563 nm is plotted in Fig. 6.2(b) (red circles). Deviations of beating frequency and the α factor from a linear trend are a result of variations of total Q factor across the measured wavelengths. The largest α factor is greater than 7 so that a fundamental linewidth enhancement of more than $1 + 7^2 = 50$ is expected at the largest detuning values.

6.4 Measurement on the α factor enhanced fundamental linewidth

A frequency discriminator method [170, 171] (for an updated noise measurement method, see Chapter 8) is used to measure the noise spectrum of the two-sided white frequency noise spectral density S_w of the SBL as shown in the Fig. 6.1(b). An interferometer is used to measure the laser frequency noise. Therein, the laser signal is sent into an AOM which is split into frequency-shifted (1st order) and unshifted (0th order) signals. The latter is delayed in a 1-km long fiber and then the two signals are mixed on a PD (Newport, 1811-FC). The delay sets up a frequency to amplitude discriminator with discrimination gain proportional to the amount of the interferometer delay. To measure the frequency noise spectral density, the detected current is measured using an electrical phase noise analyzer (PNA) and the spectrum is fit to obtain the two-sided spectral density of the SBL laser (section 6.6).

The fundamental noise component in S_w , defined as S_F , is related to the fundamental SBL linewidth through $2\pi S_F = \Delta\nu_{SBL}$ [153] where $\Delta\nu_{SBL}$ is given in Eq. 6.3. And the inverse power dependence contained in $\Delta\nu_{SBL}$ is used to extract S_F from the measurement of S_w . Data plots of S_w versus inverse power at three pumping wavelengths are shown in the inset of Fig. 6.3 and reveal this power dependence. Of importance to this measurement is that optical pumping power was controlled by attenuation of the pump so that its phase noise was constant throughout the measurement. Therefore, only the intrinsic contribution to linewidth could cause the

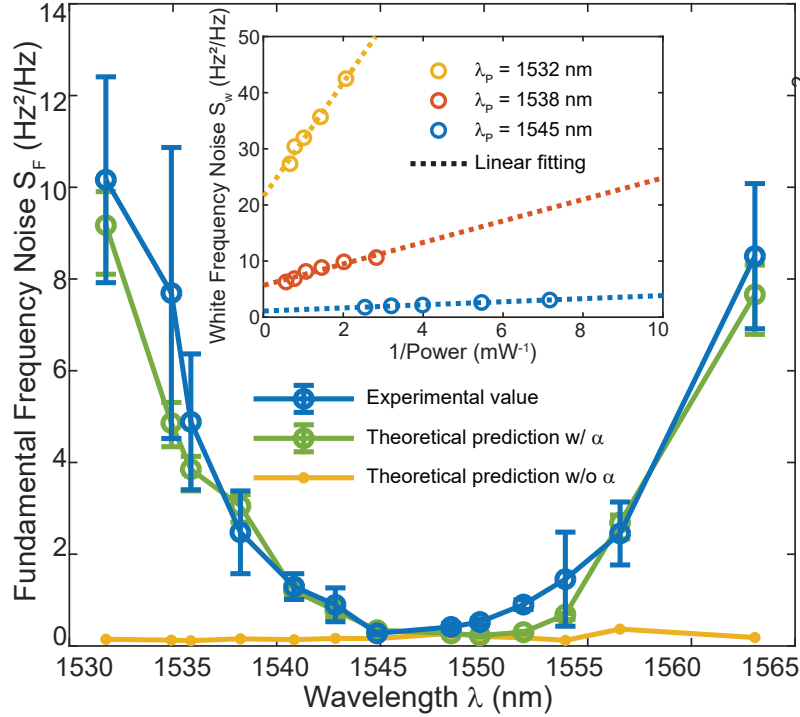


Figure 6.3: **Measured SBL frequency noise enhancement from the α factor.** Measured SBL frequency noise S_F (blue); theoretical S_F (Eqn. 6.3) prediction (green) with α obtained from Fig. 6.2(b); and non-enhanced S_0 formula ($\alpha=0$) [42] prediction (yellow); all plotted versus pump wavelength normalized to 1 mW output power. Error bars on the S_F noise correspond to the error in determining slope (see inset). Error bars on the Eqn. 6.3 prediction mainly arise from errors in $\Delta\omega$ and Q measurement errors. Variations of the $\alpha=0$ prediction mainly arise from Q_{ex} differences. Inset: SBL frequency noise S_w is plotted versus the reciprocal of SBL output power. A linear fitting is applied to determine S_F from the slope, and then plotted in the main panel. Blue, red and yellow data correspond to measurements at 1545 nm, 1538 nm and 1532 nm, respectively.

observed power dependence. The slope is equal to S_F normalized to an output power of 1 mW. Linear fitting provides the slopes which are plotted versus wavelength in the main panel of Fig. 6.3. The corresponding minimum measured fundamental noise is about $S_F = 0.2 \text{ Hz}^2/\text{Hz}$ ($\Delta\nu_{SBL} = 1.25 \text{ Hz}$) near the phase matching condition (gain center), and the maximum fundamental noise is more than $S_F = 10 \text{ Hz}^2/\text{Hz}$ ($\Delta\nu_{SBL} = 63 \text{ Hz}$), corresponding to $50\times$ noise enhancement, at the largest mismatch detunings. Comparison to Eq. (6.3) is provided as the green plot in Fig. 6.3. In this plot Q_T , Q_{ex} and α (Fig. 6.2(b, c)) measurements at each wavelength are used with no free parameters. γ can be obtained from Q_T , and we can infer $\Gamma/2\pi$ to be 34.7 MHz, assuming it is constant over wavelength. Also, $n_{th} = 572$ is used

(corresponding to the operating temperature of 26.5 °C). There is overall good agreement with the measured linewidth values. The conventional $S_0 = \Delta\nu_0/(2\pi)$ (with $\alpha=0$) is also plotted for comparison.

The nonzero intercept on the y axis of the inset to Fig. 6.3 is believed to be associated with transferred pump phase noise associated with imperfect PDH locking. This contribution will increase with increasing α . Both it and the linewidth contribution of the pump phase noise are analyzed in section 6.5.

6.5 Theoretical analysis

Derivation of the α factor in Brillouin lasers

We derive the α factor in stimulated Brillouin laser (SBL) systems by starting from the Hamiltonian of the system:

$$H = \hbar(\omega_P \tilde{A}^\dagger \tilde{A} + \omega_s \tilde{a}^\dagger \tilde{a} + \Omega \tilde{b}^\dagger \tilde{b}) + \hbar g_B (\tilde{A}^\dagger \tilde{a} \tilde{b} + \tilde{A} \tilde{a}^\dagger \tilde{b}^\dagger), \quad (6.4)$$

where \tilde{A} , \tilde{a} and \tilde{b} are the lowering operators of the pump, Stokes and phonon modes, respectively; ω_P , ω_s and Ω are the resonance frequencies of the pump, Stokes and phonon modes, respectively; and g_B is the single-particle Brillouin coupling [42]. We have ignored terms that are strongly out of phase match (i.e., energy non-conserving) in the Hamiltonian to simplify the discussion. The fast time dependencies are removed from the operators as follows:

$$A \equiv \tilde{A} \exp(i\omega_{P,\text{in}}t), \quad (6.5)$$

$$a \equiv \tilde{a} \exp(i\omega_L t), \quad (6.6)$$

$$b \equiv \tilde{b} \exp(i\Omega_L t), \quad (6.7)$$

where A , a and b are the slow-varying lowering operators; $\omega_{P,\text{in}}$ is the pumping frequency; ω_L is the SBL frequency and Ω_L is the mechanical vibration frequency. Replacing the operators with the slow-varying ones results in an effective Hamiltonian:

$$H = \hbar(\delta\omega_P A^\dagger A + \delta\omega a^\dagger a + \delta\Omega b^\dagger b) + \hbar g_B (A^\dagger a b + A a^\dagger b^\dagger), \quad (6.8)$$

where $\delta\omega_P \equiv \omega_P - \omega_{P,\text{in}}$ is the pump mode frequency detuning compared to the external pump, and $\delta\omega \equiv \omega_s - \omega_L$ ($\delta\Omega \equiv \Omega - \Omega_L$) is the detuning of Stokes (phonon) cavity mode compared to the laser (mechanical vibration) frequency. We note that the slow-varying amplitudes are directly referenced to the true oscillating frequencies of each mode instead of the resonance frequencies, which removes the fast time dependence in the interaction terms.

The Heisenberg equations of motion for the Stokes mode and the phonon mode are derived. Then, the quantum operators are replaced with classical fields as the dominant source of noise in this system is phonon thermal noise [42]. Finally, phenomenological damping terms are inserted as follows:

$$\frac{da}{dt} = -\left(\frac{\gamma}{2} + i\delta\omega\right)a - ig_{\text{B}}Ab^*, \quad (6.9)$$

$$\frac{db}{dt} = -\left(\frac{\Gamma}{2} + i\delta\Omega\right)b - ig_{\text{B}}Aa^*, \quad (6.10)$$

where γ (Γ) is the energy decay rates for the Stokes (phonon) mode.

We first seek nonzero steady-state solutions to the above equations that represent SBLs. By writing the equation for b^* using Eq. (6.10),

$$\frac{db^*}{dt} = -\left(\frac{\Gamma}{2} - i\delta\Omega\right)b^* + ig_{\text{B}}A^*a, \quad (6.11)$$

the equations (6.9) and (6.11) form a linear system in a and b^* . The requirement for nonzero solutions (i.e., zero determinant of the coefficient matrix) gives the equation:

$$\left(\frac{\gamma}{2} + i\delta\omega\right)\left(\frac{\Gamma}{2} - i\delta\Omega\right) - g_{\text{B}}^2|A|_0^2 = 0, \quad (6.12)$$

where the subscript 0 indicates steady state. This complex equation can be solved as:

$$\frac{2\delta\omega}{\gamma} = \frac{2\delta\Omega}{\Gamma}, \quad (6.13)$$

$$g_{\text{B}}^2|A|_0^2 = \frac{\gamma\Gamma}{4}\left(1 + \frac{4\delta\Omega^2}{\Gamma^2}\right). \quad (6.14)$$

For convenience, we define $\alpha \equiv 2\delta\omega/\gamma = 2\delta\Omega/\Gamma$ and later demonstrate that α is indeed the linewidth enhancement factor. With α defined, the steady-state pump photon number is,

$$|A|_0^2 = \frac{\gamma\Gamma}{4} \frac{1 + \alpha^2}{g_{\text{B}}^2} = \frac{\gamma}{2g}(1 + \alpha^2), \quad (6.15)$$

where the Brillouin gain coefficient $g = 2g_{\text{B}}^2/\Gamma$ has been defined. Since $\Gamma \gg \gamma$ in our microcavity system, we can adiabatically eliminate b^* from Eq. (6.9) by setting $db^*/dt = 0$ in Eq. (6.11):

$$\frac{da}{dt} = \left(-\frac{\gamma}{2} + \frac{g|A|_0^2}{1 + \alpha^2}\right)(1 + i\alpha)a, \quad (6.16)$$

where the definition of α has been used. Here, $|A|^2$ implicitly depends on a through the pump mode dynamics and controls the gain saturation. Alternatively, Eqn. 6.16 can be represented using the amplitude $|a|$ and phase $\phi_a = \ln(a/a^*)/(2i)$ variables,

$$\frac{d|a|}{dt} = \left(-\frac{\gamma}{2} + \frac{g|A|^2}{1+\alpha^2} \right) |a|, \quad (6.17)$$

$$\frac{d\phi_a}{dt} = \left(-\frac{\gamma}{2} + \frac{g|A|^2}{1+\alpha^2} \right) \alpha, \quad (6.18)$$

which illustrates that $\alpha = |a|\dot{\phi}_a/\dot{|a}|$ represents amplitude-phase coupling.

Henry [165] defined the α factor as the ratio of the change in real part of the refractive index and the change in the imaginary part. Below we show that this interpretation is consistent with that derived from the coupled-mode equations. For a system with Lorentzian gain, the imaginary part of the gain-induced susceptibility can be written as

$$\chi_I(\omega_B) = -\frac{\chi_B}{1 + 4\omega_B^2/\Gamma^2}, \quad (6.19)$$

where Γ is the gain bandwidth, χ_B is a positive constant describing the strength of the gain at the line center, and the angular frequency ω_B is referenced to the gain center (i.e., detuning relative to gain center). By the Kramers-Kronig relations, χ_I necessarily leads to the real part of the susceptibility χ_R through the relation,

$$\chi_R(\omega_B) = \frac{1}{\pi} \int_{-\infty}^{\infty} \frac{\chi_I(\omega'_B)}{\omega'_B - \omega_B} d\omega'_B = \chi_B \frac{2\omega_B/\Gamma}{1 + 4\omega_B^2/\Gamma^2}. \quad (6.20)$$

The refractive index can be written as $n(\omega_B)^2 = n^2 + \chi_R + i\chi_I$, where n is the material refractive index (dispersion in n has been ignored). Assuming $\chi_B \ll n^2$, we can find the real part n' and imaginary part n'' of the refractive index:

$$n' = n + \frac{\chi_R}{2n} = n + \frac{\chi_B}{2n} \frac{2\omega_B/\Gamma}{1 + 4\omega_B^2/\Gamma^2}, \quad (6.21)$$

$$n'' = \frac{\chi_I}{2n} = -\frac{\chi_B}{2n} \frac{1}{1 + 4\omega_B^2/\Gamma^2}. \quad (6.22)$$

The α factor can then be obtained as,

$$\alpha = -\frac{\partial n'/\partial \chi_B}{\partial n''/\partial \chi_B} = \frac{2\omega_B}{\Gamma}. \quad (6.23)$$

Setting $\omega_B = \delta\Omega$ recovers the desired result, $\alpha = 2\delta\Omega/\Gamma$. There are different conventions regarding the sign of α , and here we choose the negative sign which would be consistent with the $\exp(-i\omega t)$ phasor used throughout.

To further establish the connection of α to linewidth broadening, the SBL linewidth is derived. We will again assume $\Gamma \gg \gamma$ and defer the more general case to the next subsection. For this analysis we add classical noise terms to Eqs. (6.9) and (6.10),

$$\frac{da}{dt} = -\frac{\gamma}{2} (1 + i\alpha) a - ig_{\text{B}} A b^* + f_a(t), \quad (6.24)$$

$$\frac{db}{dt} = -\frac{\Gamma}{2} (1 + i\alpha) b - ig_{\text{B}} A a^* + f_b(t), \quad (6.25)$$

where f_a and f_b are classical noise operators for the Stokes and phonon mode, respectively, satisfying the following correlations:

$$\langle f_a^*(t + \tau) f_a(t) \rangle = 0, \quad (6.26)$$

$$\langle f_b^*(t + \tau) f_b(t) \rangle = n_{\text{th}} \Gamma \delta(\tau), \quad (6.27)$$

and n_{th} is the number of thermal quanta in the phonon mode (thermal quanta in the optical modes are negligible at room temperature).

Adiabatically eliminating b gives

$$\frac{da}{dt} = \left(-\frac{\gamma}{2} + \frac{g|A|^2}{1 + \alpha^2} \right) (1 + i\alpha) a + \tilde{f}_a(t), \quad (6.28)$$

$$\tilde{f}_a \equiv f_a - \frac{ig_{\text{B}} A}{1 - i\alpha} \frac{2}{\Gamma} f_b^*, \quad (6.29)$$

where we defined a composite fluctuation term \tilde{f}_a for the SBL. Its correlation reads

$$\begin{aligned} \langle \tilde{f}_a^*(t) \tilde{f}_a(0) \rangle &= \langle f_a^*(t) f_a(0) \rangle + \frac{g_{\text{B}}^2 |A|_0^2}{1 + \alpha^2} \frac{4}{\Gamma^2} \langle f_b^*(t) f_b(0) \rangle \\ &= n_{\text{th}} \gamma \delta(t), \end{aligned} \quad (6.30)$$

which is independent of α . Applying a standard linewidth analysis, the SBL linewidth is found as:

$$\Delta\omega_{\text{SBL}} = \frac{\gamma}{2N_a} n_{\text{th}} (1 + \alpha^2), \quad (6.31)$$

where $N_a = |a|^2$ is the steady-state photon number in the Stokes mode. This is readily shown to agree with Eq. 6.3 in the limit of $\Gamma \rightarrow \infty$ when expressed in terms of output SBL power.

Full analysis of the Brillouin laser noise

Here, a more complete analysis of the SBL frequency noise is presented that includes both the effect of the pumping noise and also does not make the adiabatic

approximation (i.e., $\Gamma \gg \gamma$). The equations of motion for the Stokes, phonon and pump mode amplitudes, with damping and pumping terms, are:

$$\frac{da}{dt} = -\frac{\gamma}{2} (1 + i\alpha) a - ig_B A b^*, \quad (6.32)$$

$$\frac{db}{dt} = -\frac{\Gamma}{2} (1 + i\alpha) b - ig_B A a^*, \quad (6.33)$$

$$\frac{dA}{dt} = -\left(\frac{\gamma}{2} + i\delta\omega_P\right) A - ig_B a b + \sqrt{\kappa} A_{\text{in}}, \quad (6.34)$$

where the pump and Stokes mode have the same decay rate γ , κ is the external coupling rate, $A_{\text{in}} > 0$ is the external pumping amplitude (normalized to photon rate), and the other symbols have the same meaning as in the previous subsection.

It is convenient to work with amplitude ($|a|$, $|b|$, $|A|$) and phase ($\phi_a = \ln(a/a^*)/(2i)$, similar definitions for ϕ_b and ϕ_A) variables. Their equations can be rewritten as:

$$\frac{d|a|}{|a|dt} = -\frac{\gamma}{2} + g_B \frac{|A||b|}{|a|} \sin \theta, \quad (6.35)$$

$$\frac{d|b|}{|b|dt} = -\frac{\Gamma}{2} + g_B \frac{|A||a|}{|b|} \sin \theta, \quad (6.36)$$

$$\frac{d|A|}{|A|dt} = -\frac{\gamma}{2} - g_B \frac{|a||b|}{|A|} \sin \theta + \sqrt{\kappa} \frac{A_{\text{in}}}{|A|} \cos \phi_A, \quad (6.37)$$

$$\frac{d\phi_a}{dt} = -\frac{\gamma}{2}\alpha - g_B \frac{|A||b|}{|a|} \cos \theta, \quad (6.38)$$

$$\frac{d\phi_b}{dt} = -\frac{\Gamma}{2}\alpha - g_B \frac{|A||a|}{|b|} \cos \theta, \quad (6.39)$$

$$\frac{d\phi_A}{dt} = -\delta\omega_P - g_B \frac{|a||b|}{|A|} \cos \theta - \sqrt{\kappa} \frac{A_{\text{in}}}{|A|} \sin \phi_A, \quad (6.40)$$

where we defined the phase difference $\theta = \phi_A - \phi_a - \phi_b$. The steady-state solutions (indicated by a subscript 0) are given by:

$$\cos \theta_0 = -\frac{\alpha}{\sqrt{1 + \alpha^2}}, \quad (6.41)$$

$$\sin \theta_0 = \frac{1}{\sqrt{1 + \alpha^2}}, \quad (6.42)$$

$$|A|_0^2 = \frac{\gamma}{2g} (1 + \alpha^2), \quad (6.43)$$

$$|b|_0^2 = \frac{\gamma}{\Gamma} N_a, \quad (6.44)$$

$$\sqrt{\kappa} A_{\text{in}} \cos \phi_{A,0} = |A|_0 \left(\frac{\gamma}{2} + \frac{g N_a}{1 + \alpha^2} \right), \quad (6.45)$$

$$\delta\omega_P = \frac{\alpha}{1 + \alpha^2} g N_a - \sqrt{\kappa} \frac{A_{\text{in}}}{|A|_0} \sin \phi_{A,0}, \quad (6.46)$$

where we used the definition $g = 2g_B^2/\Gamma$. Also, although we expressed everything in terms of SBL photon numbers $N_a \equiv |a|_0^2$, it is the input amplitude A_{in} that determines N_a .

Because the pump mode is Pound-Drever-Hall (PDH) locked to the cavity resonance $\phi_{A,0} = 0$. Thus, the input amplitude and detuning can be further simplified as:

$$\sqrt{\kappa} A_{\text{in},0} = \left(\frac{\gamma}{2} + \frac{g N_a}{1 + \alpha^2} \right) \sqrt{\frac{\gamma}{2g}} \sqrt{1 + \alpha^2}, \quad (6.47)$$

$$\delta\omega_{P,0} = \frac{\alpha}{1 + \alpha^2} g N_a. \quad (6.48)$$

We note that the $\delta\omega_{P,0}$ obtained here is, up to zeroth order of γ/Γ , equal to the negative of beatnote change between the pump and SBL signals induced by amplitude-phase coupling, as measured in Fig. 6.2(a).

After the steady-state solutions are obtained, the dynamical equations are linearized by defining relative amplitude change variables (e.g., $\delta a = |a|/|a|_0 - 1$) and phase change variables (e.g., $\delta\phi_a = \phi_a - \phi_{a,0}$). Also, Langevin terms are added to the right side of the equations. These are, as before, classical and include only the thermal noise contributions. The linearized equations with noise terms are:

$$\frac{d\delta a}{dt} = \frac{\gamma}{2} (\delta A + \delta b - \delta a - \alpha\delta\theta) + f_{\delta a}, \quad (6.49)$$

$$\frac{d\delta b}{dt} = \frac{\Gamma}{2} (\delta A + \delta a - \delta b - \alpha\delta\theta) + f_{\delta b}, \quad (6.50)$$

$$\frac{d\delta A}{dt} = -\frac{\gamma}{2} \delta A - \frac{g N_a}{1 + \alpha^2} (\delta a + \delta b - \alpha\delta\theta), \quad (6.51)$$

$$\frac{d\delta\phi_a}{dt} = \frac{\gamma}{2} (\alpha\delta A + \alpha\delta b - \alpha\delta a + \delta\theta) + f_{\delta\phi,a}, \quad (6.52)$$

$$\frac{d\delta\phi_b}{dt} = \frac{\Gamma}{2} (\alpha\delta A + \alpha\delta a - \alpha\delta b + \delta\theta) + f_{\delta\phi,b}, \quad (6.53)$$

$$\frac{d\delta\phi_A}{dt} = \frac{g N_a}{1 + \alpha^2} (\alpha\delta a + \alpha\delta b - \alpha\delta A + \delta\theta) - \left(\frac{\gamma}{2} + \frac{g N_a}{1 + \alpha^2} \right) (\delta\phi_A + f_{\delta\phi,A}), \quad (6.54)$$

where f_z represents noise input to the variable z . It is convenient to switch to the frequency domain using $d/dt \rightarrow i\omega$. The power spectral density of each noise term can be written as:

$$S_{f,\delta a} = S_{f,\delta\phi,a} = 0, \quad (6.55)$$

$$S_{f,\delta b} = S_{f,\delta\phi,b} = \frac{n_{\text{th}}}{2} \frac{\Gamma}{|b|_0^2}, \quad (6.56)$$

$$S_{f,\delta\phi,A} = S_{\phi,\text{Pump}}, \quad (6.57)$$

where $S_{\phi,\text{Pump}}$ is the input phase noise contributed by the pump, and each noise term is independent of others. We have ignored the relative intensity noise of the pump, but it can also be analyzed similarly.

The above linear equations can be directly inverted, and the solution for $\delta\phi_a$ is, to the lowest order in ω :

$$\delta\phi_a = \frac{i}{(\gamma + \Gamma)\omega} (\alpha\Gamma f_{\delta a} - \alpha\gamma f_{\delta b} - \Gamma f_{\delta\phi,a} + \gamma f_{\delta\phi,b}) - \frac{\gamma}{\gamma + \Gamma} f_{\delta\phi,A}, \quad (6.58)$$

where the lowest order of ω approximation remains valid when $\omega \ll \gamma$. From here we obtain the phase noise of the SBL,

$$S_{\phi,\text{SBL}} = \frac{\alpha^2\Gamma^2 S_{f,\delta a} + \alpha^2\gamma^2 S_{f,\delta b} - \Gamma^2 S_{f,\delta\phi,a} + \gamma^2 S_{f,\delta\phi,b}}{(\gamma + \Gamma)^2\omega^2} + \left(\frac{\gamma}{\gamma + \Gamma}\right)^2 S_{f,\delta\phi,A}, \quad (6.59)$$

$$S_{\phi,\text{SBL}} = \frac{\Gamma^2 (1 + \alpha^2)}{(\gamma + \Gamma)^2\omega^2} \frac{\gamma}{2N_a} n_{\text{th}} + \left(\frac{\gamma}{\gamma + \Gamma}\right)^2 S_{\phi,\text{Pump}}. \quad (6.60)$$

Converting to frequency noise gives,

$$S_{\nu,\text{SBL}} = \frac{\Gamma^2 (1 + \alpha^2)}{4\pi^2(\gamma + \Gamma)^2} \frac{\gamma}{2N_a} n_{\text{th}} + \left(\frac{\gamma}{\gamma + \Gamma}\right)^2 S_{\nu,\text{Pump}}. \quad (6.61)$$

Thus, the fundamental linewidth of the SBL is given by

$$\Delta\omega_{\text{SBL}} = \left(\frac{\Gamma}{\gamma + \Gamma}\right)^2 (1 + \alpha^2) \frac{\gamma}{2N_a} n_{\text{th}}. \quad (6.62)$$

Note that the above derivation automatically incorporates non-adiabaticity and the linewidth enhancement factor. Also, the transduction of the pump phase noise is, when the pump mode is PDH locked,

$$S_{\nu,\text{SBL}} = \left(\frac{\gamma}{\gamma + \Gamma}\right)^2 S_{\nu,\text{P}}, \quad (6.63)$$

and is independent of the α factor.

We briefly comment on the noise behavior when $\delta\omega_{\text{p}}$ is tuned away from its PDH-locked value, which happens because the PDH locking can reduce, but not totally eliminate, the drifting in $\delta\omega_{\text{p}}$. Repeating the previous analyses, we arrive at the

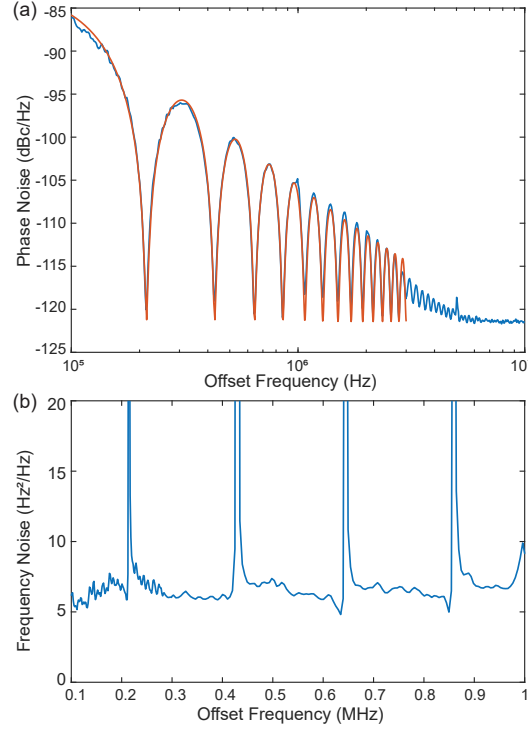


Figure 6.4: **Illustration for SBL noise measurement and fitting.** (a) Blue curve is the measured phase noise spectrum from the self-heterodyne output when pump wavelength is 1538 nm and SBL power is 1.29 mW. Red curve is the fitting according to Eq. (6.69) to obtain the frequency noise S . (b) The converted frequency noise spectrum from panel (a).

following expression for $S_{v,\text{SBL}}$ and expand it as a series in the relative variation of detuning:

$$\frac{S_{v,\text{SBL}}}{S_{v,\text{P}}} \approx \left(\frac{\gamma}{\gamma + \Gamma} \right)^2 + \alpha^2 \left(\frac{\gamma}{\gamma + \Gamma} \right) \left(\frac{\delta\omega_{\text{P}}}{\delta\omega_{\text{P},0}} - 1 \right) + \frac{\alpha^4}{4} \left(\frac{\delta\omega_{\text{P}}}{\delta\omega_{\text{P},0}} - 1 \right)^2, \quad (6.64)$$

where we have kept only the lowest-order term in γ/Γ for each coefficient. As the last term no longer contains the γ/Γ reduction, the phase noise transduction is strongly dependent upon α . Thus an imperfect PDH locking increases the transferred pump phase noise in proportion to α^2 .

6.6 Additional measurements and information

Frequency discriminator measurements

Here the frequency noise measurement is studied to arrive at the transfer function that relates the measured phase noise spectrum (Fig. 6.4(a)) to the frequency noise spectral density S plotted in Fig. 6.3. As shown in the Supplement Information of the previous work in our group [37], pump noise conversion is believed to be the

dominant noise source at low offset frequency, while white Schawlow-Townes-like noise dominants at high offset frequency (usually over 100 kHz).

For white frequency noise, the correlation of the time derivative of the phase satisfies,

$$\langle \dot{\phi}(t + \tau) \dot{\phi}(t) \rangle = \Delta\omega_N \delta(\tau), \quad (6.65)$$

where $\Delta\omega_N$ is the Lorentzian full-width-at-half-maximum linewidth in rad/s, including both fundamental ($\Delta\omega_{\text{SBL}}$) and technical contributions. The two-sided spectral density function for the instantaneous frequency $\nu \equiv \dot{\phi}/(2\pi)$ is given by the Fourier transform of the correlation function:

$$S_w = \frac{1}{4\pi^2} \int_{-\infty}^{\infty} \langle \dot{\phi}(t + \tau) \dot{\phi}(t) \rangle e^{-2\pi i f \tau} d\tau = \frac{\Delta\omega_N}{4\pi^2}, \quad (6.66)$$

where S_w is the white frequency noise spectral density as in the previous sections.

On account of the time delayed path in the frequency discrimination system, the detected output returns a signal with a noisy phase $\phi(t + \tau) - \phi(t)$, where τ is the interferometer delay. We are thus interested in the frequency noise of $\nu(\tau) \equiv (\dot{\phi}(t + \tau) - \dot{\phi}(t))/(2\pi)$. By the time-shifting property of the Fourier transform,

$$S_{\nu(\tau)}(f) = S_w(2 - e^{2\pi i f \tau} - e^{-2\pi i f \tau}) = 4 \sin^2(\pi f \tau) S_w. \quad (6.67)$$

The detected output from the self-heterodyne interferometer is analyzed by a phase noise analyzer. Therefore, converting to phase noise gives,

$$S_{\phi(\tau)}(f) = \frac{1}{f^2} S_{\nu(\tau)}(f) = 4 \frac{\sin^2(\pi f \tau)}{f^2} S_w. \quad (6.68)$$

A typical measured phase-noise spectrum is shown in Fig. 6.4(a). In fitting the spectrum, there is both the sinc^2 -shaped noise spectrum contributed by the SBL laser, and a noise floor contributed by the photodetector noise equivalent power (NEP). Thus, the following equation is used to describe the total phase noise,

$$S_{\text{Total},\phi}(f) = S_{\text{NEP}} + 4\pi^2 \tau^2 \text{sinc}^2(\pi f \tau) S_w, \quad (6.69)$$

where $\text{sinc}(z) \equiv \sin z/z$, $S_{\text{Total},\phi}(f)$ is the total measured phase noise, and S_{NEP} is the NEP contributed phase noise (determined by averaging the measured phase noise between 8 MHz to 10 MHz). S_w and the time delay τ are fitting parameters in the measurement (the fiber delay has around 1 km length and therefore provides an approximate delay of $\tau \approx 4.67 \mu\text{s}$). The fitting is performed within the frequency

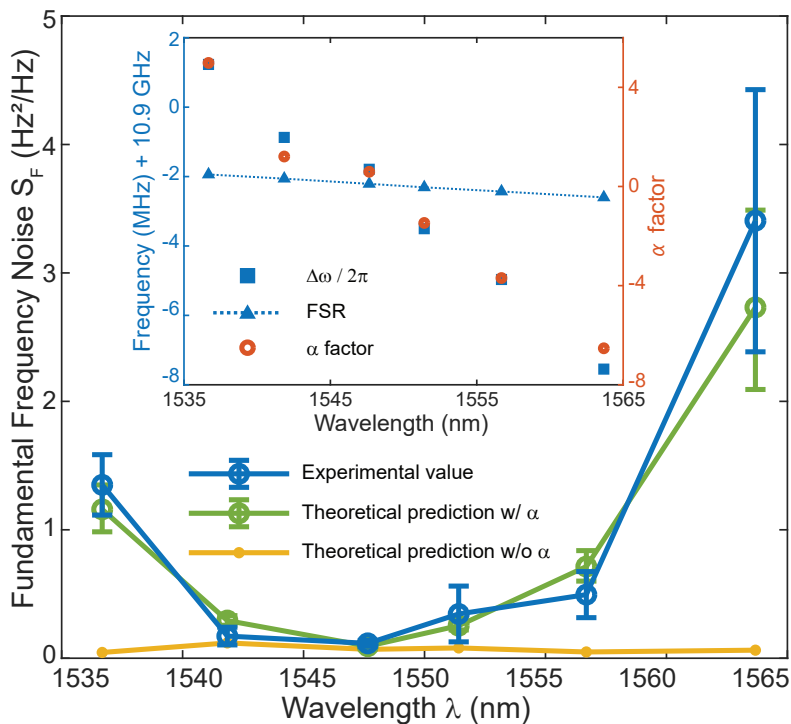


Figure 6.5: **SBL frequency noise enhancement measured using a second device.** Measured SBL fundamental frequency noise S_F (blue); theoretical S_F prediction (green) with α obtained from the plot provided in the inset. The non-enhanced S_0 formula ($\alpha=0$) prediction (yellow) is also shown. All data are plotted versus pump wavelength and normalized to 1 mW output power. Inset: The extrapolated beating frequency (squares) and FSR (triangles) are plotted versus wavelength. The calculated α factor (red circles) is plotted versus wavelength.

range between 0.1 MHz and 3 MHz, since technical noise becomes significant below 0.1 MHz, while the fringe contrast is reduced for frequencies higher than 3 MHz on account of reduced resolution.

To explicitly illustrate the measured noise is approximately white over this frequency range, we convert the phase noise from discriminator measurement to frequency noise by dividing out the response function, $4\pi^2\tau^2\text{sinc}^2(\pi f\tau)$. As shown in Fig. 6.4(b), the overall frequency noise is nearly white except for some spikes resulting from zeros in the response function in combination with the NEP noise contributions.

Noise enhancement measured in a second device

To verify the generality of our findings, we have performed the experiment on another device and summarized the main data in Fig. 6.5. Data definition and calculation methods are the same as the previous sections. In the measurement, we

have chosen six longitudinal modes in one transverse mode family. This device has a lowest frequency noise S_F of $0.10 \text{ Hz}^2/\text{Hz}$ and the measured α factor is as large as 6. The measured noise enhancement is overall in good agreement with the α factor predictions.

6.7 Discussion

We have studied the linewidth enhancement factor α in a Brillouin laser. A modification to the fundamental linewidth formula that incorporates the α factor was theoretically derived and then tested experimentally in a high-Q silica whispering gallery resonator. Phase matching of the Brillouin process determines the sign and magnitude of α . Under perfect phase-matching conditions, corresponding to laser oscillation at the Brillouin gain maximum, $\alpha=0$. However, measurement and theory show that the mismatch (induced here by tuning of the pumping wavelength) leads to α factors greater than 7 yielding frequency noise and fundamental linewidth enhancement as large as $50\times$. The sign of α can also be controlled through the sign of the frequency mismatch detuning. Although the phase-matching condition was controlled here by tuning of pumping wavelength, it should also be possible to vary phase matching and therefore α through control of the temperature. This would vary the Brillouin shift frequency by way of the temperature dependence of the sound velocity. The results presented here stress the importance of proper pumping wavelength selection and observance of temperature control for narrow linewidth operation of SBLs. These considerations will be important in all applications of these devices that are sensitive to frequency noise and linewidth.

Chapter 7

PETERMANN-FACTOR SENSITIVITY LIMIT NEAR AN EXCEPTIONAL POINT IN A BRILLOUIN RING LASER GYROSCOPE

7.1 Introduction

¹ Non-Hermitian Hamiltonians [172, 173] describing open systems can feature singularities called exceptional points (EPs) [174, 175, 176]. EPs have been experimentally realized in several systems [177, 178, 179] and applied to demonstrate non-reciprocal transmission [180, 181, 182] and lasing dynamics control [183, 184, 185, 186]. Moreover, resonant frequencies become strongly dependent on externally applied perturbations near an EP which has given rise to the concept of EP-enhanced sensing in photonics [187, 188, 189, 190] and electronics [191, 192]. While increased sensor responsivity has been demonstrated in several systems [193, 194, 59, 195], signal-to-noise performance (sensitivity) has been considered only theoretically [196, 197, 198, 199, 200].

Recently, strong responsivity improvement near an EP was reported in a Brillouin ring laser gyroscope by monitoring an increase in the gyroscope scale factor (i.e., transduction factor of rotation-rate into a signal) [59]. At the same time, however, measurement of the gyroscope Allan deviation versus averaging time showed that short-term laser frequency noise also increased near the EP. This noise was random-walk in nature, suggesting a fundamental origin. Moreover, it depended upon system bias relative to the EP in such a way so as to precisely compensate the observed EP-enhanced transduction. As a result, the gyroscope's angular random walk, the metric used to quantify short-term rotation sensitivity, was observed to maintain a constant value (i.e., independent of gyroscope bias relative to the EP). In effect, the measurements showed that gyroscope sensitivity (i.e., weakest rotation signal measurable at a given detection bandwidth) is not improved by operation near the EP even while the gyroscope responsiveness through improved transduction (scale factor) increases.

As with all laser gyroscopes, the Brillouin ring laser gyroscope measures rotations

¹Work presented in this chapter has been published in [153] "Petermann-factor sensitivity limit near an exceptional point in a Brillouin ring laser gyroscope." *Nature Communications* 11.1 (2020), p. 1610.

through the Sagnac effect [201]. Clockwise (cw) and counter-clockwise (ccw) lasing waves experience opposing frequency shifts when the plane of the gyroscope rotates. By mixing the two laser fields on a detector, their difference frequency therefore reveals the rotation-induced frequency shift added onto a constant bias frequency (which is at audio rates in this case [59]). Frequency noise in the beat frequency therefore determines the measurement sensitivity. This noise has both a technical component (observable on longer time scales in the Allan deviation [59]) as well as a random walk component that, absent the EP, is known to result from fundamental linewidth broadening of the Brillouin laser waves [59, 42]. Significantly, subsequent measurement of the random walk component showed that none of the parameters which normally impact its magnitude (e.g., laser power, cavity Q factor) varied near the EP, therefore suggesting that frequency noise (and linewidth) is increased by way of another mechanism.

Laser linewidth can also be broadened by the Petermann factor [202, 203, 204, 205, 206, 207]. This mechanism is associated with non-orthogonality of a mode spectrum, and its connection to EPs has been considered in theoretical studies of microresonators [208, 209]. However, despite continued theoretical interest [210, 211], including the development of new techniques for determination of linewidth in general laser systems [212], the observation of Petermann linewidth broadening near exceptional points was reported only recently by the Yang group in a phonon laser system [213]. And the link between Petermann-factor-induced noise and EP sensor performance is unexplored. Here, it is shown that mode non-orthogonality induced by the EP limits the gyroscope sensitivity via Petermann-factor linewidth broadening. Indeed, analysis and measurement confirm near perfect cancellation of the signal transduction improvement by increasing Petermann-factor noise so that the gyroscope's fundamental signal-to-noise ratio (SNR) and hence sensitivity is not improved by operation near the EP. These results are further confirmed using an Adler phase locking equation approach [214, 215] which is also applied to analyze the combined effect of dissipative and conservative coupling on the system.

7.2 Biorthogonal Noise Enhancement Theory

The gyroscope uses a high-Q silica whispering gallery resonator [37] in a ring-laser configuration [46]. As illustrated in Fig. 7.1(a), optical pumping of cw and ccw directions on the same whispering-gallery mode index induces laser action through the Brillouin process. On account of the Brillouin phase matching condition, these stimulated Brillouin laser (SBL) waves propagate in a direction opposite to their

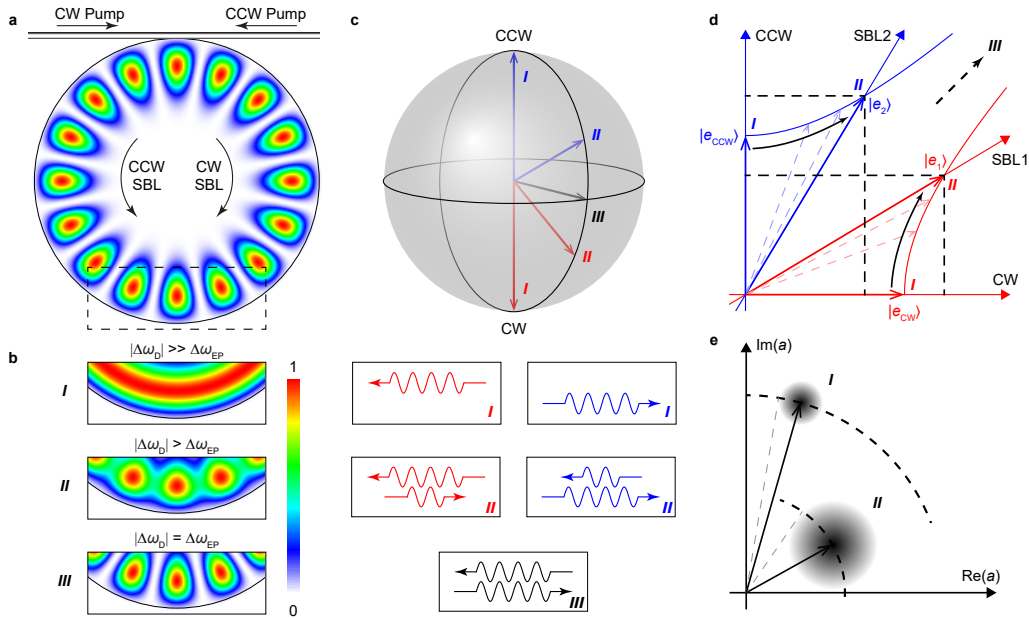


Figure 7.1: **Brillouin laser linewidth enhancement near an exceptional point.**

(a) Diagram of whispering-gallery mode resonator with the energy distribution of an eigenmode superimposed. The eigenmode energy distribution corresponds to state III in panel (b). Optical pumps on the coupling waveguide and whispering-gallery SBL modes are indicated by arrows. (b) Mode energy distributions for three different states: far from EP (state I) the eigenmodes are traveling cw or ccw waves; near EP (state II) the eigenmodes are hybrids of cw and ccw waves; at EP (state III) eigenmodes coalesce to a standing wave. (c) Bloch sphere showing the eigenstates for cases I, II and III with corresponding cw and ccw composition. (d) Illustration of the cw-ccw and SBL1-SBL2 coordinate systems. Unit vectors for states I and II are shown on each axis. As the system is steered towards the EP, the SBL axes move toward each other so that unit vectors along the SBL axes lengthen as described by the two hyperbolas. This is illustrated by decomposing a unit vector of the non-orthogonal SBL coordinate system using the orthogonal cw-ccw coordinates [e.g., $(5/4, 3/4)^T$ and $(3/4, 5/4)^T$ for state II]. Consequently, the field amplitude is effectively shortened in the SBL basis. (e) Phasor representation of the complex amplitude of a lasing mode for states I and II provides an interpretation of linewidth enhancement. Phasor length is shortened and noise is enhanced as the system is steered to the EP, leading to an increased phasor angle diffusion and laser linewidth enhancement.

corresponding pump waves [42]. Dissipative backscattering [216] couples the SBLs and the following Hamiltonian governs the above-laser-threshold motion [59]:

$$H = \begin{pmatrix} \omega_{cw} & i\Delta\omega_{EP}/2 \\ i\Delta\omega_{EP}/2 & \omega_{ccw} \end{pmatrix}, \quad (7.1)$$

where H describes the dynamics via $id\Psi/dt = H\Psi$ and $\Psi = (a_{cw}, a_{ccw})^T$ is the column vector of SBL mode amplitudes (square of norm is photon number). Also, $\Delta\omega_{EP}$ is a non-Hermitian term related to the coupling rate between the two SBL modes and ω_{cw} (ω_{ccw}) is the active-cavity resonance angular frequency of the cw (ccw) SBL mode above laser threshold. The dependence of ω_{cw} , ω_{ccw} and $\Delta\omega_{EP}$ on other system parameters, most notably the angular rotation rate and the optical pumping frequencies, has been suppressed for clarity.

A class of EP sensors operate by measuring the frequency difference of the two system eigenmodes. This difference is readily calculated from Eq. (7.1) as $\Delta\omega_S = \sqrt{\Delta\omega_D^2 - \Delta\omega_{EP}^2}$ where $\Delta\omega_D \equiv \omega_{ccw} - \omega_{cw}$ is the resonance frequency difference and $\Delta\omega_{EP}$ is the critical value of $\Delta\omega_D$ at which the system is biased at the EP. As illustrated in Fig. 7.1(b,c) the vector composition of the SBL modes strongly depends upon the system proximity to the EP. For $|\Delta\omega_D| \gg \Delta\omega_{EP}$ the SBL modes (unit vectors) are orthogonal cw and ccw waves. However, closer to the EP the waves become admixtures of these states that are no longer orthogonal. At the EP, the two waves coalesce to a single state vector (a standing wave in the whispering gallery). Rotation of the gyroscope in state II in Fig. 7.1 ($|\Delta\omega_D| > \Delta\omega_{EP}$) introduces a perturbation to $\Delta\omega_D$ whose transduction into $\Delta\omega_S$ is enhanced relative to the conventional Sagnac factor [201]. This EP-induced signal-enhancement-factor (SEF) is given by [59]:

$$\text{SEF} = \left| \frac{\partial\Delta\omega_S}{\partial\Delta\omega_D} \right|^2 = \frac{\Delta\omega_D^2}{\Delta\omega_D^2 - \Delta\omega_{EP}^2}, \quad (7.2)$$

where SEF refers to the signal power (not amplitude) enhancement. This factor has recently been verified in the Brillouin ring laser gyroscope [59]. The control of $\Delta\omega_D$ (and in turn $\Delta\omega_S$) in that work and here is possible by tuning of the optical pumping frequencies and is introduced later.

$\Delta\omega_S$ is measured as the beat frequency of the SBL laser signals upon photodetection and the SNR is set by the laser linewidth. To understand the linewidth behavior a bi-orthogonal basis is used (Supplementary Note [153]). As shown there and illustrated in Fig. 7.1(d), the peculiar properties of non-orthogonal systems near the EP cause the unit vectors (optical modes) to be lengthened. This lengthening results

in an effectively shorter laser field amplitude. Also, noise into the mode is increased as illustrated in Fig. 7.1(e). Because the laser linewidth can be understood to result from diffusion of the phasor in Fig. 7.1(e), linewidth increases upon operation close to the EP. And the linewidth enhancement is given by the Petermann factor (Supplementary Note 3 [153]):

$$\text{PF} = \frac{1}{2} \left(1 + \frac{\text{Tr}(H_0^\dagger H_0)}{|\text{Tr}(H_0^2)|} \right) = \frac{\Delta\omega_D^2}{\Delta\omega_D^2 - \Delta\omega_{\text{EP}}^2}, \quad (7.3)$$

where Tr is the matrix trace operation and $H_0 = H - \text{Tr}(H)/2$ is the traceless part of H . As derived in Supplementary Note 2, the first part of this equation is a basis independent form and is valid for a general two-dimensional system. The second part is specific to the current SBL system. Inspection of Eq. (7.2) and Eq. (7.3) shows that $\text{SEF} = \text{PF}$. As a result the SNR is not expected to improve through operation near the EP when the system is fundamental-noise limited.

7.3 Measurement on the Petermann factor enhanced fundamental noise

To verify the above predictions, the output of a single pump laser (~ 1553.3 nm) is divided into two branches that are coupled into cw and ccw directions of the resonator using a tapered fiber [62, 63]. Both pump powers are actively stabilized. The resonator is mounted in a sealed box and a thermo-electric cooler (TEC) controls the chip temperature which is monitored using a thermistor (fluctuations are held within 5 mK). Each pumping branch has its frequency controlled using acousto-optic modulators (AOMs). SBL power is also monitored and controlled so that fluctuations are within 0.6%. Even with the control of temperature and power, the Allan deviation at longer gate times reflects technical-noise drifting that is observed to be more pronounced for operation near the EP. As described in Ref. [59], the ccw pump laser frequency is Pound-Drever-Hall (PDH) locked to one resonator mode and the cw pump laser can then be independently tuned by the AOM. This pump detuning frequency ($\Delta\omega_P$) is therefore controlled to radio-frequency precision. It is used to precisely adjust $\Delta\omega_D$ and in turn $\Delta\omega_S$ as shown in three sets of measurements in Fig. 7.2(a). Here, the photodetected SBL beat frequency $\Delta\omega_S$ is measured using a frequency counter. The data sets are taken for three distinct SBL output amplitude ratios as discussed further below. A solid curve fitting is also presented using $\Delta\omega_S = \pm\sqrt{\Delta\omega_D^2 - \Delta\omega_{\text{EP}}^2}$, where $\Delta\omega_D = \frac{\gamma/\Gamma}{1+\gamma/\Gamma}\Delta\omega_P + \frac{1}{1+\gamma/\Gamma}\Delta\omega_{\text{Kerr}}$ (Supplementary Note 4 [153]). Also, γ is the photon decay rate, Γ is the Brillouin gain bandwidth [42], and $\Delta\omega_{\text{Kerr}}$ is a Kerr effect correction that is explained below. As an aside, the

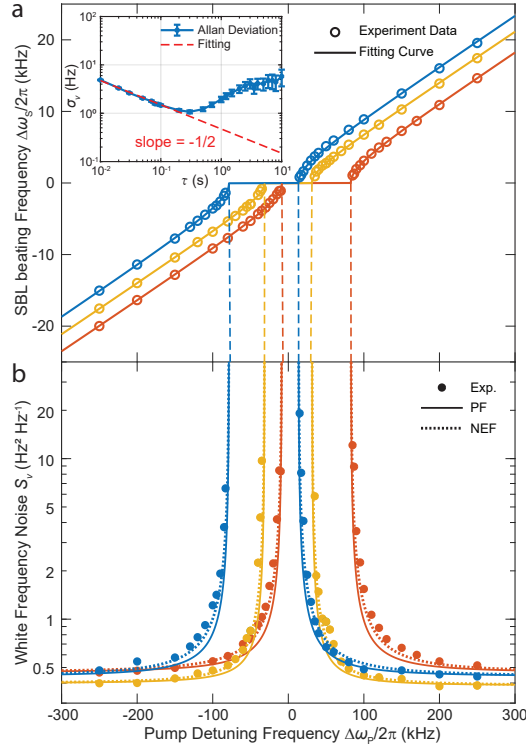


Figure 7.2: **Measured linewidth enhancement of SBLs near the exceptional point.** (a) Measured SBL beating frequency is plotted versus pump detuning for three distinct locking zones, corresponding SBL amplitude ratios q : 1.15 (blue), 1 (orange), 0.85 (red). Solid curves are theoretical fittings. Inset is a typical Allan deviation measurement of frequency ($\sigma_\nu(\tau)$) versus gate time τ . Error bars give the standard error of the mean. The short-term part is fitted with $\sqrt{S_\nu/(2\tau)}$ where S_ν is the one-sided power spectral density of the white frequency noise plotted in panel (b). (b) Measured white frequency noise of the beating signal determined using the Allan deviation measurement. Data point color corresponds to the amplitude ratios used in panel (a). The Petermann factor PF (solid lines) and NEF (dashed lines) theoretical predictions use parameters obtained by fitting from panel (a).

data plot and theory show a frequency locking zone, the boundaries of which occur at the EP.

The frequency counter data are also analyzed as an Allan deviation (Adev) measurement (Fig. 7.2(a) inset). The initial roll-off of the Adev features a slope of $-1/2$ corresponding to white frequency noise [217]. This was also verified in separate measurements of the beat frequency using both an electrical spectrum analyzer and a fast Fourier transform. The slope of this region is fit to $\sqrt{S_\nu/(2\tau)}$ where S_ν is the one-sided spectral density of the white frequency noise. Adev measurement at each of the detuning points in Fig. 7.2(a) is used to infer the S_ν values that

are plotted in Fig. 7.2(b). There, a frequency noise enhancement is observed as the system is biased towards an EP. Also plotted is the Petermann factor noise enhancement (Eq. (7.3)). Aside from a slight discrepancy at intermediate detuning frequencies (analyzed further below), there is overall excellent agreement between theory and measurement. The frequency noise levels measured in Fig. 7.2(b) are consistent with fundamental SBL frequency noise (see Methods). Significantly, the fundamental nature of the noise, the good agreement between the PF prediction (Eq. (7.3)) and measurement in Fig. 7.2(b), and separate experimental work [59] that has verified the theoretical form of the SEF (Eq. (7.3)) confirm that $\text{SEF} = \text{PF}$ so that the fundamental sensitivity limit of the gyroscope is not improved by operation near the EP.

7.4 Adler analysis on the enhanced noise and locking bandwidth

While the Petermann factor analysis provides very good agreement with the measured results, we also derived an Adler-like coupled mode equation analysis for the Brillouin laser system. This approach is distinct from the bi-orthogonal framework and, while more complicated, provides additional insights into the system behavior. Adapting analysis applied in the noise analysis of ring laser gyroscopes [215], a noise enhancement factor NEF results (see Supplementary Note 4 [153]):

$$\text{NEF} = \frac{\Delta\omega_{\text{D}}^2 + \Delta\omega_{\text{EP}}^2/2}{\Delta\omega_{\text{D}}^2 - \Delta\omega_{\text{EP}}^2}. \quad (7.4)$$

It is interesting that this result, despite the different physical context of the Brillouin laser system, has a similar form to one derived for polarization-mode-coupled laser systems [218]. The PF and NEF predictions are shown on Fig. 7.2(b) and the Adler-derived NEF correction provides slightly better agreement with the data at the intermediate detuning values.

The Adler approach is also useful to explain a locking zone dependence upon SBL amplitudes observed in Fig. 7.2(a). As shown in Supplementary Note 4 [153], this variation can be explained through the combined action of the Kerr effect and intermodal coupling coefficients of both dissipative and conservative nature. Specifically, the locking bandwidth is found to exhibit the following dependence upon the amplitude ratio $q = |a_{\text{ccw}}/a_{\text{cw}}|$ of the SBL lasers:

$$\Delta\omega_{\text{EP}}^2 = \left(\frac{\Gamma}{\Gamma + \gamma}\right)^2 \left[\left(q + \frac{1}{q}\right)^2 |\kappa|^2 + \left(q - \frac{1}{q}\right)^2 |\chi|^2 \right], \quad (7.5)$$

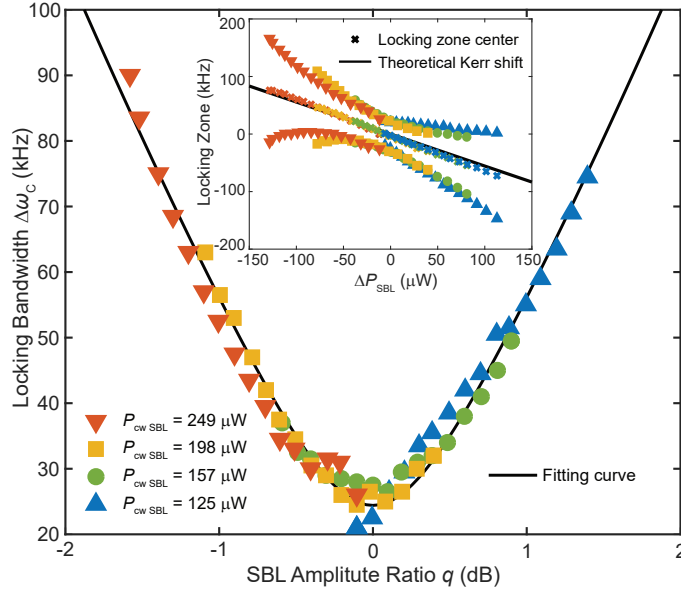


Figure 7.3: **Locking zone bandwidth versus SBL amplitude ratio.** Measured locking zone bandwidth is plotted versus amplitude ratio q of the SBL lasers. The cw power is held constant at four values (see legend) to create the data composite. The solid black curve is Eq. (7.5). Inset: the measured locking zone boundaries are plotted versus the SBL power differences ($\Delta P_{\text{SBL}} = P_{\text{ccw}} - P_{\text{cw}}$). Colors and symbols correspond to the main panel. The center of the locking zone is also indicated and is shifted by the Kerr nonlinearity which varies as the SBL power difference. Black line gives the theoretical prediction (no free parameters).

where κ is the dissipative coupling and χ is the conservative coupling between cw and ccw SBL modes. The locking zone boundaries in terms of pump detuning frequency have been measured (Fig. 7.3 inset) for a series of different SBL powers. Using this data, the locking bandwidth is expressed in pump frequency detuning ($\Delta\omega_{\text{P}}$) units using $\Delta\omega_{\text{C}} \equiv (1 + \Gamma/\gamma)\Delta\omega_{\text{EP}}$ and plotted versus q in the main panel of Fig. 7.3. The plot agrees well with Eq. (7.5) (fitting shown in black) and gives $|\kappa| = 0.93$ kHz, $|\chi| = 8.21$ kHz.

Finally, the center of the locking band is shifted by the Kerr effect and (in pump frequency detuning $\Delta\omega_{\text{P}}$ units) can be expressed as $-(\Gamma/\gamma)\Delta\omega_{\text{Kerr}}$, where $\Delta\omega_{\text{Kerr}} = \eta \left(|a_{\text{ccw}}|^2 - |a_{\text{cw}}|^2 \right) = (\eta\Delta P_{\text{SBL}})/(\gamma_{\text{ex}}\hbar\omega)$ is the Kerr induced SBL resonance frequency difference, $\Delta P_{\text{SBL}} = P_{\text{ccw}} - P_{\text{cw}}$ is the output power difference of the SBLs, and γ_{ex} is the photon decay rate due to the output coupling. Also, $\eta = n_2\hbar\omega^2c/(Vn_0^2)$ is the single-photon Kerr-effect angular frequency shift with ω the SBL angular frequency, n_2 the Kerr-nonlinear refractive index of silica, V the mode volume, n_0 the

linear refractive index, and c the speed of light in vacuum. If the white frequency noise floors in Fig. 7.2 are used to infer the resonator quality factor, then a Kerr nonlinearity value of $558 \text{ Hz } \mu\text{W}^{-1}$ is predicted (see section 7.5). This value gives the line plot in the Fig. 7.3 inset (with no free parameters) which agrees with experiment.

7.5 Additional information

Linewidth and Allan deviation measurement

In experiments, frequency is measured in the time domain using a frequency counter and its Allan deviation is calculated for different averaging times (Fig. 7.2(a)). The Allan deviation $\sigma_\nu(\tau)$ for a signal frequency is defined by:

$$\sigma_\nu(\tau) \equiv \sqrt{\frac{1}{2(M-1)} \sum_{k=1}^{M-1} (\bar{\nu}_{k+1} - \bar{\nu}_k)^2}, \quad (7.6)$$

where τ is the averaging time, M is the number of frequency measurements, and $\bar{\nu}_k$ is the average frequency of the signal (measured in Hz) in the time interval between $k\tau$ and $(k+1)\tau$. The Allan deviation follows a $\tau^{-1/2}$ dependence when the underlying frequency noise spectral density is white [217] as occurs for laser frequency noise limited by spontaneous emission. White noise causes the lineshape of the laser to be a Lorentzian. White noise is also typically dominant in the Allan deviation plot at shorter averaging times where flicker noise and frequency drift are not yet important. This portion of the Allan deviation plot can be fit using $\sigma_\nu(\tau) = \sqrt{S_\nu/(2\tau)}$ where S_ν is the white frequency noise one-sided spectral density function. This result can be further converted to the Lorentzian full-width at half maximum (FWHM) linewidth $\Delta\nu_{\text{FWHM}}$ (measured in Hz) using the conversion:

$$S_\nu = 2\sigma_\nu^2(\tau)\tau = \frac{1}{\pi}\Delta\nu_{\text{FWHM}}. \quad (7.7)$$

Experimental parameters and data fitting

The resonator is pumped at the optical wavelength $\lambda = 1553.3 \text{ nm}$, which, subject to the Brillouin phase matching condition, corresponds to a phonon frequency (Stokes frequency shift) of approximately $\Omega_{\text{phonon}}/(2\pi) = 10.8 \text{ GHz}$. Quality factors of the SBL modes are measured using a Mach-Zehnder interferometer, and a loaded Q factor $Q_{\text{T}} = 88 \times 10^6$ and coupling Q factor $Q_{\text{ex}} = 507 \times 10^6$ are obtained.

The theoretical formula for the white frequency noise of the beat frequency far away

from the EP reads:

$$S_v = \left(\frac{\Gamma}{\gamma + \Gamma} \right)^2 \frac{\hbar\omega^3}{4\pi^2 Q_T Q_{\text{ex}}} \left(\frac{1}{P_{\text{cw}}} + \frac{1}{P_{\text{ccw}}} \right) (n_{\text{th}} + N_{\text{th}} + 1), \quad (7.8)$$

which results from summing the Schawlow-Townes-like linewidths of the SBL laser waves [42]. In the expression, N_{th} and n_{th} are the thermal occupation numbers of the SBL state and phonon state, respectively. At room temperature, $n_{\text{th}} \approx 577$ and $N_{\text{th}} \approx 0$. For the power balanced case (orange data set in Fig. 7.2), $P_{\text{cw}} = P_{\text{ccw}} = 215 \mu\text{W}$ and the predicted white frequency noise (Eq. 7.8) is $S_v = 0.50 \text{ Hz}^2 \text{ Hz}^{-1}$. For the blue (red) data set, P_{cw} (P_{ccw}) is decreased by 1.22 dB (1.46 dB) so that $S_v = 0.58$ (0.60) $\text{Hz}^2 \text{ Hz}^{-1}$ is calculated. On the other hand, the measured values for the blue, orange and red data sets in Fig. 7.2(b) (i.e., white frequency noise floors far from EP) give $S_v = 0.44, 0.39, 0.46 \text{ Hz}^2 \text{ Hz}^{-1}$, respectively. The difference here is attributed to errors in Q measurement. For example, the experimental values of noise can be used to infer a corrected coupling Q factor $Q_{\text{ex}} \approx 658 \times 10^6$. Using this value below yields an excellent prediction of the Kerr nonlinear coefficient which supports this belief.

The beating frequency in Fig. 7.2(a) is fit using the following relations:

$$\begin{aligned} \Delta\omega_S &= \text{sgn}(\Delta\omega_D) \sqrt{\Delta\omega_D^2 - \Delta\omega_{\text{EP}}^2}, \\ \Delta\omega_D &= \frac{\gamma/\Gamma}{1 + \gamma/\Gamma} \Delta\omega_P + \frac{1}{1 + \gamma/\Gamma} \Delta\omega_{\text{Kerr}}, \end{aligned} \quad (7.9)$$

where sgn is the sign function and γ/Γ , $\Delta\omega_{\text{Kerr}}$ and $\Delta\omega_{\text{EP}}$ are fitting parameters. The fitting gives $\gamma/\Gamma = 0.076$ consistently, while $\Delta\omega_{\text{Kerr}}$ and $\Delta\omega_{\text{EP}}$ are separately adjusted in each data set. These parameters feature a power dependence that is fully explored in Fig. 7.3.

The theoretical Kerr coefficient used in Fig. 7.3 can be calculated as follows. Assuming $n_2 \approx 2.7 \times 10^{-20} \text{ m}^2/\text{W}$, $n_0 = 1.45$ for the silica material, and $V = 10^7 \mu\text{m}^3$ (obtained through finite-element simulations for the 36mm-diameter disk used here), gives $\eta/2\pi \approx 10^{-5} \text{ Hz}$. Using the Q_{ex} corrected by the white frequency noise data (see discussion above), $\gamma_{\text{ex}}/2\pi = 299 \text{ kHz}$ so that $\Delta\omega_{\text{Kerr}}/(2\pi\Delta P_{\text{SBL}}) \approx 42 \text{ Hz } \mu\text{W}^{-1}$. When $\gamma/\Gamma = 0.076$, the center shift of pump locking band is $-(\Gamma/\gamma)\Delta\omega_{\text{Kerr}} = 558 \text{ Hz } \mu\text{W}^{-1}$. This value agrees very well with experiment (Fig. 7.3 inset).

7.6 Discussion

Prior work has shown that Brillouin laser gyroscopes when operated near an EP have an improved responsivity (equivalently, an increase in the gyroscope's scale factor for

transduction of rotation rate into the Sagnac frequency shift) [59]. At the same time, these measurements have shown that the gyroscope's sensitivity did not improve near the EP. We have verified through measurement and theory that mode non-orthogonality induced by the EP explains this latter result. Specifically, increasing mode non-orthogonality occurs when the two system eigenvectors (optical modes) begin to coalesce near the EP. This, in turn, increases laser frequency noise from an increasing Petermann factor and thereby reduces sensitivity. Curiously, these two mechanisms, the enhanced transduction and enhanced noise, feature an almost identical dependence upon the system's proximity to the EP. In effect, the increased signal response in the gyroscope arising from the EP does not lead to an improvement in the minimum detectable signal (sensitivity).

It is interesting to note that a recent theoretical study of noise limitations in a class of non-lasing EP sensors showed no fundamental sensitivity advantage for operation near the EP [198]. Nonetheless it is still possible that other sensing modalities could benefit from operation near an EP. Moreover, open systems offer other potentially useful ways for transduction of rotation [219]. Also, the proposal of conservative nonlinear mode coupling provides a potential way to enhance the Sagnac effect [220, 221, 222]. The apparent divergence of the linewidth near the EP is an interesting feature of the current model and also one that agrees well with the data (at least in the range of the measurement). Nonetheless, constraints to this divergence set by the linewidth of the passive cavity loss are a subject of further study. More generally, the excellent control of the state space that is possible in the Brillouin system can provide a new platform for study of the remarkable physics associated with exceptional points.

CORRELATED SELF-HETERODYNE METHOD FOR ULTRA-LOW-NOISE LASER LINEWIDTH MEASUREMENTS

8.1 Introduction

¹ Ultra-low-noise lasers are indispensable ingredients for a wide range of applications, including optical gyroscopes [47], optical atomic clocks [224], and light detection and ranging (LiDAR) systems [225]. Accurate measurement of ultra-low-noise frequency spectra is an essential prerequisite for optimizing their performance and advancing their applications. Hence, high demands are placed on measurement systems to characterize these lasers with low frequency noise floors and high intensity-fluctuation isolation.

Several methods have been used for laser linewidth characterization. Incoherent homodyne detection incorporates a fiber delay line exceeding the coherence length of the laser under test [226]. While the method measures relatively high frequency noise levels accurately, it becomes inappropriate as the laser linewidth reaches Hz levels, where the coherence length is on the order of 10^5 km. Phase discriminators with sub-coherent-length delay have been proposed in such cases, either by locking to a quadrature point [42, 37] or using self-heterodyne detection to shift the signal to the radiofrequency (RF) domain so as to avoid low-frequency technical noise [170, 171]. However, optical-to-electrical (OE) conversion at the photodetector (PD) introduces additional technical PD noise, and relative intensity noise (RIN) of the laser may also be coupled to the output signal through the OE conversion. These factors prevent the detection methods from achieving the sufficiently-low noise floor required for milli-Hertz-linewidth laser characterization. At the same time, cross-correlation has been applied to frequency noise characterization in the RF domain as a mature method for measuring ultra-low-noise microwave signals [227]. This technique compares the signal against two references and correlates them to suppress the independent noise from the references. Similar techniques have been introduced in the optical domain to characterize sub-Hertz linewidth lasers with optical references [228].

¹Work presented in this chapter has been published in [223] “Correlated self-heterodyne method for ultra-low-noise laser linewidth measurements.” *Optics Express* 30.14 (2022), pp. 25147–25161.

In this paper, we demonstrate a reference-free self-heterodyne cross-correlator for ultra-low-noise laser linewidth measurements. By employing two PDs for OE conversion in the conventional self-heterodyne method, the cross-correlation can eliminate the need for references while extracting laser noise. In addition, balanced photodetectors (BPDs) are used to minimize the RIN coupling ratio. The cross-correlator has a noise floor lower than $0.01 \text{ Hz}^2/\text{Hz}$ and 40.4 dBrad^2 RIN suppression at 1 MHz offset frequency. Various commercial and lab-built lasers are used to benchmark the measurements, including an external-cavity laser (ECL) and a distributed-feedback (DFB) laser with and without self injection locking. Factors that may impact cross-correlator performance, including environmental noise coupling and delay length selection, are also discussed. The measurement can be readily generalized to other wavelengths [229] and may advance the development of next-generation laser sources through rapid measurement of noise.

8.2 Measurement setup

The COSH setup is shown in Fig. 8.1(a). A laser under test is split by a three-port acousto-optic modulator (AOM) into frequency-downshifted (1st order output) and unshifted (0th order output) portions. The former is polarization-controlled and then recombined with the latter delayed by a 1-km-long fiber, which forms a modified Mach–Zehnder interferometer (MZI) with a free spectral range (FSR) of 214.06 kHz. The three-port AOM acts as a variable splitter that also uses the unshifted laser power compared to a two-port modulator. On the output side, instead of one PD, both outputs are divided and received by two identical balanced photodetectors (BPDs). Using BPDs helps suppress RIN and using two BPDs allows cross-correlation between the electrical outputs and suppresses independent BPD noise. The whole optical section of the system is isolated from the external environment with an acoustic shield. The BPD outputs are recorded using a high-speed oscilloscope. The AOM is driven with a 55 MHz radio-frequency carrier which determines the center frequency of the recorded waveforms [Fig. 8.1(b)], and the sampling rate of the oscilloscope is set to 250 MHz to prevent aliasing. AC coupling at the oscilloscope is used to block low-frequency components that are spectrally far away from the carrier. The time delay between the two channels is estimated to be less than 0.5 ns and will not be considered in the following analyses. 2 seconds of waveforms (500×10^6 points for each channel, 1×10^9 points in total) are collected and transferred to a computer for data processing. While the record length is limited by the memory of our oscilloscope, it is sufficient to meet the noise

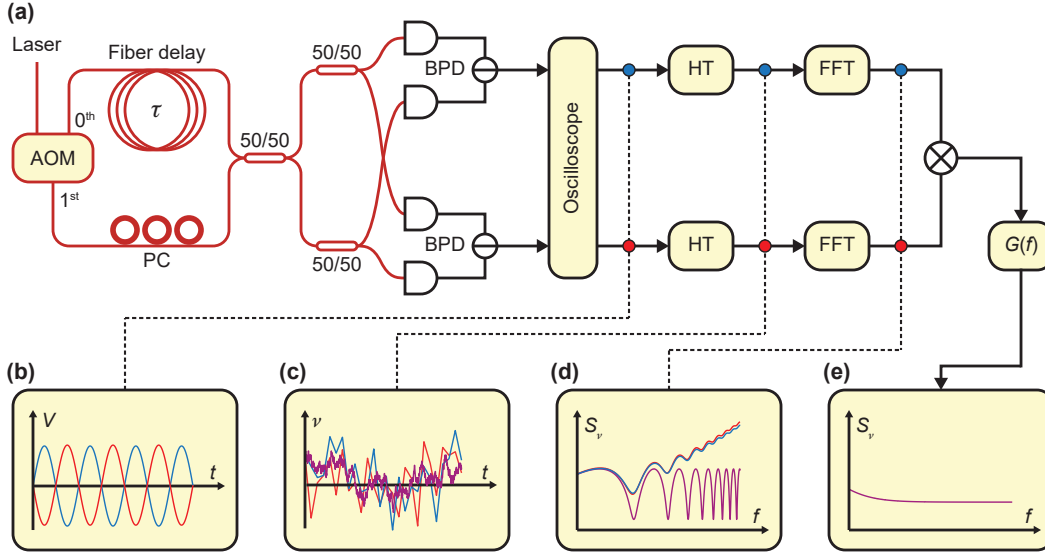


Figure 8.1: **Schematic of the correlated self-heterodyne (COSH) measurement setup.** (a) Illustration of the setup. AOM, acousto-optic modulator; PC, polarization controller; BPD, balanced photodetector; HT, Hilbert transform, followed by a time-domain difference operation; FFT, fast Fourier transform. (b) Self-heterodyne waveforms recorded by a high-speed oscilloscope. (c) Frequency fluctuations extracted with Hilbert transform and time-domain difference. The red and blue lines refer to the frequency fluctuations from two BPD outputs marked by color in accordance with inset (a) (similar hereinafter). Laser frequency noise (common mode) indicated by the purple line and BPD-induced noise (differential mode) are contained in the extracted results. (d) Power spectral density (PSD) of BPD output frequency given by FFT. The red and blue lines refer to the total noise PSD while the purple line indicates the laser frequency noise PSD (common mode). The deviation between them at high frequency is due to the BPD noise. (e) Single-sideband (SSB) laser noise after cross-correlation and $G(f)$ in which the BPD noise has been eliminated.

floor requirements for the current measurements (see section 8.4).

In the data processing part, phase fluctuations for each channel are extracted using Hilbert transforms and then converted to frequency fluctuation through time-domain difference [Fig. 8.1(c)]. The Hilbert transform causes distortions at the endpoints of the waveforms, thus the first and last 40 ms (10×10^6 points) for each channel are discarded after the Hilbert transform. The remaining points are divided into non-overlapping segments (rectangular windowing, similar to Bartlett's method for estimating power spectra [230]), each with a τ_R time length [corresponding to a resolution bandwidth (RBW) of $1/\tau_R$] and fast-Fourier-transformed to obtain the frequency spectrum at a given offset frequency. For lower frequency offsets, the

RBWs are made smaller with the segment lengths adjusted accordingly. The power spectrum density (PSD) of BPD output frequencies suffer from BPD noise [Fig. 8.1(d)]. To suppress this noise, the cross-correlation is calculated as the product between the Fourier coefficients of the two BPD output frequency spectra, averaged over all available segments. Owing to the independent nature of the two BPD noise sources, BPD noise can be suppressed compared to individual PSDs of BPD outputs. Finally, the cross-correlation spectrum is multiplied by a processing gain $G(f)$ to compensate the filtering effect from the MZI and recover the single-sideband (SSB) laser frequency noise result [Fig. 8.1(e)].

8.3 Modeling of the measurement process

In this section, we model the properties of the output signal from the COSH measurements. In the following, all spectral densities refer to two-sided spectral densities unless indicated otherwise.

Self-heterodyne noise detection

To model the self-heterodyne method for noise measurement, we begin with an idealized derivation, where a frequency-shifted signal beats against a delayed signal and the resulting frequency noise is calculated. From the Wiener-Khinchin theorem, the frequency noise of the original signal can be understood as the Fourier transform of the phase time-derivative correlation function:

$$S_v(f) = \int_{-\infty}^{\infty} \left\langle \frac{\dot{\phi}(0)}{2\pi} \frac{\dot{\phi}(t)}{2\pi} \right\rangle e^{2\pi i f t} dt = \frac{1}{4\pi^2} \int_{-\infty}^{\infty} \langle \dot{\phi}(0) \dot{\phi}(t) \rangle e^{2\pi i f t} dt. \quad (8.1)$$

Here $S_v(f)$ is the frequency noise PSD of the input signal, f is the offset frequency, ϕ is the optical noisy phase signal, t denotes time, dot indicates derivative with respect to t and $\langle z \rangle$ denotes the ensemble average of z .

The self-heterodyne beating outputs a signal with phase $-2\pi f_c t + \phi(t) - \phi(t - \tau)$, where τ is the delay time and f_c is the carrier frequency (determined by the AOM). We are thus interested in the frequency noise of $\nu(\tau) = -f_c + [\dot{\phi}(t) - \dot{\phi}(t - \tau)]/(2\pi)$. By the time-shifting property of the Fourier transform we get:

$$S_{\nu(\tau)}(f) = [2 - \exp(2\pi i f \tau) - \exp(-2\pi i f \tau)] S_v(f) = 4 \sin^2(\pi f \tau) S_v(f), \quad (8.2)$$

thus the frequency noise reads:

$$S_{\nu(\tau)}(f) = 4 \sin^2(\pi f \tau) S_v(f). \quad (8.3)$$

The transfer function in the above equations has zeros at integer multiples of MZI FSR ($f = 1/\tau, 2/\tau, 3/\tau$ and so on). At these offset frequencies, destructive interference eliminates the phase difference at the MZI output. To compensate, the processing gain $G(f)$ should be chosen as:

$$G(f) = \frac{1}{4 \sin^2(\pi f \tau)}. \quad (8.4)$$

We note that $G(f)$ diverges at integer multiples of the MZI FSR. This nonphysical divergence will be removed after the finite detection resolution bandwidth is properly considered (see discussion in section 8.3).

It is sometimes convenient to directly measure the phase noise corresponding to $S_{v(\tau)}(f)$, denoted as $S_{\varphi, v(\tau)}(f) \equiv S_{v(\tau)}(f)/f^2$ (e.g., by sending the RF signal directly to a phase noise analyzer). In this case,

$$S_{\varphi, v(\tau)}(f) = 4 \frac{\sin^2(\pi f \tau)}{f^2} S_v(f) = (2\pi\tau)^2 \text{sinc}^2(f\tau) S_v(f), \quad (8.5)$$

where $\text{sinc } z \equiv \sin(\pi z)/(\pi z)$ is the normalized sinc function.

Self-heterodyne noise detection using an AOM

Here we present a more rigorous derivation based on the setup described previously. Various non-ideal effects can be incorporated and compared against the experiments.

We assume a laser input signal of the form:

$$A(t) = \exp(-2\pi i f_0 t) [1 + \delta a(t)] \exp[-i\delta\phi(t)], \quad (8.6)$$

where f_0 is the optical frequency. The δa and $\delta\phi$ are relative amplitude fluctuation and phase fluctuation, respectively, and are assumed to be small within the time scale of $1/f_c$, where $\delta\phi = \phi - 2\pi f_0 t$. This indicates that the laser would have low noise, which is the intended regime for the cross-correlator. Discussions on using the setup to measure a high-noise laser can be found below in section 8.4.

The frequency-shifted signal becomes:

$$A_1(t) = \frac{1}{\sqrt{2}} \exp(-2\pi i f_0 t) \exp(2\pi i f_c t) [1 + \delta a(t)] \exp[-i\delta\phi(t)], \quad (8.7)$$

and the delayed signal becomes:

$$A_2(t) = \frac{1}{\sqrt{2}} \exp(-2\pi i f_0 t) \exp(2\pi i f_0 \tau) [1 + \delta a(t - \tau)] \exp[-i\delta\phi(t - \tau)], \quad (8.8)$$

where we have assumed that the AOM splits the light equally into two ports (which can be realized by adjusting the RF power input for the AOM).

The signals from the two arms are mixed at another coupler and form the MZI outputs. We do not assume *a priori* that the coupler is perfectly balanced and write the two output amplitudes as:

$$A_+ = q_1 A_1 + i q_2 A_2, \quad A_- = q_1^* A_2 + i q_2^* A_1, \quad (8.9)$$

where q_1 and q_2 are complex transmission coefficients. We further assume that the two couplers just before the BPDs are matched, such that the relative power between the two arms remains the same at the two BPDs. In this case, powers at individual PDs can be found from $P_{\pm} \equiv |A_{\pm}|^2$, and the RF power of each BPD output reads, up to a proportional constant,

$$\Delta P \equiv P_+ - P_- = 2\text{Re}[i q_1^* q_2 \exp(2\pi i f_0 \tau) \exp(-2\pi i f_c t) (1 + \Sigma a) \exp(i \Delta \phi)] + \Delta |q|^2 \Delta a, \quad (8.10)$$

where we have introduced some shorthand notations: $\Sigma a \equiv \delta a(t) + \delta a(t - \tau)$, $\Delta \phi \equiv \delta \phi(t) - \delta \phi(t - \tau)$, $\Delta a \equiv \delta a(t) - \delta a(t - \tau)$, and $\Delta |q|^2 \equiv |q_1|^2 - |q_2|^2$.

Next, the Hilbert transform is performed on ΔP to recover the analytic signal and extract the instantaneous phase. The terms within the brackets consist of the main part of ΔP and is itself an analytic signal oscillating at f_c . The Δa term may also influence the phase of the signal. However, only those frequency components of Δa around the carrier frequency f_c contribute to the phase noise at low offset frequencies. As the self-heterodyne beating shifts the phase noise information to f_c where the amplitude noise of a laser is extremely low, this effectively isolates the laser RIN from entering the phase extraction process. We can therefore approximate the analytic signal by

$$\mathcal{H}\Delta P \approx 2i q_1^* q_2 \exp(2\pi i f_0 \tau) \exp(-2\pi i f_c t) (1 + \Sigma a) \exp(i \Delta \phi), \quad (8.11)$$

and the phase can be extracted as:

$$\varphi = \Delta \phi - 2\pi f_c t + 2\pi f_0 \tau + \text{Arg}[i q_1^* q_2]. \quad (8.12)$$

After that, $\nu(\tau)$ is calculated from the time derivative of ϕ , which can be approximated with a finite time difference:

$$\nu(\tau) = \frac{\dot{\varphi}}{2\pi} = -f_c + \frac{\delta \dot{\phi}(t) - \delta \dot{\phi}(t - \tau)}{2\pi}. \quad (8.13)$$

From here, the spectral density of $\nu(\tau)$ measured by a single BPD can be estimated and then used to recover $S_\nu(f)$ with the processing gain from Eq. (8.4). The results with cross-correlation can be further found in section 8.3.

Resolution bandwidth

To compute $S_{\nu}(\tau)$ using the Wiener-Khinchin theorem, an infinite length of $\nu(\tau)$ would be required to complete the Fourier transform accurately. Using a limited amount of data leads to a finite resolution bandwidth, which will distort the measured frequency noise. Segmenting the data into shorter sections has a similar effect. Below we derive the modified PSD estimate and the corresponding $G(f)$ for the finite resolution bandwidth case.

In the calculation, $S_{\nu}(\tau)$ is estimated from the Fourier coefficients of the gated signal:

$$S_{\nu(\tau),\text{gated}}(f) = \frac{|\hat{\nu}_{\text{gated}}(\tau, f)|^2}{\int_{-\infty}^{\infty} w(\tau')^2 d\tau'}, \quad (8.14)$$

where $w(\tau')$ is the window function for gating and $\hat{\nu}_{\text{gated}}(\tau, f)$ is the Fourier coefficient of the gated signal:

$$\hat{\nu}_{\text{gated}}(\tau, f) = \int_{-\infty}^{\infty} \nu(\tau, t = \tau') w(\tau') \exp(2\pi i f \tau') d\tau'. \quad (8.15)$$

Viewing $\nu(\tau)$ as random variables, the expectation of $S_{\nu(\tau),\text{gated}}$ reads

$$\begin{aligned} E[S_{\nu(\tau),\text{gated}}(f)] &= \frac{\int_{-\infty}^{\infty} \int_{-\infty}^{\infty} E[\nu(\tau, t = \tau') \nu(\tau, t = \tau' + \tau'')] w(\tau') w(\tau' + \tau'') e^{2\pi i f \tau''} d\tau' d\tau''}{\int_{-\infty}^{\infty} w(\tau')^2 d\tau'} \\ &= \frac{\int_{-\infty}^{\infty} d\tau'' \langle \nu(\tau, 0) \nu(\tau, \tau'') \rangle e^{2\pi i f \tau''} \int_{-\infty}^{\infty} d\tau' w(\tau') w(\tau' + \tau'')}{\int_{-\infty}^{\infty} w(\tau')^2 d\tau'} \end{aligned} \quad (8.16)$$

$$\begin{aligned} &= \int_{-\infty}^{\infty} d\tau'' \langle \nu(\tau, 0) \nu(\tau, \tau'') \rangle e^{2\pi i f \tau''} w_2(\tau'') \\ &= \int_{-\infty}^{\infty} S_{\nu(\tau)}(f - f') \hat{w}_2(f') df', \end{aligned} \quad (8.17)$$

where we introduced $w_2(\tau'')$ as the normalized autocorrelation of w and its associated Fourier transform $\hat{w}_2(f')$:

$$w_2(\tau'') = \frac{\int_{-\infty}^{\infty} w(\tau') w(\tau' + \tau'') d\tau'}{\int_{-\infty}^{\infty} w(\tau')^2 d\tau'}, \quad w_2(0) = 1 \quad (8.18)$$

$$\hat{w}_2(f') = \int_{-\infty}^{\infty} w_2(\tau'') \exp(2\pi i f' \tau'') d\tau''. \quad (8.19)$$

From Eq. (8.17), it can be seen that the effect of gating the signal results in convolving $S_{\nu(\tau)}$ with \hat{w}_2 , which is equivalent to filtering the frequency domain trace of $S_{\nu(\tau)}$ with a response function of w_2 in the time domain from the viewpoint of Eq. (8.16).

To see how this filtering of $S_{\nu(\tau)}$ impacts signal processing, we rewrite Eq. (8.3) as:

$$S_{\nu(\tau)}(f) = 4 \sin^2(\pi f \tau) S_{\nu}(f) = [2 - 2 \cos(2\pi f \tau)] S_{\nu}(f). \quad (8.20)$$

If $S_{\nu}(f)$ varies slowly within the MZI FSR scale ($1/\tau$), the gating filter only affects the term within the brackets. For the rectangular window used here, w_2 becomes a triangular window, and $S_{\nu(\tau),\text{gated}}$ can be found as:

$$S_{\nu(\tau),\text{gated}}(f) \approx [2 - 2(1 - \tau\text{RBW})^+ \cos(2\pi f \tau)] S_{\nu}(f), \quad (8.21)$$

where $z^+ = \max(0, z)$ is the ramp function and RBW is the resolution bandwidth of the rectangular window (equal to the reciprocal of its temporal width). The associated processing gain becomes:

$$G_{\text{gated}}(f) = \frac{1}{2 - 2(1 - \tau\text{RBW})^+ \cos(2\pi f \tau)}. \quad (8.22)$$

We note that the divergence of $G(f)$ is no longer present in Eq. (8.22) for any finite RBW, which can be explained as a spectral leakage of noise from other offset frequencies to integer multiples of MZI FSR. If the RBW is larger than one MZI FSR such that $\tau\text{RBW} > 1$, then Eq. (8.21) and Eq. (8.22) indicate that the fringe pattern is completely averaged out by the filtering. In this case the systems work in the same way as an incoherent detection setup.

Suppression of independent noise with cross-correlation

While the optical signals are converted to RF signal at the BPDs, technical BPD noise (usually characterized by its noise equivalent power) will also be present in the output and is dominant in the current measurement system. This increases the phase noise of the output and limits the noise floor of the measurement without cross-correlation. We model this technical noise by adding noise terms, $\varphi_{\text{BPD},1}$ and $\varphi_{\text{BPD},2}$, for the extracted phase:

$$\varphi_1 = \varphi + \varphi_{\text{BPD},1}, \quad \varphi_2 = \varphi + \varphi_{\text{BPD},2}. \quad (8.23)$$

The noise will be transferred to the frequency signal:

$$\nu_1(\tau) = \nu(\tau) + \nu_{\text{BPD},1}, \quad \nu_2(\tau) = \nu(\tau) + \nu_{\text{BPD},2}, \quad (8.24)$$

where $\nu_{\text{BPD},1}$ and $\nu_{\text{BPD},2}$ are the noise terms after time-domain difference. In this case, calculating the Fourier coefficient of $\nu(\tau)$ leads to:

$$\hat{\nu}_1(\tau, f) = \int_{-\infty}^{\infty} [\nu(\tau, t = \tau') + \nu_{\text{BPD},1}] w(\tau') \exp(2\pi i f \tau') d\tau'. \quad (8.25)$$

Assuming $v(\tau)$ and $v_{\text{BPD},1}$ are independent, the calculated PSD for $v_1(\tau)$ becomes:

$$S_{v(\tau),1}(f) = S_{v(\tau),\text{gated}}(f) + S_{\text{BPD},1}, \quad (8.26)$$

where $S_{\text{BPD},1}$ is the gated PSD for $v_{\text{BPD},1}$ noise and determines the measurement floor using only a single BPD.

To remove the BPD technical noise, both BPD outputs are used and cross-correlated to suppress the contribution of $v_{\text{BPD},1}$ and $v_{\text{BPD},2}$. The correlated estimate of $S_{v(\tau)}(f)$ is the product of two Fourier coefficients originating from different BPDs:

$$S_{v(\tau),\text{corr}}(f) = \frac{\hat{v}_1(\tau, f)\hat{v}_2^*(\tau, f)}{\int_{-\infty}^{\infty} w(\tau')^2 d\tau'}. \quad (8.27)$$

Assuming $v(\tau)$, $v_{\text{BPD},1}$ and $v_{\text{BPD},2}$ are all independent, it can be readily shown that:

$$E[S_{v(\tau),\text{corr}}(f)] = S_{v(\tau),\text{gated}}(f), \quad (8.28)$$

and includes only the contributions from laser noise. However, BPD noise adds randomness to the correlation and increases the variance of $S_{v(\tau),\text{corr}}(f)$. This effect will be more obvious at high offset frequencies when technical phase noise from the BPD is converted to larger frequency noise (see section 8.4), or at low offset frequencies while using a short delay line (where $G(f) \gg 1$). This can be improved by averaging over N segments of data, which lowers the standard error of the mean by \sqrt{N} times and therefore improves the signal-to-noise ratio by \sqrt{N} .

8.4 Characterization of the measurement setup

RIN suppression

As noted in section 8.3, the frequency-shifting process of the self-heterodyne setup effectively isolates RIN from coupling into the measured frequency noise. In order to characterize the RIN suppression performance of the cross-correlator, we measured the RIN conversion ratio with a setup shown in Fig. 8.2(a). The measurement setup consists of an ECL (RIO ORION 1550 nm laser module) modulated by an AOM to generate an artificial RIN signal. The AOM carrier generated from the arbitrary waveform generator is amplitude-modulated by a single-tone sine wave with manually configured frequency and modulation depth. The carrier frequency is selected as the optimal modulation frequency of this AOM (here 55 MHz) to minimize amplitude-phase coupling during the modulation process. By measuring the frequency noise with and without the power modulation using the cross-correlator, the RIN conversion ratio can be determined. The modulation intensity is calculated

from the modulation depth and calibrated by tapping 10% of the modulated laser before the cross-correlator. All signals are recorded by the aforementioned high-speed oscilloscope.

Empirically, the RIN conversion to measured frequency noise can be described by:

$$\tilde{S}_{v(\tau)}(f) = S_{v(\tau),\text{corr}}(f) + f^2\alpha \times \text{RIN}(f), \quad (8.29)$$

where $\tilde{S}_{v(\tau)}(f)$ is the measured frequency noise just before the processing gain, including RIN contributions, α is a proportionally constant that converts RIN to phase noise, and the extra f^2 factor further converts phase noise to frequency noise. For the reconstructed laser noise the above equation becomes:

$$\tilde{S}_v(f) = S_v(f) + G(f)f^2\alpha \times \text{RIN}(f). \quad (8.30)$$

The single-tone modulations used in the actual measurements could not be quantified by a spectral density. Instead, the frequency noise intensity can be recovered from:

$$P_v(f_{\text{AM}}) = S_v(f_{\text{AM}}) \times \text{RBW}, (f_{\text{AM}}) \quad (8.31)$$

where f_{AM} is the modulation frequency. Similarly, phase noise intensity is related to the frequency noise intensity by:

$$P_\phi(f_{\text{AM}}) = \frac{1}{f_{\text{AM}}^2} P_v(f_{\text{AM}}). \quad (8.32)$$

By comparing $P_\phi(f_{\text{AM}})$ against the amplitude modulation intensity, α can be extracted through a linear fitting process.

The measured $\tilde{S}_v(f)$ under different modulation intensity at 963 kHz offset frequency are shown in Fig. 8.2(b). The noise spurs at 29 kHz come from the ECL itself, which also appear in Fig. 8.5 and Fig. 8.6. The inset of Fig. 8.2(b) shows the linear fitting between the phase noise intensity and the modulation intensity. Here, the RIN to measured laser phase noise conversion ratio [$G(f)\alpha$] at 963 kHz (i.e., the slope of the fitting) is -46.4 dBrad² (2.29×10^{-5} rad²). From here, α can be found as -40.4 dBrad² (9.16×10^{-5} rad²).

As shown in Fig. 8.2(c), a -20 dBc modulation intensity is selected for all measurements at different modulation frequencies, which is sufficient as an overestimation for RIN of a normal laser. The intrinsic laser frequency noise may obscure the presence of weakly-coupled RIN, and becomes a noise floor for the RIN conversion measurement. The frequency noise intensity without laser power modulation

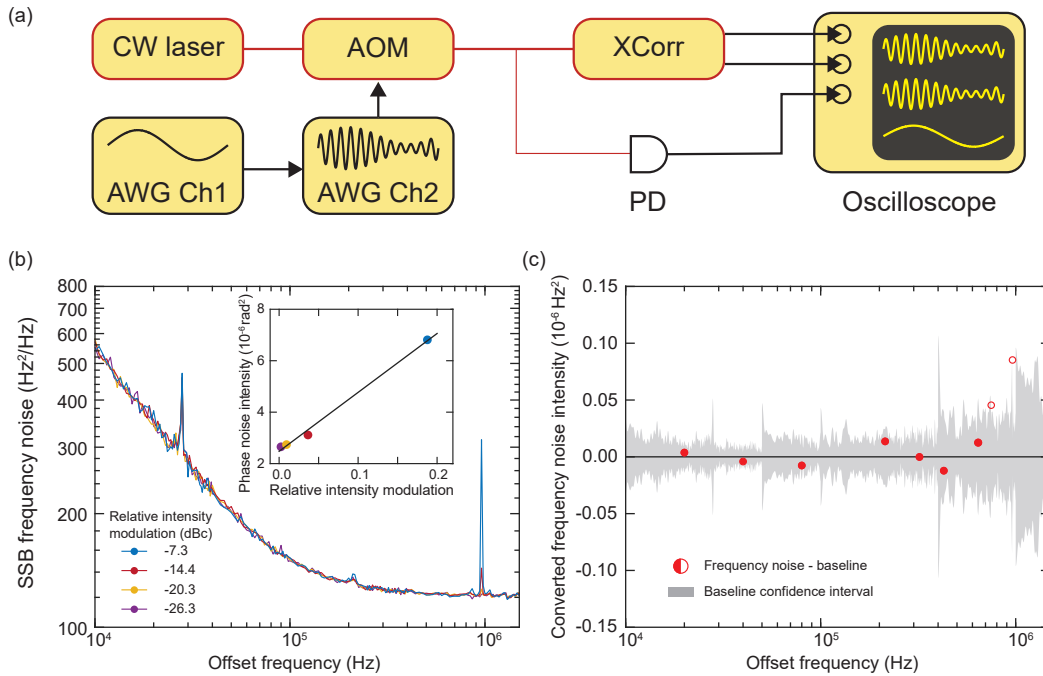


Figure 8.2: Characterization on RIN suppression. (a) Experimental setup for RIN suppression characterization. CW laser: continuous wave laser, AOM: acousto-optical modulator, XCorr: cross-correlator [as in Fig. 8.1(a)], AWG: arbitrary waveform generator, PD: photodetector, OSC: oscilloscope. (b) SSB laser frequency noise spectra under different modulation intensity at 963 kHz offset frequency. Inset: Phase noise intensity at 963 kHz as a function of modulation intensity. The solid black line is the linear fitting. (c) Frequency dependence of RIN conversion ratio. The shaded area stands for the confidence interval (99% confidence probability) of the frequency noise intensity without power modulation. The frequency noise intensity baseline has been subtracted for comparison. The red circles are plotted as the converted frequency noise intensity (measured frequency noise intensity minus baseline) at different offset frequency corresponding to the power modulation frequency. The solid (hollow) circles indicate that the converted frequency noise intensity is inside (outside) the shaded area.

(i.e., the baseline) is measured 10 times and a 99% possibility confidence interval (shaded area) for the RIN conversion signal is given by assuming that the measured frequency noise intensity is normally distributed. When amplitude modulation is applied, the frequency noise intensity (red circles) at the corresponding offset frequency is calculated and compared with the baseline. A measured intensity outside the confidence interval indicates significant conversion of RIN. RIN conversion has been tested at 20 kHz, 40 kHz, 80 kHz, 214 kHz (equal to the MZI FSR $1/\tau_0$, where $\tau_0 = 4.67$ ms is the delay time of the 1-km-long fiber), 321 kHz, 428 kHz, 642

kHz, 749 kHz, and 963 kHz. The modulation frequencies over 100 kHz match the integer and half-integer multiples of MZI FSR, corresponding to local maximums and minimums of $G(f)$, respectively. The measured frequency noises with artificial RIN coupling only fall outside of the confidence interval at 749 kHz and 963 kHz, which suggests that the RIN suppression is high enough for lasers at offset frequency lower than 1 MHz. We note that the $G(f)$ will amplify the RIN conversion at offset frequencies equal to integer multiples of the MZI FSR. However, as shown by the experimental data, the overall RIN conversion is not important in most cases.

Below we present a model for the origin of RIN coupling by considering signal leakage at the AOM within the cross-correlator [Fig. 8.1(a)]. We assume that a small portion of 0th order light is leaked into the 1st order port at the AOM, which is supported by experimental observations. The net effect is that the amplitude for the frequency-shifted arm should be modified as:

$$\begin{aligned} \tilde{A}_1(t) = & \frac{1}{\sqrt{2}} \exp(-2\pi i f_0 t) \exp(2\pi i f_c t) [1 + \delta a(t)] \exp[-i\delta\phi(t)] \\ & + \frac{\epsilon}{\sqrt{2}} \exp(-2\pi i f_0 t) [1 + \delta a(t)] \exp[-i\delta\phi(t)], \end{aligned} \quad (8.33)$$

where ϵ is a complex number that represents the leakage amplitude. The amplitude on the other arm A_2 remains the same. The BPD power now reads, keeping only the signals oscillating near frequency f_c ,

$$\begin{aligned} \Delta\tilde{P} = & 2\text{Re}[iq_1^* q_2 \exp(2\pi i f_0 \tau) \exp(-2\pi i f_c t) (1 + \Sigma a) \exp(i\Delta\phi)] \\ & + \text{Re}[\Delta|q|^2 \epsilon \exp(-2\pi i f_c t) (1 + 2\delta a(t))], \end{aligned} \quad (8.34)$$

where the exponential of phase noise is linearized for convenience. The extra term results from the same-arm beating detected at the BPD. The analytic signal is given by, up to first order of ϵ and $\Delta\phi$,

$$\mathcal{H}\Delta P \approx 2iq_1^* q_2 \exp(2\pi i f_0 \tau) \exp(-2\pi i f_c t) \left[1 + \Sigma a + i\Delta\phi + \frac{\Delta|q|^2|\epsilon|}{|q_1 q_2|} \exp(i\theta_{\text{RIN}}) \left(\frac{1}{2} + \delta a(t) \right) \right]. \quad (8.35)$$

Here θ_{RIN} is a phase angle that couples amplitude to phase:

$$\theta_{\text{RIN}} = 2\pi i f_0 \tau + \text{Arg}[\epsilon] - \text{Arg}[iq_1^* q_2]. \quad (8.36)$$

Performing phase extraction and time difference leads to

$$\tilde{v}(\tau) = v(\tau) + \frac{\Delta|q|^2|\epsilon|}{|q_1 q_2|} \sin(\theta_{\text{RIN}}) \frac{d\delta a}{2\pi dt}. \quad (8.37)$$

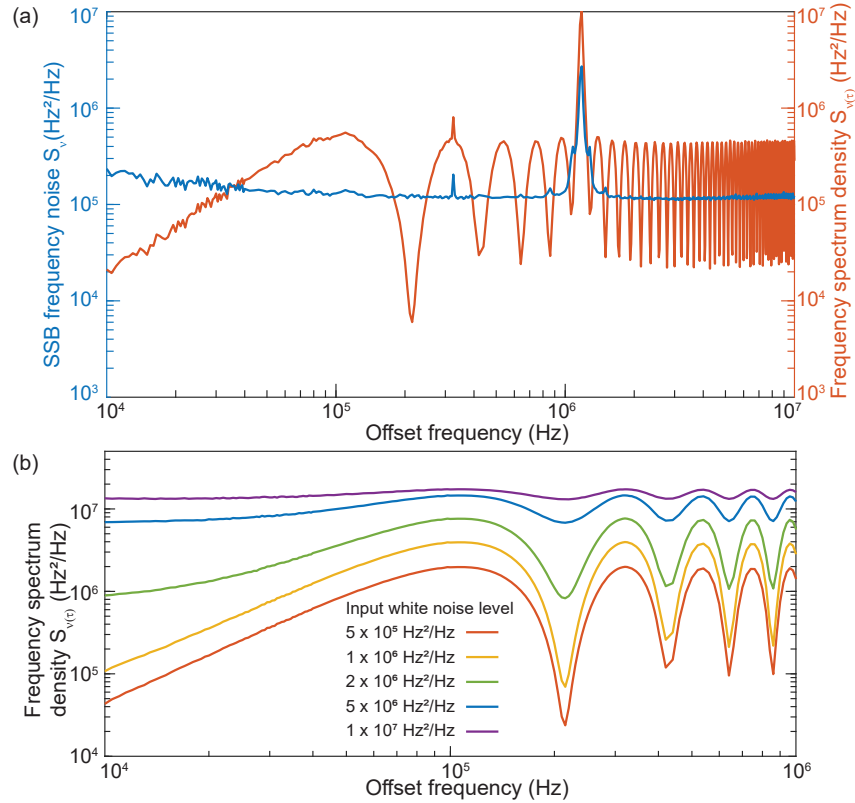


Figure 8.3: **Measurement dynamic range (lasers with high frequency noise).** (a) SSB frequency noise and frequency spectral density of a DFB laser. (b) Simulated $S_{v(\tau)}(f)$ output of the system when a laser with high white frequency noise is used as input. The white noise levels are, from bottom to top: 5×10^5 Hz²/Hz, 1×10^6 Hz²/Hz, 2×10^6 Hz²/Hz, 5×10^6 Hz²/Hz, 1×10^7 Hz²/Hz.

For the worst case (maximal coupling) $\sin(\theta_{\text{RIN}}) = \pm 1$, and in the case when laser amplitude and frequency noise are independent, calculating the PSD gives:

$$\tilde{S}_{v(\tau)}(f) = S_{v(\tau),\text{corr}}(f) + f^2 \frac{(\Delta|q|^2)^2 |\epsilon|^2 \text{RIN}(f)}{|q_1|^2 |q_2|^2} \frac{1}{4}. \quad (8.38)$$

Comparing with the empirical model Eq. (8.29) gives:

$$\alpha = \frac{(\Delta|q|^2)^2}{4|q_1|^2 |q_2|^2} |\epsilon|^2, \quad (8.39)$$

and is directly proportional to the leaked power at the AOM.

Dynamic range

To quantify the upper limit of noise the COSH setup can measure, we use a DFB laser for characterization. Limited by the laser cavity length and reflectivity of the

output facet, the noise of a DFB laser can reach the level of 1 MHz, corresponding to a coherence length shorter than the 1-km-long fiber delay line. However, the measurable noise is not directly related by the delay line, but only limited by the carrier frequency (see below).

Measurement results for a free-running DFB laser are shown in Fig. 8.3(a). The SSB frequency noise of the DFB laser is around $1.2 \times 10^5 \text{ Hz}^2/\text{Hz}$ at high offset frequencies, corresponding to a 0.75 MHz Lorentzian linewidth and a 267 m coherence length in fiber (assuming a fiber refractive index of 1.5). As the BPD noise is far less than the DFB laser noise, performing cross-correlation on the data provides negligible improvement. Note that the noise peak at 1.2 MHz is from the DFB laser. Combined with the estimate for the noise floor (see section 8.4), the setup could reach over 70 dB dynamic range for frequency noise measurements.

To understand how the system behaves for higher laser frequency noise, simulations have been performed and the results are collected in Fig. 8.3(b). Increasing the laser frequency noise above $1 \times 10^6 \text{ Hz}^2/\text{Hz}$ leads to a visible decrease of fringe contrast before multiplying $G(f)$. This can be attributed to the wide broadening of the carrier signal $\exp(2\pi i f_c t)$. The components that are separated more than f_c from the carrier cross into the negative-frequency domain and will be reflected by the Hilbert transform. If such contributions are significant, Eq. (8.11) is invalidated, and the laser frequency noise can no longer be reliably recovered. Choosing an AOM with higher modulation frequency and increasing the sampling rate for the oscilloscope could increase the upper noise limit at the expense of measurement time or memory. We note that fringes are still visible even if the noise level exceeds the MZI FSR (i.e., the laser coherent length is shorter than the delay length), unless the resolution bandwidth is chosen to exceed the MZI FSR [as given by $G(f)$].

Noise floor

Finally, the noise floor of the COSH method is verified using a DFB injection locked to a high-Q resonator (section 2.3). The laser linewidth coming from the compound laser-resonator system can be greatly suppressed [231, 232, 74] and have demonstrated record linewidth levels in integrated photonics platforms comparable to fiber lasers [233].

Here, the aforementioned DFB laser has been self-injection-locked to a 7-m long, ultra-high-Q on-chip resonator (with an intrinsic Q factor of 150 million). The SSB frequency noise of this lab-built laser is then measured by the setup and results are

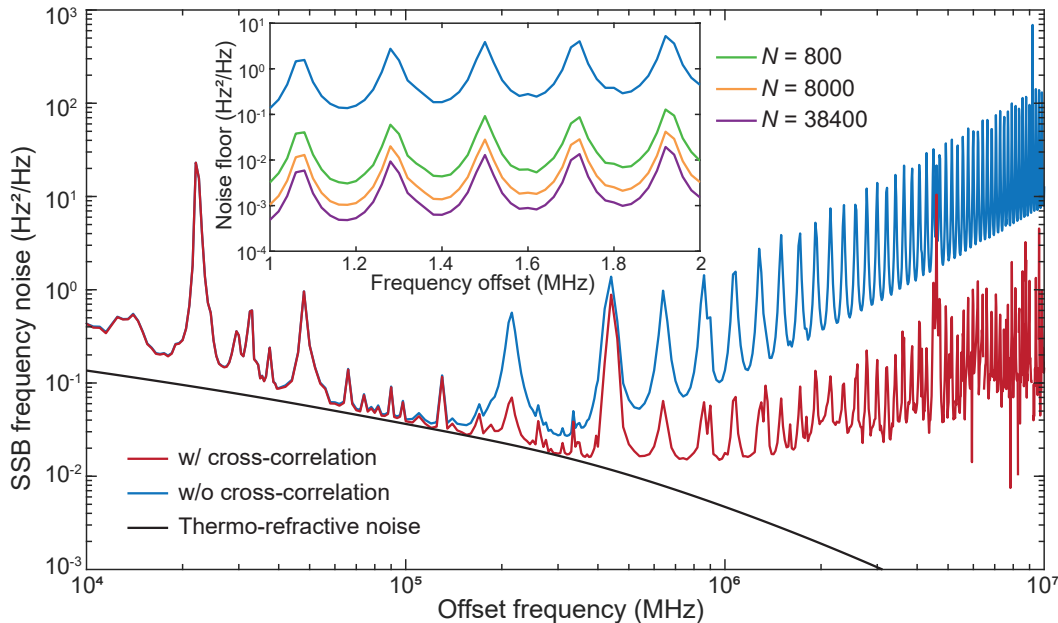


Figure 8.4: **Measurement noise floor (DFB laser with SIL).** Two traces are measured by the self-heterodyne method with and without cross-correlation. The deviation between them is due to the BPD noise as illustrated in Fig. 8.1. The cross-correlator extracts the common mode SIL laser noise and suppresses the individual BPD noise to reach a $0.01 \text{ Hz}^2/\text{Hz}$ noise floor at 1 MHz offset frequency. The simulated thermo-refractive noise is plotted in black for comparison. Inset: the measured frequency noise error bar is interpreted as the measurement system noise floor here. With increasing averaging segment number N , the noise floor is reduced by \sqrt{N} . The blue trace is the same as the main figure.

shown in Fig. 8.4. Compared with a 1.4-m long spiral resonator [233], larger mode volume further suppresses the thermo-refractive noise (TRN) and reaches $0.041 \text{ Hz}^2/\text{Hz}$ at 100 kHz offset frequency. The numerically simulated TRN is also plotted for comparison. The lowest measured frequency noise is $0.015 \pm 0.002 \text{ Hz}^2/\text{Hz}$ at 1 MHz offset frequency, comparable with the previous work [233].

The power spectrum density given by a single BPD output frequency without cross-correlation is also illustrated in Fig. 8.1(d). Since BPD technical noise is approximately white when characterized as phase noise, the independent BPD noise contribution to measured frequency noise scales as f^2 and is more apparent at high offset frequencies, which is confirmed by comparing the two traces in Fig. 8.4. The spurs in the single-BPD trace are the BPD technical noise amplified by $G(f)$ and are also an indication that the BPD noise has significant contributions. By using cross-correlation and averaging over N segments of data, the noise contribution can

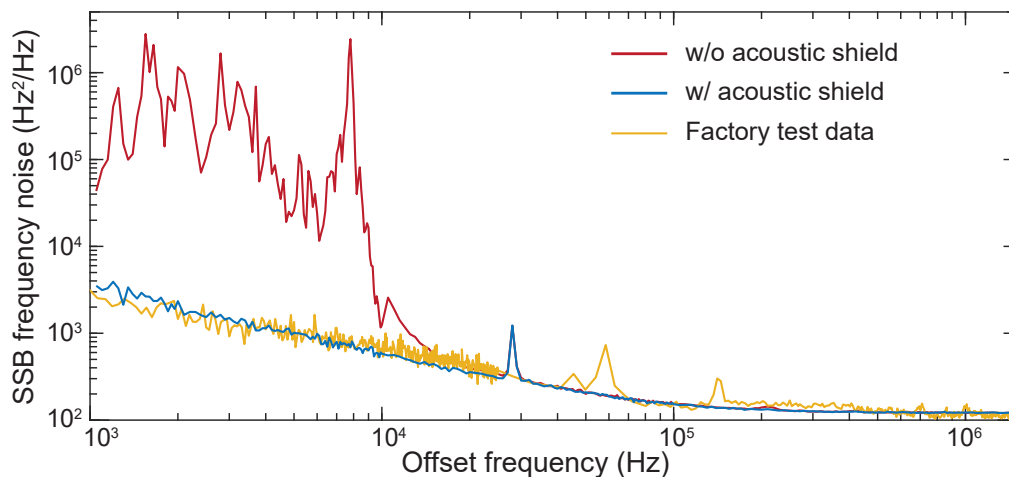


Figure 8.5: **Frequency noise measurement with and without acoustic shield.** Typical SSB frequency noise of a commercial ECL obtained using cross-correlator with/without an acoustic shield. The yellow trace is the test data as provided by the manufacturer.

be reduced by \sqrt{N} . Here, for the 20 kHz resolution bandwidth used for high offset frequencies, we have $N = 38400$, and the signal-to-noise ratio is improved by 22.9 dB. As shown in the inset of Fig. 8.4, the error bar of measured frequency noise (standard deviation of frequency noise from multiple segments) is interpreted as the measurement setup noise floor here, and larger N (proportional to the overall data length used) leads to a lower noise floor. Assuming 0.05 mW optical input power at the BPD, the technical noise is equivalent to 0.10 Hz²/Hz at 1 MHz offset frequency, consistent with the blue trace in Fig. 8.4 inset. With $N = 38400$, the noise floor with cross-correlation is suppressed to be 0.0005 Hz²/Hz, consistent with the purple trace in the inset. At MZI FSR frequencies, the noise floor is enhanced but remains below 0.01 Hz²/Hz around 1 MHz offset frequency. The spurs of measured SSB frequency noise at higher than 1 MHz offset frequency is significantly higher than the noise floor and are believed to originate from the residual RIN amplified by $G(f)$.

8.5 Discussion

Environmental noise coupling

Acoustic noise may be present in the external environment and can couple to the measured SSB frequency noise through the fiber delay of the modified MZI. To minimize environmental perturbations, the optical section of the measurement setup is acoustically shielded with a foam box. To calibrate the external noise isolation

from the shield box, we have applied additional acoustic noise in the environment and measured the ECL frequency noise. As is shown in Fig. 8.5, the measured SSB frequency noise is smooth and no peaks can be found below 10 kHz offset frequency, compared to the case without the acoustic shield. Above 10 kHz, the effect of environment noise is not evident for the noise measurement system. Meanwhile, the frequency noise measured with acoustic shield is consistent with the laser manufacturers specification sheet.

Fiber delay length

A major drawback of the current setup is the decrease of sensitivity at integer multiples of MZI FSR, where the frequency noise destructively interferes and $G(f)$ reaches its maximum. These frequencies can be adjusted by changing the fiber delay length. If the destructive interference is undesired over a wide offset frequency range, the fiber delay length should be short enough such that the first MZI FSR appears outside the frequency range. For example, a 10 meter fiber (with MZI FSR equal to approximately 20 MHz) ensures that no fringes appear below 20 MHz offset frequency.

A major disadvantage of using a short fiber delay length is the large systematic error

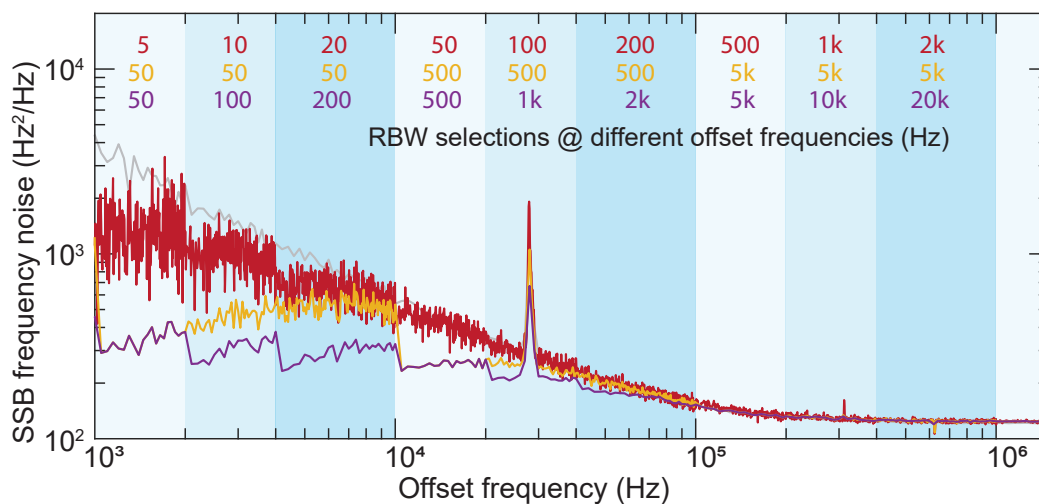


Figure 8.6: **Frequency noise measurement with a short delay line.** SSB frequency noise of the ECL calculated with different RBW configurations using 15-meter-long fiber delay line are plotted as red, yellow and purple traces. The RBWs chosen at different offset frequency intervals (marked by shading) are shown at the top with colors in accordance with traces. The gray line using 1-km-long fiber delay line is plotted as a reference and its RBW configurations are the same as the purple trace.

of low-frequency noise. To demonstrate this, the 1 km delay line in the MZI is substituted with a 15 meter fiber and the ECL noise is measured. The results are presented in Fig. 8.6. We note that there are frequency noise discontinuities when the RBW changes. For the purple trace in Fig. 8.6, the calculated frequency noise “jumps” at 20 kHz, 40 kHz and 100 kHz, where different RBWs are chosen for the offset frequency intervals on both sides. On the other hand, the data measured using 1 km delay length (grey trace) gives a continuous result and is consistent with the noise data from the laser manufacturers specification sheet.

The strong dependence of calculated noise on the RBW can be attributed to the non-white frequency noise spectrum of the laser. The gating filter acts differently on the spectrum compared to the white case and invalidates Eq. (8.21). By using smaller RBWs, the calculated noise becomes closer to the true laser noise, as seen from the red trace in Fig. 8.6.

8.6 Conclusion

In this paper we have demonstrated a correlated self-heterodyne (COSH) method to measure laser frequency noise with $0.01 \text{ Hz}^2/\text{Hz}$ noise floor and high RIN rejection quantified by the coupling coefficient $\alpha = -40.4 \text{ dBrad}^2$. Commercial ECL and DFB lasers with/without self-injection-locking are used to verify the performance. The cross-correlation noise floor is limited by the coupled RIN amplified by the processing gain $G(f)$ as well as residual BPD technical noise.

The setup described here can be further reconfigured to meet specific measurement requirements. For example, the RIN suppression can be further enhanced by using an AOM with higher 0th order to 1st order isolation. Temperature controllers can be installed to the 50/50 couplers to adjust the coupling ratio precisely and balance the MZI arms. On the other hand, if the expected laser noise frequency is high, then cross-correlation is not necessary and the memory depth of the oscilloscope can be decreased accordingly. A conventional PD can be used in place of a BPD if RIN is not a concern. Overall, the specific measurement setup and parameters introduced in Section 2.1 are targeted towards ultra-low-noise laser measurement mainly at high offset frequencies, while the basic principle remains universal.

HIGH-COHERENCE HYBRID-INTEGRATED 780 NM SOURCE BY SELF-INJECTION-LOCKED SECOND-HARMONIC GENERATION IN A HIGH-Q SILICON-NITRIDE RESONATOR

9.1 Introduction

¹ Highly coherent visible laser sources play a crucial role in the operation of optical atomic clocks [235], automotive LiDAR [236], and sensing systems [237]. However, existing bench-top visible lasers are both costly and bulky, limiting their use beyond laboratory environments including application in future navigation and sensing systems. Integration of these sources on a semiconductor chip is a necessary step if the systems that use these devices are to be made compact, portable and low power.

To address this challenge, we generate visible light in a high- Q silicon nitride microcavity that is hybridly-integrated to a semiconductor laser operating in the near-infrared band. The cavity both line narrows the laser through self-injection-locking (SIL) [66, 233] and generates the high-coherence visible signal as a second-harmonic (SH) signal by way of the photogalvanic field-induced second-order nonlinearity [238] and the all-optical-poling effect [239, 240, 241] in Si_3N_4 . A record-low frequency noise floor of $4 \text{ Hz}^2/\text{Hz}$ is achieved for the 780 nm emission. Frequency noise is reduced by 100-fold compared with previous integrated visible lasers [242, 243, 244, 245]. The approach can potentially generate signals over a wide range of visible and near-visible bands, and thereby help transition many table-top systems into a fieldable form.

9.2 Characterization on the second-harmonic generation

The resonator is fabricated using the ultra-low-loss silicon-nitride photonic platform [66, 67] with a 100 nm thick silicon nitride waveguide core and a $2.2 \mu\text{m}$ thick silica top cladding. The resonator has a $5 \mu\text{m}$ waveguide width and a $850 \mu\text{m}$ radius. The free-spectral range is 35.52 GHz at 1560 nm. Two pulley couplers are designed for coupling at both the near-infrared and visible bands. The near-infrared coupler has a $2.3 \mu\text{m}$ waveguide width with a $3.5 \mu\text{m}$ gap that is designed to prevent coupling

¹Work presented in this chapter has been published in [234] “High-coherence hybrid-integrated 780 nm source by self-injection-locked second-harmonic generation in a high- Q silicon-nitride resonator.” *Optica* 10.9 (2023), pp. 1241–1244.

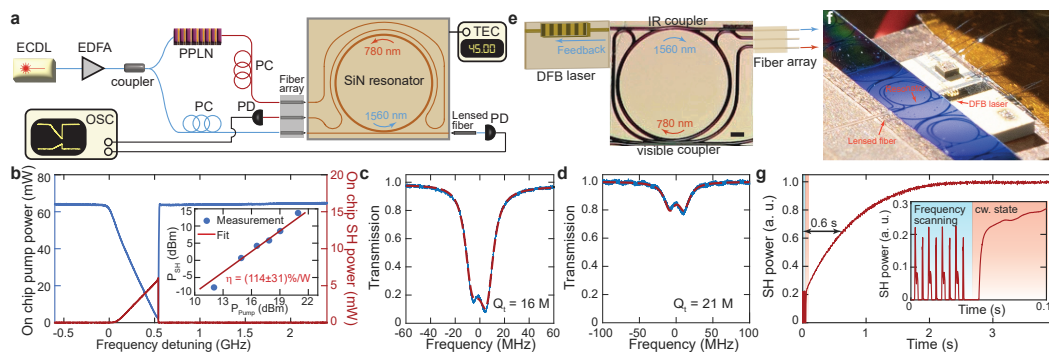


Figure 9.1: Experimental setups and characterization of the Si_3N_4 resonator and SH generation performance. (a) Experimental setup used to determine the phase matching condition and characterize the SH performance of the Si_3N_4 resonator. ECDL, external cavity diode lasers; EDFA, Erbium-doped fiber amplifier; PPLN, periodically poled lithium niobate; PC, polarization controller; PD, photodiode; OSC, oscilloscope; TEC, thermoelectric cooler. (b) Measured on-chip transmission pump power (left axis) and generated SH power (right axis) when scanning the frequency of the pump laser across a cavity resonance at the phase matching condition. Inset: measured on-chip SH power (blue dots) plotted versus pump power levels. (c) Transmission spectrum of the pump resonance at 1560.1 nm. (d) Transmission spectrum of the SH resonance at 780.05 nm. (e) Schematic of the hybrid-integrated frequency conversion laser, where a DFB laser is endfire-coupled to a high-Q silicon-nitride microresonator to provide feedback to the laser. The upper and lower waveguides are designed for coupling at 1560 nm and 780 nm, respectively. The scale bar is $200 \mu\text{m}$. (f) Photograph of the hybrid-integrated frequency conversion laser in panel (e). (g) The time response of the SH power after the DFB laser frequency is stopped at the operation point. Inset: zoom-in of the main plot.

to the visible mode. The visible coupler has a $1.6 \mu\text{m}$ waveguide width with a $0.3 \mu\text{m}$ gap that is designed to reduce coupling to the near-infrared mode.

The resonator is first characterized using the experimental setup shown in Fig. 9.1(a). A 4-channel fiber array and a lensed fiber are used to couple to near-infrared and visible resonances simultaneously. To probe the resonances, the output of a near-infrared tunable laser is split with one output doubled in frequency using a periodically-poled lithium niobate (PPLN) crystal. In this way, first and second harmonic probe waves are generated to characterize resonator spectra in these bands. Because the photogalvanic effect induces optical poling to thereby establish the quasi-phase-matching condition [241], a visible mode having twice the pumping frequency will achieve SH generation regardless of its propagation constant. To establish this condition, the Si_3N_4 chip is temperature controlled to tune the mode spectra. Tuning over no more

than one free-spectral-range is sufficient, and in the current setup a chip temperature of 45 °C aligns the pump resonance at 1560.1 nm with a visible resonance at 780.05 nm. Photogalvanic-induced second-harmonic generation can be readily observed when scanning the pump laser across the near-infrared resonance, as shown in Fig. 9.1(b). Continuous-wave SH power measurements with the pump laser frequency fixed at the cavity resonance are shown in the inset of Fig. 9.1(b).

The frequency conversion efficiency is fit by the red line with a slope of 2. Within our measurement range, the SHG efficiency (η in %/W) is found to be constant and estimated to be $114 \pm 31\%$ W (average over measured powers). The SH output power as high as 24 mW is measured (in the bus waveguide). The total Q factors (Q_t) of the pump and SH modes are determined by transmission spectra measurements shown in Fig. 9.1(c,d). The experimental measurements are plotted in blue and the theoretical fittings are plotted in red. Each resonance exhibits backscatter-induced splitting and total Q factors (Q_t) are indicated. The leakage of 1560 nm light into the 780 nm pulley coupler and the multimode nature of the 780 nm waveguide make determination of the intrinsic (i.e., ring-only) Q factors of the 1560 nm and 780 nm modes difficult (see section 9.4).

To achieve a high coherence visible light source in a compact foot print, we replace the bulk tunable laser with a distributed-feedback (DFB) chip laser as shown in the experimental setup in Fig. 9.1(e,f). The DFB laser is endfire-coupled to the silicon-nitride chip and can deliver 20 mW pump power to the resonator waveguide (accounting for 6 dB facet coupling loss). Backscatter-induced feedback from the resonator to the laser provides self-injection-locking that dramatically reduces the laser frequency noise [66, 233]. Upon current tuning the DFB laser frequency into the 1560.1 nm resonance, the optical poling process is initialized through the field-induced photogalvanic effect. This process can be monitored by scanning the frequency of the DFB laser around the resonance by modulating the pump current with a function generator. The produced SH signal power changes periodically during forward and backward scanning (the blue region in the inset of Fig. 9.1(g)). The function generator is then turned off, and the DFB frequency self-locks into the resonance center and SH power builds to steady state. The resulting SH signal time evolution is shown over short time interval in the inset of Fig. 9.1(g) (red region) and over several seconds in the main panel. The SH power build-up features a 0.6s rise time and takes only a few seconds to reach steady state. In steady-state operation, the SH power at 780 nm reaches over 0.5 mW on-chip as monitored via

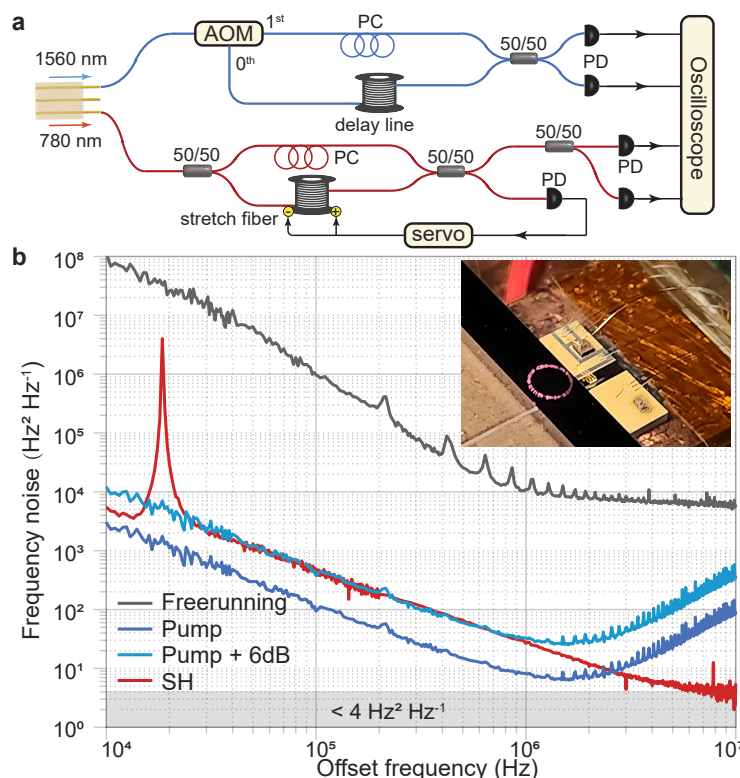


Figure 9.2: **Frequency noise measurement for SIL pump laser and generated SH laser.** (a) Frequency noise measurement setups for both the SIL 1560 nm laser and the SH 780 nm laser. AOM, acousto-optic modulator. (b) Measured single-sideband frequency noise spectrum. Gray, blue and red traces show the frequency noise spectra of the free-running DFB signal, SIL pump signal (1560 nm), and SH signal (780 nm), respectively. The light blue trace shows the SIL pump laser frequency noise up-shifted by 6 dB. The inset is a photograph of the device under operation with 780 nm emission visible on the ring resonator.

a lensed fiber (12dB coupling loss).

9.3 Frequency noise characterization on the generated SIL 780 nm source

The SIL 1560 nm light and SH generated 780 nm light are then further analyzed to determine their frequency noise performance, as shown in Fig. 9.2(a). The SH signal is sent to a delayed self-homodyne detection setup with quadrature-point locking [37] and its measured frequency noise is shown as the red trace in Fig. 9.2(b). The peak at 18 kHz offset in the spectrum is due to the feedback loop response of a fiber stretcher used to maintain the quadrature point. At high offset frequencies, the photodetector (PD) white noise is suppressed using a cross-correlation technique [227, 223], and achieves $4 \text{ Hz}^2/\text{Hz}$ noise floor above 6 MHz offset frequency, corresponding to a record-low 25 Hz instantaneous linewidth for

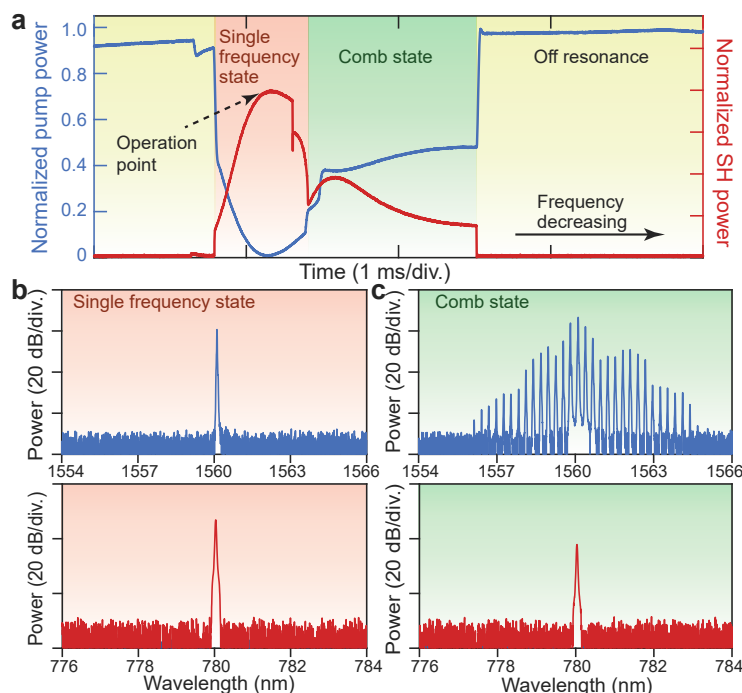


Figure 9.3: **Self-injection locked laser response with pump current induced frequency tuning.** (a) The measured SIL pump power (blue) and second harmonic power (red) when the pump current is scanned across the resonance. When the DFB laser frequency is tuned into the cavity resonance, the near infrared laser is initially in a single frequency state and eventually tunes to a comb state. (b, c) Upper panels: Measured optical spectra of the near infrared laser in the single frequency state (b) and comb state (c). Lower panels: corresponding SH 780 nm spectra.

visible on-chip sources. The frequency noise of the self-injection locked pump laser is characterized with a self-heterodyne approach [223], and the result is shown as the blue curve in Fig. 9.2. Compared with the free-running DFB laser noise (gray trace), the SIL process suppresses the noise by 40 (32) dB at 100 kHz (1 MHz) offset frequency. The generated SH laser noise is 4 times higher than the SIL pump laser noise due to coherent photon conversion [244]. Specifically, the phase fluctuation of the pump field is doubled in the SH signal through the squaring of the pumping field. The corresponding SH spectral density function therefore experiences a factor of 4 increase (6 dB) relative to the pump. The difference in these spectra at high offset frequencies is due to spontaneous emission noise in the 1560 nm signal resulting from its measurement at the transmission port of the coupled resonator system.

High intra-cavity photon density and resonant backscattering make this system prone to Kerr frequency comb generation [66]. SIL comb formation is governed by

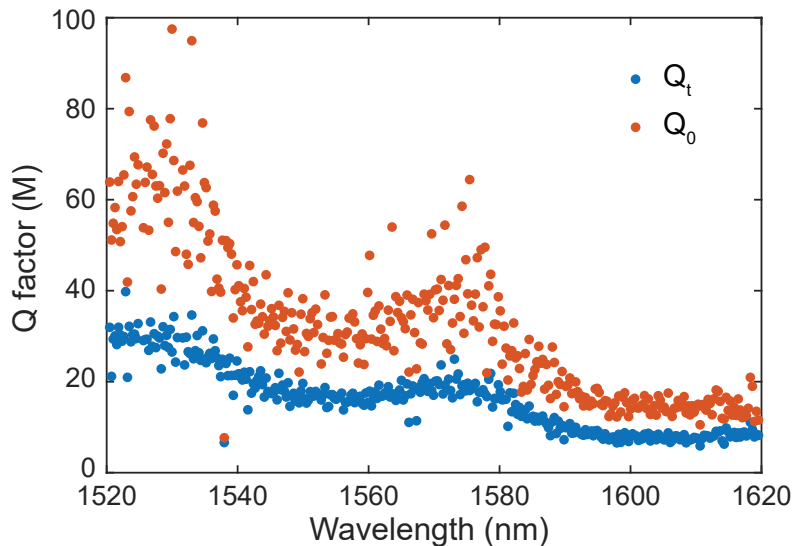


Figure 9.4: **Resonator total and intrinsic Q factor measurements plotted versus wavelength.** The spectral peaks in measured intrinsic Q factors are believed to originate from the wavelength-dependent coupling of 1560 nm light to the 780 nm pulley coupler.

feedback phase and frequency detuning [73, 246], and these parameters also provide a way to favor single mode lasing over comb generation. In the present device the laser-to-chip gap (feedback phase) and pump current (frequency detuning) provide useful controls. The latter is illustrated in Fig. 9.3(a) where the transmitted pumping power and the SH power are plotted versus DFB laser current scan. Distinct regimes where the single-frequency SIL state and the comb state appear are indicated. In the comb state, only the pump comb line can be frequency doubled due to phase matching condition. The operation point used in the previous power and noise measurements is indicated. Typical SH spectra in the two regimes are shown in Fig. 9.3(b, c). Reduced SH power is apparent for the comb state since intracavity pump power is reduced by comb formation.

9.4 Coupler design principle

The 1560 nm pulley coupler waveguide width is chosen to achieve phase matching to the ring resonator fundamental eigenmode. The coupler occupies an effective arc length of about 0.1 radian of the resonator with a $3.5 \mu\text{m}$ minimum gap. This gap is too large to achieve significant interaction with the 780 nm eigenmode thereby reduces parasitic coupling of the 780 nm mode to the 1560 nm coupler.

The $1.6 \mu\text{m}$ width of the 780 nm pulley coupler waveguide is approximately phase-

matched to the TE₁₀ higher-order mode of the resonator. This substantially phase mismatches the coupler to the fundamental resonator eigenmode at 1560 nm, thereby suppressing parasitic coupling of the 1560 nm mode. The coupler gap is narrow (minimum 0.3 μm) and to further minimize perturbation to the 1560 nm mode, the gap is adiabatically reduced using the arc of an archimedean spiral. This however results in a coupler arc-length exceeding 1 radian, so that 780 nm optical power might undergo several coupling oscillations over the length of the coupler.

Some parasitic coupling of the 1560 nm light to the 780 nm coupler is expected. This parasitic loss channel contributes to the intrinsic Q factor of the resonator at 1560 nm. And spectral measurements of Q factor around 1560 nm reveal an oscillatory dependence (see Fig. 9.4) that is believed to result from this dependence.

9.5 Conclusion

In conclusion, we have demonstrated a record-low 4 Hz^2/Hz frequency noise floor for a hybrid-integrated visible light source by self-injection-locking a DFB laser with a high- Q Si_3N_4 resonator. The III-V laser and the silicon nitride resonator can be heterogeneously integrated using the integration technique described in ref. [247]. The current resonator intrinsic Q factor is not optimal, and based on prior work could exceed 250M at 1560 nm [66]. This should further reduce frequency noise levels since the SIL noise reduction scales as Q^2 [74]. This scaling makes generation of highly coherent signals easier in the near-IR where optical Q factors are overall much higher. The SH-SIL process therefore extends this advantage into the visible bands. Finally, the photogalvanic effect makes access to other wavelengths straightforward. Devices require only waveguide couplers designed for efficient visible and near infrared operation.

BIBLIOGRAPHY

- [1] Kerry J. Vahala. “Optical microcavities.” In: *Nature* 424.6950 (2003), pp. 839–846.
- [2] Jason McKeever et al. “Experimental realization of a one-atom laser in the regime of strong coupling.” In: *Nature* 425.6955 (2003), pp. 268–271.
- [3] Takao Aoki et al. “Observation of strong coupling between one atom and a monolithic microresonator.” In: *Nature* 443.7112 (2006), pp. 671–674.
- [4] Hossein Rokhsari et al. “Radiation-pressure-driven micro-mechanical oscillator.” In: *Optics Express* 13.14 (2005), pp. 5293–5301.
- [5] Tobias J. Kippenberg and Kerry J. Vahala. “Cavity optomechanics: Back-action at the mesoscale.” In: *Science* 321.5893 (2008), pp. 1172–1176.
- [6] Frank Vollmer and Lan Yang. “Review Label-free detection with high-Q microcavities: A review of biosensing mechanisms for integrated devices.” In: *Nanophotonics* 1.3-4 (2012), pp. 267–291.
- [7] Eli Yablonovitch. “Inhibited spontaneous emission in solid-state physics and electronics.” In: *Physical Review Letters* 58.20 (1987), p. 2059.
- [8] Robert W. Boyd, Alexander L. Gaeta, and Enno Giese. “Nonlinear optics.” In: *Springer Handbook of Atomic, Molecular, and Optical Physics*. Springer, 2008, pp. 1097–1110.
- [9] Scott A. Diddams, Kerry Vahala, and Thomas Udem. “Optical frequency combs: Coherently uniting the electromagnetic spectrum.” In: *Science* 369.6501 (2020), eaay3676.
- [10] Joerg Reichert et al. “Measuring the frequency of light with mode-locked lasers.” In: *Optics Communications* 172.1-6 (1999), pp. 59–68.
- [11] David J. Jones et al. “Carrier-envelope phase control of femtosecond mode-locked lasers and direct optical frequency synthesis.” In: *Science* 288.5466 (2000), pp. 635–639.
- [12] Scott A. Diddams et al. “Direct link between microwave and optical frequencies with a 300 THz femtosecond laser comb.” In: *Physical Review Letters* 84.22 (2000), p. 5102.
- [13] Scott A. Diddams et al. “An optical clock based on a single trapped $^{199}\text{Hg}^+$ ion.” In: *Science* 293.5531 (2001), pp. 825–828.
- [14] Jun Ye, Long Sheng Ma, and John L. Hall. “Molecular iodine clock.” In: *Physical Review Letters* 87.27 (2001), p. 270801.
- [15] Tara M. Fortier et al. “Generation of ultrastable microwaves via optical frequency division.” In: *Nature Photonics* 5.7 (2011), pp. 425–429.

- [16] Ian Coddington et al. “Rapid and precise absolute distance measurements at long range.” In: *Nature Photonics* 3.6 (2009), pp. 351–356.
- [17] R. Holzwarth et al. “Optical frequency synthesizer for precision spectroscopy.” In: *Physical Review Letters* 85.11 (2000), p. 2264.
- [18] Tilo Steinmetz et al. “Laser frequency combs for astronomical observations.” In: *Science* 321.5894 (2008), pp. 1335–1337.
- [19] Tobias J. Kippenberg et al. “Dissipative Kerr solitons in optical microresonators.” In: *Science* 361.6402 (2018), eaan8083.
- [20] Tobias Herr et al. “Temporal solitons in optical microresonators.” In: *Nature Photonics* 8.2 (2014), pp. 145–152.
- [21] B.J.M. Hausmann et al. “Diamond nonlinear photonics.” In: *Nature Photonics* 8.5 (2014), pp. 369–374.
- [22] Chaitanya Joshi et al. “Thermally controlled comb generation and soliton modelocking in microresonators.” In: *Optics Letters* 41.11 (2016), pp. 2565–2568.
- [23] Pei-Hsun Wang et al. “Intracavity characterization of micro-comb generation in the single-soliton regime.” In: *Optics Express* 24.10 (2016), pp. 10890–10897.
- [24] Victor Brasch et al. “Photonic chip-based optical frequency comb using soliton Cherenkov radiation.” In: *Science* 351.6271 (2016), pp. 357–360.
- [25] Qing Li et al. “Stably accessing octave-spanning microresonator frequency combs in the soliton regime.” In: *Optica* 4.2 (2017), pp. 193–203.
- [26] Xu Yi et al. “Soliton frequency comb at microwave rates in a high-Q silica microresonator.” In: *Optica* 2.12 (2015), pp. 1078–1085.
- [27] Zheng Gong et al. “High-fidelity cavity soliton generation in crystalline AlN micro-ring resonators.” In: *Optics Letters* 43.18 (2018), pp. 4366–4369.
- [28] Lin Chang et al. “Ultra-efficient frequency comb generation in AlGaAs-on-insulator microresonators.” In: *Nature Communications* 11.1 (2020), p. 1331.
- [29] Yang He et al. “Self-starting bi-chromatic LiNbO₃ soliton microcomb.” In: *Optica* 6.9 (2019), pp. 1138–1144.
- [30] Marc Nikles, Luc Thevenaz, and Philippe A. Robert. “Brillouin gain spectrum characterization in single-mode optical fibers.” In: *Journal of Light-wave Technology* 15.10 (1997), pp. 1842–1851.
- [31] E.P. Ippen and R.H. Stolen. “Stimulated Brillouin scattering in optical fibers.” In: *Applied Physics Letters* 21.11 (1972), pp. 539–541.

- [32] Andrey Kobayakov, Michael Sauer, and Dipak Chowdhury. “Stimulated Brillouin scattering in optical fibers.” In: *Advances in Optics and Photonics* 2.1 (2010), pp. 1–59.
- [33] Benjamin J. Eggleton, Christopher G. Poulton, and Ravi Pant. “Inducing and harnessing stimulated Brillouin scattering in photonic integrated circuits.” In: *Advances in Optics and Photonics* 5.4 (2013), pp. 536–587.
- [34] Matthew Tomes and Tal Carmon. “Photonic micro-electromechanical systems vibrating at X-band (11-GHz) rates.” In: *Physical Review Letters* 102.11 (2009), p. 113601.
- [35] Ivan S. Grudinin, Andrey B. Matsko, and Lute Maleki. “Brillouin lasing with a CaF₂ whispering gallery mode resonator.” In: *Physical Review Letters* 102.4 (2009), p. 043902.
- [36] Ravi Pant et al. “On-chip stimulated Brillouin scattering.” In: *Optics Express* 19.9 (2011), pp. 8285–8290.
- [37] Hansuek Lee et al. “Chemically etched ultrahigh-Q wedge-resonator on a silicon chip.” In: *Nature Photonics* 6.6 (2012), p. 369.
- [38] William Loh et al. “Dual-microcavity narrow-linewidth Brillouin laser.” In: *Optica* 2.3 (2015), pp. 225–232.
- [39] Nils T. Otterstrom et al. “A silicon Brillouin laser.” In: *Science* 360.6393 (2018), pp. 1113–1116.
- [40] K. Y. Yang et al. “Bridging ultrahigh-Q devices and photonic circuits.” In: *Nat. Photon.* 12 (2018), pp. 297–302.
- [41] Sarat Gundavarapu et al. “Sub-hertz fundamental linewidth photonic integrated Brillouin laser.” In: *Nature Photonics* 13.1 (2019), pp. 60–67.
- [42] Jiang Li et al. “Characterization of a high coherence, Brillouin microcavity laser on silicon.” In: *Optics Express* 20.18 (2012), pp. 20170–20180.
- [43] Jiang Li, Hansuek Lee, and Kerry J. Vahala. “Low-noise Brillouin laser on a chip at 1064 nm.” In: *Optics Letters* 39.2 (Jan. 2014), pp. 287–290.
- [44] Jiang Li, Hansuek Lee, and Kerry J. Vahala. “Microwave synthesizer using an on-chip Brillouin oscillator.” In: *Nature Communications* 4.1 (2013), p. 2097.
- [45] Jiang Li et al. “Electro-optical frequency division and stable microwave synthesis.” In: *Science* 345.6194 (2014), pp. 309–313.
- [46] Jiang Li, Myoung-Gyun Suh, and Kerry Vahala. “Microresonator Brillouin gyroscope.” In: *Optica* 4.3 (2017), pp. 346–348.
- [47] Yu-Hung Lai et al. “Earth rotation measured by a chip-scale ring laser gyroscope.” In: *Nature Photonics* (2020).

- [48] William Loh et al. “Operation of an optical atomic clock with a Brillouin laser subsystem.” In: *Nature* 588 (2020), pp. 244–249.
- [49] P.A. Franken et al. “Generation of optical harmonics.” In: *Physical Review Letters* 7.4 (1961), p. 118.
- [50] Cheng Wang et al. “Second harmonic generation in nano-structured thin-film lithium niobate waveguides.” In: *Optics Express* 25.6 (2017), pp. 6963–6973.
- [51] Juanjuan Lu et al. “Periodically poled thin-film lithium niobate microring resonators with a second-harmonic generation efficiency of 250,000%/W.” In: *Optica* 6.12 (2019), pp. 1455–1460.
- [52] Aref Chowdhury et al. “Second-harmonic generation in periodically poled GaN.” In: *Applied Physics Letters* 83.6 (2003), pp. 1077–1079.
- [53] Y.R. Shen. “Optical second harmonic generation at interfaces.” In: *Annual Review of Physical Chemistry* 40.1 (1989), pp. 327–350.
- [54] S. Matsumoto et al. “Quasiphase-matched second harmonic generation of blue light in electrically periodically-poled lithium tantalate waveguides.” In: *Electronics Letters* 22.27 (1991), pp. 2040–2042.
- [55] Vladimir S. Ilchenko et al. “Nonlinear optics and crystalline whispering gallery mode cavities.” In: *Physical Review Letters* 92.4 (2004), p. 043903.
- [56] Josef U. Furst et al. “Second-harmonic generation of light at 245 nm in a lithium tetraborate whispering gallery resonator.” In: *Optics Letters* 40.9 (2015), pp. 1932–1935.
- [57] Lue Wu et al. “Greater than one billion Q factor for on-chip microresonators.” In: *Optics Letters* 45.18 (2020), pp. 5129–5131.
- [58] Myoung-Gyun Suh and Kerry Vahala. “Gigahertz-repetition-rate soliton microcombs.” In: *Optica* 5.1 (2018), pp. 65–66.
- [59] Yu-Hung Lai et al. “Observation of the exceptional-point-enhanced Sagnac effect.” In: *Nature* 576.7785 (2019), pp. 65–69. DOI: 10.1038/s41586-019-1777-z.
- [60] Tobias Herr et al. “Mode spectrum and temporal soliton formation in optical microresonators.” In: *Physical Review Letters* 113.12 (2014), p. 123901.
- [61] Seung Hoon Lee et al. “Towards visible soliton microcomb generation.” In: *Nature Communications* 8.1 (2017), p. 1295.
- [62] Ming Cai, Oskar Painter, and Kerry J. Vahala. “Observation of critical coupling in a fiber taper to a silica-microsphere whispering-gallery mode system.” In: *Physical Review Letters* 85.1 (2000), p. 74.
- [63] S.M. Spillane et al. “Ideality in a fiber-taper-coupled microresonator system for application to cavity quantum electrodynamics.” In: *Physical Review Letters* 91.4 (2003), p. 043902.

- [64] Yu-Hung Lai et al. “Fiber taper characterization by optical backscattering reflectometry.” In: *Optics Express* 25.19 (2017), pp. 22312–22327.
- [65] Myoung-Gyun Suh et al. “Directly pumped 10 GHz microcomb modules from low-power diode lasers.” In: *Optics Letters* 44.7 (2019), pp. 1841–1843.
- [66] Warren Jin et al. “Hertz-linewidth semiconductor lasers using CMOS-ready ultra-high-Q microresonators.” In: *Nature Photonics* 15.5 (2021), pp. 346–353.
- [67] M. Puckett and et al. “422 Million intrinsic quality factor planar integrated all-waveguide resonator with sub-MHz linewidth.” In: *Nature Communications* 12 (2021), p. 934.
- [68] Martin H.P. Pfeiffer et al. “Ultra-smooth silicon nitride waveguides based on the Damascene reflow process: Fabrication and loss origins.” In: *Optica* 5.7 (2018), pp. 884–892.
- [69] Kaikai Liu et al. “Ultralow 0.034 dB/m loss wafer-scale integrated photonics realizing 720 million Q and 380 μ W threshold Brillouin lasing.” In: *Optics Letters* 47.7 (2022), pp. 1855–1858.
- [70] Cyril Godey et al. “Stability analysis of the spatiotemporal Lugiato-Lefever model for Kerr optical frequency combs in the anomalous and normal dispersion regimes.” In: *Physical Review A* 89.6 (2014), p. 063814.
- [71] Xu Yi et al. “Active capture and stabilization of temporal solitons in microresonators.” In: *Optics Letters* 41.9 (2016), pp. 2037–2040.
- [72] Shuangyou Zhang et al. “Sub-milliwatt-level microresonator solitons with extended access range using an auxiliary laser.” In: *Optica* 6.2 (2019), pp. 206–212.
- [73] Boqiang Shen et al. “Integrated turnkey soliton microcombs.” In: *Nature* 582.7812 (2020), pp. 365–369.
- [74] N.M. Kondratiev et al. “Self-injection locking of a laser diode to a high-Q WGM microresonator.” In: *Optics Express* 25.23 (2017), pp. 28167–28178.
- [75] Chengying Bao et al. “Interleaved difference-frequency generation for microcomb spectral densification in the mid-infrared.” In: *Optica* 7.4 (2020), pp. 309–315. DOI: 10.1364/OPTICA.382992.
- [76] Chengying Bao et al. “Architecture for microcomb-based GHz-mid-infrared dual-comb spectroscopy.” In: *Nature Communications* 12.1 (2021), p. 6573. DOI: 10.1038/s41467-021-26958-6.
- [77] Fritz Keilmann, Christoph Gohle, and Ronald Holzwarth. “Time-domain mid-infrared frequency-comb spectrometer.” In: *Optics Letters* 29.13 (2004), pp. 1542–1544.

- [78] Ian Coddington, Nathan Newbury, and William Swann. “Dual-comb spectroscopy.” In: *Optica* 3.4 (2016), pp. 414–426.
- [79] Nathalie Picqué and Theodore W. Hänsch. “Frequency comb spectroscopy.” In: *Nature Photonics* 13.3 (2019), pp. 146–157.
- [80] Albert Schliesser, Nathalie Picqué, and Theodor W. Hänsch. “Mid-infrared frequency combs.” In: *Nature Photonics* 6.7 (2012), pp. 440–449.
- [81] Mengjie Yu et al. “Silicon-chip-based mid-infrared dual-comb spectroscopy.” In: *Nature Communications* 9.1 (2018), p. 1869.
- [82] F. Zhu et al. “Mid-infrared dual frequency comb spectroscopy based on fiber lasers for the detection of methane in ambient air.” In: *Laser Physics Letters* 12.9 (2015), p. 095701.
- [83] Zaijun Chen, Theodor W. Hänsch, and Nathalie Picqué. “Mid-infrared feed-forward dual-comb spectroscopy.” In: *Proceedings of the National Academy of Sciences* 116.9 (2019), pp. 3454–3459.
- [84] Gabriel Ycas et al. “High-coherence mid-infrared dual-comb spectroscopy spanning 2.6 to 5.2 μm .” In: *Nature Photonics* 12.4 (2018), p. 202.
- [85] Henry Timmers et al. “Molecular fingerprinting with bright, broadband infrared frequency combs.” In: *Optica* 5.6 (2018), pp. 727–732.
- [86] Zhaowei Zhang, Tom Gardiner, and Derryck T. Reid. “Mid-infrared dual-comb spectroscopy with an optical parametric oscillator.” In: *Optics Letters* 38.16 (2013), pp. 3148–3150.
- [87] A.V. Muraviev et al. “Massively parallel sensing of trace molecules and their isotopologues with broadband subharmonic mid-infrared frequency combs.” In: *Nature Photonics* 12.4 (2018), p. 209.
- [88] Hairun Guo et al. “Nanophotonic supercontinuum-based mid-infrared dual-comb spectroscopy.” In: *Optica* 7.9 (2020), pp. 1181–1188.
- [89] Nima Nader et al. “Infrared frequency comb generation and spectroscopy with suspended silicon nanophotonic waveguides.” In: *Optica* 6.10 (2019), pp. 1269–1276.
- [90] Alexander J. Lind et al. “Mid-infrared frequency comb generation and spectroscopy with few-cycle pulses and $\chi^{(2)}$ nonlinear optics.” In: *Physical Review Letters* 124.13 (2020), p. 133904.
- [91] Ming Yan et al. “Mid-infrared dual-comb spectroscopy with electro-optic modulators.” In: *Light: Science & Applications* 6.10 (2017), e17076.
- [92] Abijith S Kowligy et al. “Mid-infrared frequency combs at 10 GHz.” In: *Optics Letters* 45.13 (2020), pp. 3677–3680.
- [93] Cheng Wang et al. “Integrated lithium niobate electro-optic modulators operating at CMOS-compatible voltages.” In: *Nature* 562.7725 (2018), p. 101.

- [94] Amirhassan Shams-Ansari et al. “Thin-film lithium-niobate electro-optic platform for spectrally tailored dual-comb spectroscopy.” In: *Communications Physics* 5.1 (2022), p. 88.
- [95] Qi-Fan Yang et al. “Counter-propagating solitons in microresonators.” In: *Nature Photonics* 11.9 (2017), pp. 560–564.
- [96] Nazanin Hoghooghi, Ryan K. Cole, and Gregory B. Rieker. “11- μ s time-resolved, continuous dual-comb spectroscopy with spectrally filtered mode-locked frequency combs.” In: *Applied Physics B* 127.2 (2021), pp. 1–10.
- [97] Brad C. Smith, Bachana Lomsadze, and Steven T. Cundiff. “Optimum repetition rates for dual-comb spectroscopy.” In: *Optics Express* 26.9 (2018), pp. 12049–12056.
- [98] Myoung-Gyun Suh et al. “Microresonator soliton dual-comb spectroscopy.” In: *Science* 354.6312 (2016), pp. 600–603.
- [99] Avik Dutt et al. “On-chip dual-comb source for spectroscopy.” In: *Science Advances* 4.3 (2018), e1701858.
- [100] Chengying Bao, Myoung-Gyun Suh, and Kerry Vahala. “Microresonator soliton dual-comb imaging.” In: *Optica* 6.9 (2019), pp. 1110–1116.
- [101] Tong Lin et al. “Broadband ultrahigh-resolution chip-scale scanning soliton dual-comb spectroscopy.” In: *arXiv:2001.00869* (2020).
- [102] Kasper Van Gasse et al. “An on-chip III-V-semiconductor-on-silicon laser frequency comb for gas-phase molecular spectroscopy in real-time.” In: *arXiv:2006.15113* (2020).
- [103] Andreas Hugi et al. “Mid-infrared frequency comb based on a quantum cascade laser.” In: *Nature* 492.7428 (2012), p. 229.
- [104] Giacomo Scalari, Jérôme Faist, and Nathalie Picqué. “On-chip mid-infrared and THz frequency combs for spectroscopy.” In: *Applied Physics Letters* 114 (2019), p. 150401.
- [105] Victor Torres-Company and Andrew M. Weiner. “Optical frequency comb technology for ultra-broadband radio-frequency photonics.” In: *Laser & Photonics Reviews* 8.3 (2014), pp. 368–393.
- [106] Lukasz A. Sterczewski, Jonas Westberg, and Gerard Wysocki. “Computational coherent averaging for free-running dual-comb spectroscopy.” In: *Optics Express* 27.17 (2019), pp. 23875–23893.
- [107] Esther Baumann et al. “Spectroscopy of the methane ν_3 band with an accurate midinfrared coherent dual-comb spectrometer.” In: *Physical Review A* 84.6 (2011), p. 062513.
- [108] Iouli E. Gordon et al. “The HITRAN2016 molecular spectroscopic database.” In: *Journal of Quantitative Spectroscopy and Radiative Transfer* 203 (2017), pp. 3–69.

- [109] G.L. Villanueva, M.J. Mumma, and K. Magee-Sauer. “Ethane in planetary and cometary atmospheres: Transmittance and fluorescence models of the ν_7 band at $3.3 \mu\text{m}$.” In: *Journal of Geophysical Research: Planets* 116.E8 (2011).
- [110] Alexander J. Turner, Christian Frankenberg, and Eric A. Kort. “Interpreting contemporary trends in atmospheric methane.” In: *Proceedings of the National Academy of Sciences* 116.8 (2019), pp. 2805–2813.
- [111] Anthony D. Draper et al. “Broadband dual-frequency comb spectroscopy in a rapid compression machine.” In: *Optics Express* 27.8 (2019), pp. 10814–10825.
- [112] Erwan Lucas et al. “Spatial multiplexing of soliton microcombs.” In: *Nature Photonics* 12.11 (2018), pp. 699–705.
- [113] Birgitta Bernhardt et al. “Cavity-enhanced dual-comb spectroscopy.” In: *Nature Photonics* 4.1 (2010), pp. 55–57.
- [114] Marc Jankowski et al. “Ultrabroadband nonlinear optics in nanophotonic periodically poled lithium niobate waveguides.” In: *Optica* 7.1 (2020), pp. 40–46.
- [115] Zhiqian Yuan et al. “Soliton pulse pairs at multiple colors in normal dispersion microresonators.” In: *Nature Photonics* 610.11 (2023), pp. 977–983. doi: 10.1038/s41566-023-01257-2.
- [116] Xiaoxiao Xue et al. “Mode-locked dark pulse Kerr combs in normal-dispersion microresonators.” In: *Nature Photonics* 9.9 (2015), pp. 594–600.
- [117] Mohammad Soltani, Andrey Matsko, and Lute Maleki. “Enabling arbitrary wavelength frequency combs on chip.” In: *Laser & Photonics Reviews* 10.1 (2016), pp. 158–162.
- [118] Sangsik Kim et al. “Dispersion engineering and frequency comb generation in thin silicon nitride concentric microresonators.” In: *Nature Communications* 8.1 (2017), pp. 1–8.
- [119] Sven Ramelow et al. “Strong polarization mode coupling in microresonators.” In: *Optics Letters* 39.17 (2014), pp. 5134–5137.
- [120] Yu Li et al. “Spatial-mode-coupling-based dispersion engineering for integrated optical waveguide.” In: *Optics Express* 26.3 (2018), pp. 2807–2816.
- [121] Maxim Karpov et al. “Photonic chip-based soliton frequency combs covering the biological imaging window.” In: *Nature communications* 9.1 (2018), p. 1146.
- [122] Bok Young Kim et al. “Turn-key, high-efficiency Kerr comb source.” In: *Optics letters* 44.18 (2019), pp. 4475–4478.

- [123] Óskar B. Helgason et al. “Dissipative solitons in photonic molecules.” In: *Nature Photonics* 15.4 (2021), pp. 305–310.
- [124] Xiaoxiao Xue, Xiaoping Zheng, and Bingkun Zhou. “Super-efficient temporal solitons in mutually coupled optical cavities.” In: *Nature Photonics* 13.9 (2019), pp. 616–622.
- [125] Heming Wang et al. “Dirac solitons in optical microresonators.” In: *Light: Science & Applications* 9.1 (2020), pp. 1–15.
- [126] Daniel C. Cole et al. “Soliton crystals in Kerr resonators.” In: *Nature Photonics* 11.10 (2017), pp. 671–676.
- [127] Hairun Guo et al. “Universal dynamics and deterministic switching of dissipative Kerr solitons in optical microresonators.” In: *Nature Physics* 13.1 (2017), pp. 94–102.
- [128] Erwan Lucas et al. “Breathing dissipative solitons in optical microresonators.” In: *Nature Communications* 8.1 (2017), pp. 1–11.
- [129] Christian Reimer et al. “Generation of multiphoton entangled quantum states by means of integrated frequency combs.” In: *Science* 351.6278 (2016), pp. 1176–1180.
- [130] Michael Kues et al. “On-chip generation of high-dimensional entangled quantum states and their coherent control.” In: *Nature* 546.7660 (2017), pp. 622–626.
- [131] Michael Kues et al. “Quantum optical microcombs.” In: *Nature Photonics* 13.3 (2019), pp. 170–179.
- [132] Melissa A. Guidry et al. “Quantum optics of soliton microcombs.” In: *Nature Photonics* 16.1 (2022), pp. 52–58.
- [133] Zijiao Yang et al. “A squeezed quantum microcomb on a chip.” In: *Nature Communications* 12.1 (2021), p. 4781.
- [134] Shota Yokoyama et al. “Ultra-large-scale continuous-variable cluster states multiplexed in the time domain.” In: *Nature Photonics* 7.12 (2013), pp. 982–986.
- [135] Warit Asavanant et al. “Generation of time-domain-multiplexed two-dimensional cluster state.” In: *Science* 366.6463 (2019), pp. 373–376.
- [136] L. Lu, J. Joannopoulos, and M. Soljačić. “Topological photonics.” In: *Nature Photon* 8 (2014), pp. 821–829.
- [137] Tomoki Ozawa et al. “Topological photonics.” In: *Reviews of Modern Physics* 91 (1 Mar. 2019), p. 015006.
- [138] Alexey Tikan et al. “Protected generation of dissipative Kerr solitons in supermodes of coupled optical microresonators.” In: *Science Advances* 8.13 (2022), eabm6982.

- [139] Arkadev Roy et al. “Topological optical parametric oscillation.” In: *Nanophotonics* 11.8 (2022), pp. 1611–1618.
- [140] Stefan Wabnitz. “Suppression of interactions in a phase-locked soliton optical memory.” In: *Optics Letters* 18.8 (1993), pp. 601–603.
- [141] François Leo et al. “Temporal cavity solitons in one-dimensional Kerr media as bits in an all-optical buffer.” In: *Nature Photonics* 4.7 (2010), pp. 471–476.
- [142] Yu-Hung Lai et al. “Brillouin backaction thermometry for modal temperature control.” In: *Optica* 9.7 (2022), pp. 701–705. DOI: 10.1364/OPTICA.459082.
- [143] William Loh et al. “Microresonator Brillouin laser stabilization using a microfabricated rubidium cell.” In: *Optics Express* 24 (2016), pp. 14513–14524.
- [144] Andrey B. Matsko et al. “Whispering-gallery-mode resonators as frequency references. I. Fundamental limitations.” In: *Journal of the Optical Society of America B* 24 (2007), pp. 1324–1335.
- [145] Anatoliy A. Savchenkov et al. “Whispering-gallery-mode resonators as frequency references. II. Stabilization.” In: *Journal of the Optical Society of America B* 24 (2007), pp. 2988–2997.
- [146] M. Niklès, L. Thévenaz, and P. A. Robert. “Brillouin gain spectrum characterization in single-mode optical fibers.” In: *Journal of Lightwave Technology* 15 (1997), pp. 1842–1851.
- [147] A. Jagannathan and R. Orbach. “Temperature and frequency dependence of the sound velocity in vitreous silica due to scattering off localized modes.” In: *Physical Review B* 41.5 (1990), p. 3153.
- [148] Zhiqian Yuan et al. “Linewidth enhancement factor in a microcavity Brillouin laser.” In: *Optica* 7.9 (2020), pp. 1150–1153. DOI: 10.1364/OPTICA.394311.
- [149] D. V. Strekalov et al. “Temperature measurement and stabilization in a birefringent whispering gallery mode resonator.” In: *Optics Express* 19 (2011), pp. 14495–14501.
- [150] I. Fescenko et al. “Dual-mode temperature compensation technique for laser stabilization to a crystalline whispering gallery mode resonator.” In: *Optics Express* 20 (2012), pp. 19185–19193.
- [151] William Loh et al. “Ultra-narrow linewidth Brillouin laser with nanokelvin temperature self-referencing.” In: *Optica* 6 (2019), pp. 152–159.
- [152] Qiancheng Zhao et al. “Integrated reference cavity with dual-mode optical thermometry for frequency correction.” In: *Optica* 8.11 (2021), pp. 1481–1487.

- [153] Heming Wang et al. “Petermann-factor sensitivity limit near an exceptional point in a Brillouin ring laser gyroscope.” In: *Nature Communications* 11.1 (2020), p. 1610. DOI: 10.1038/s41467-020-15341-6.
- [154] Gaurav Bahl et al. “Observation of spontaneous Brillouin cooling.” In: *Nature Physics* 8.3 (2012), pp. 203–207.
- [155] Myoung-Gyun Suh, Qi-Fan Yang, and Kerry J. Vahala. “Phonon-limited-linewidth of Brillouin lasers at cryogenic temperatures.” In: *Physical Review Letters* 119 (14 2017), p. 143901.
- [156] Jinkang Lim et al. “Probing 10 μ K stability and residual drifts in the cross-polarized dual-mode stabilization of single-crystal ultrahigh-Q optical resonators.” In: *Light: Science & Applications* 8.1 (2019), pp. 1–9.
- [157] L.F. Stokes, M. Chodorow, and H.J. Shaw. “All-fiber stimulated Brillouin ring laser with submilliwatt pump threshold.” In: *Optics Letters* 7.10 (1982), pp. 509–511.
- [158] X. Steve Yao. “High-quality microwave signal generation by use of Brillouin scattering in optical fibers.” In: *Optics Letters* 22.17 (1997), pp. 1329–1331.
- [159] Patrick T. Callahan, Michael C. Gross, and Michael L. Dennis. “Frequency-independent phase noise in a dual-wavelength Brillouin fiber laser.” In: *IEEE Journal of Quantum Electronics* 47.8 (2011), pp. 1142–1150.
- [160] Y. R. Shen and N. Bloembergen. “Theory of stimulated Brillouin and Raman scattering.” In: *Physical Review* 137 (6A Mar. 1965), A1787–A1805.
- [161] Arthur L. Schawlow and Charles H. Townes. “Infrared and optical masers.” In: *Physical Review* 112.6 (1958), p. 1940.
- [162] Ryan O Behunin et al. “Fundamental noise dynamics in cascaded-order Brillouin lasers.” In: *Physical Review A* 98.2 (2018), p. 023832.
- [163] Alexis Debut, Stéphane Randoux, and Jaouad Zemmouri. “Linewidth narrowing in Brillouin lasers: Theoretical analysis.” In: *Physical Review A* 62 (2 July 2000), p. 023803.
- [164] Melvin Lax. “Quantum noise. X. Density-matrix treatment of field and population-difference fluctuations.” In: *Physical Review* 157 (2 May 1967), pp. 213–231.
- [165] Charles Henry. “Theory of the linewidth of semiconductor lasers.” In: *IEEE Journal of Quantum Electronics* 18.2 (1982), pp. 259–264.
- [166] Kerry Vahala et al. “On the linewidth enhancement factor α in semiconductor injection lasers.” In: *Applied Physics Letters* 42.8 (1983), pp. 631–633. DOI: 10.1063/1.94054.
- [167] Christoph Harder, Kerry Vahala, and Amnon Yariv. “Measurement of the linewidth enhancement factor α of semiconductor lasers.” In: *Applied Physics Letters* 42.4 (1983), pp. 328–330.

- [168] I.D. Henning and J.V. Collins. “Measurements of the semiconductor laser linewidth broadening factor.” In: *Electronics Letters* 19.22 (1983), pp. 927–929.
- [169] John R. Rumble, ed. *CRC handbook of chemistry and physics*. 100th ed. CRC press, Internet Version 2019.
- [170] M.P. Van Exter, S.J.M. Kuppens, and J.P. Woerdman. “Excess phase noise in self-heterodyne detection.” In: *IEEE Journal of Quantum Electronics* 28.3 (1992), pp. 580–584.
- [171] Hanne Ludvigsen, Mika Tossavainen, and Matti Kaivola. “Laser linewidth measurements using self-homodyne detection with short delay.” In: *Optics Communications* 155.1-3 (1998), pp. 180–186.
- [172] Carl M. Bender and Stefan Boettcher. “Real spectra in non-Hermitian Hamiltonians having PT symmetry.” In: *Physical Review Letters* 80.24 (1998), p. 5243.
- [173] Carl M. Bender. “Making sense of non-Hermitian Hamiltonians.” In: *Reviews of Modern Physics* 70.6 (2007), p. 947.
- [174] Liang Feng, Ramy El-Ganainy, and Li Ge. “Non-Hermitian photonics based on parity–time symmetry.” In: *Nature Photonics* 11.12 (2017), pp. 752–762.
- [175] Ramy El-Ganainy et al. “The dawn of non-Hermitian optics.” In: *Communications Physics* 2.1 (2019), pp. 1–5.
- [176] Mohammad-Ali Miri and Andrea Alù. “Exceptional points in optics and photonics.” In: *Science* 363.6422 (2019), eaar7709.
- [177] Sang-Bum Lee et al. “Observation of an exceptional point in a chaotic optical microcavity.” In: *Physical Review Letters* 103.13 (2009), p. 134101.
- [178] A. Guo et al. “Observation of PT-symmetry breaking in complex optical potentials.” In: *Physical Review Letters* 103.9 (2009), p. 093902.
- [179] Christian E. Rüter et al. “Observation of parity–time symmetry in optics.” In: *Nature Physics* 6.3 (2010), pp. 192–195.
- [180] Alois Regensburger et al. “Parity–time synthetic photonic lattices.” In: *Nature* 488.7410 (2012), pp. 167–171.
- [181] Bo Peng et al. “Parity–time-symmetric whispering-gallery microcavities.” In: *Nature Physics* 10.5 (2014), pp. 394–398.
- [182] Jörg Doppler et al. “Dynamically encircling an exceptional point for asymmetric mode switching.” In: *Nature* 537.7618 (2016), pp. 76–79.
- [183] B. Peng et al. “Loss-induced suppression and revival of lasing.” In: *Science* 346.6207 (2014), pp. 328–332.
- [184] Liang Feng et al. “Single-mode laser by parity-time symmetry breaking.” In: *Science* 346.6212 (2014), pp. 972–975.

- [185] Hossein Hodaei et al. “Parity-time–symmetric microring lasers.” In: *Science* 346.6212 (2014), pp. 975–978.
- [186] M. Brandstetter et al. “Reversing the pump dependence of a laser at an exceptional point.” In: *Nature Communications* 5.1 (2014), pp. 1–7.
- [187] Jan Wiersig. “Enhancing the sensitivity of frequency and energy splitting detection by using exceptional points: Application to microcavity sensors for single-particle detection.” In: *Physical Review Letters* 112.20 (2014), p. 203901.
- [188] Zhong-Peng Liu et al. “Metrology with PT-symmetric cavities: Enhanced sensitivity near the PT-phase transition.” In: *Physical Review Letters* 117.11 (2016), p. 110802.
- [189] Jinhan Ren et al. “Ultrasensitive micro-scale parity-time-symmetric ring laser gyroscope.” In: *Optics Letters* 42.8 (2017), pp. 1556–1559.
- [190] Satoshi Sunada. “Large Sagnac frequency splitting in a ring resonator operating at an exceptional point.” In: *Physical Review A* 96.3 (2017), p. 033842.
- [191] Pai-Yen Chen et al. “Generalized parity–time symmetry condition for enhanced sensor telemetry.” In: *Nature Electronics* 1.5 (2018), pp. 297–304.
- [192] Zhenya Dong et al. “Sensitive readout of implantable microsensors using a wireless system locked to an exceptional point.” In: *Nature Electronics* 2.8 (2019), pp. 335–342.
- [193] Weijian Chen et al. “Exceptional points enhance sensing in an optical microcavity.” In: *Nature* 548.7666 (2017), pp. 192–196.
- [194] Hossein Hodaei et al. “Enhanced sensitivity at higher-order exceptional points.” In: *Nature* 548.7666 (2017), pp. 187–191.
- [195] Mohammad P Hokmabadi et al. “Non-Hermitian ring laser gyroscopes with enhanced Sagnac sensitivity.” In: *Nature* 576.7785 (2019), pp. 70–74.
- [196] Mengzhen Zhang et al. “Quantum noise theory of exceptional point sensors.” In: *Physical Review Letters* 123.18 (2019), p. 180501.
- [197] W. Langbein. “No exceptional precision of exceptional-point sensors.” In: *Physical Review A* 98.2 (2018), p. 023805.
- [198] Hoi-Kwan Lau and Aashish A Clerk. “Fundamental limits and non-reciprocal approaches in non-Hermitian quantum sensing.” In: *Nature Communications* 9.1 (2018), pp. 1–13.
- [199] Chong Chen, Liang Jin, and Ren-Bao Liu. “Sensitivity of parameter estimation near the exceptional point of a non-Hermitian system.” In: *New Journal of Physics* 21.8 (2019), p. 083002.
- [200] N. Asger Mortensen et al. “Fluctuations and noise-limited sensing near the exceptional point of parity-time-symmetric resonator systems.” In: *Optica* 5.10 (2018), pp. 1342–1346.

- [201] E. J. Post. “Sagnac effect.” In: *Reviews of Modern Physics* 39 (1967), pp. 475–493.
- [202] Klaus Petermann. “Calculated spontaneous emission factor for double-heterostructure injection lasers with gain-induced waveguiding.” In: *IEEE Journal of Quantum Electronics* 15.7 (1979), pp. 566–570.
- [203] A.E. Siegman. “Excess spontaneous emission in non-Hermitian optical systems. I. Laser amplifiers.” In: *Physical Review A* 39.3 (1989), p. 1253.
- [204] W.A. Hamel and J.P. Woerdman. “Observation of enhanced fundamental linewidth of a laser due to nonorthogonality of its longitudinal eigenmodes.” In: *Physical Review Letters* 64.13 (1990), p. 1506.
- [205] Yuh-Jen Cheng, C.G. Fanning, and A.E. Siegman. “Experimental observation of a large excess quantum noise factor in the linewidth of a laser oscillator having nonorthogonal modes.” In: *Physical Review Letters* 77.4 (1996), p. 627.
- [206] Hans Wenzel et al. “Mechanisms of fast self pulsations in two-section DFB lasers.” In: *IEEE Journal of Quantum Electronics* 32.1 (1996), pp. 69–78.
- [207] Michael V. Berry. “Mode degeneracies and the Petermann excess-noise factor for unstable lasers.” In: *Journal of Modern Optics* 50.1 (2003), pp. 63–81.
- [208] Soo-Young Lee et al. “Divergent Petermann factor of interacting resonances in a stadium-shaped microcavity.” In: *Physical Review A* 78.1 (2008), p. 015805.
- [209] Jan Wiersig, Sang Wook Kim, and Martina Hentschel. “Asymmetric scattering and nonorthogonal mode patterns in optical microspirals.” In: *Physical Review A* 78.5 (2008), p. 053809.
- [210] Henning Schomerus. “Excess quantum noise due to mode nonorthogonality in dielectric microresonators.” In: *Physical Review A* 79.6 (2009), p. 061801.
- [211] Gwangsu Yoo, H.-S. Sim, and Henning Schomerus. “Quantum noise and mode nonorthogonality in non-Hermitian PT-symmetric optical resonators.” In: *Physical Review A* 84.6 (2011), p. 063833.
- [212] Y.D. Chong and A. Douglas Stone. “General linewidth formula for steady-state multimode lasing in arbitrary cavities.” In: *Physical Review Letters* 109.6 (2012), p. 063902.
- [213] Jing Zhang et al. “A phonon laser operating at an exceptional point.” In: *Nature Photonics* 12.8 (2018), pp. 479–484.
- [214] Robert Adler. “A study of locking phenomena in oscillators.” In: *Proceedings of the IRE* 34.6 (1946), pp. 351–357.
- [215] J.D. Cresser. “Quantum noise in ring-laser gyros. III. Approximate analytic results in unlocked region.” In: *Physical Review A* 26.1 (1982), p. 398.

- [216] R.J.C. Spreeuw et al. “Mode coupling in a He-Ne ring laser with backscattering.” In: *Physical Review A* 42.7 (1990), p. 4315.
- [217] Eva S. Ferre-Pikal et al. “IEEE standard definitions of physical quantities for fundamental frequency and time metrology—random instabilities.” In: *IEEE Std Std 1139-2008* (2009), pp. c1–35.
- [218] A.M. Van der Lee et al. “Excess quantum noise due to nonorthogonal polarization modes.” In: *Physical Review Letters* 79.22 (1997), p. 4357.
- [219] Raktim Sarma et al. “Rotating optical microcavities with broken chiral symmetry.” In: *Physical Review Letters* 114.5 (2015), p. 053903.
- [220] A.E. Kaplan and Pierre Meystre. “Enhancement of the Sagnac effect due to nonlinearly induced nonreciprocity.” In: *Optics Letters* 6.12 (1981), pp. 590–592.
- [221] Ewan M. Wright et al. “Theory of the nonlinear Sagnac effect in a fiber-optic gyroscope.” In: *Physical Review A* 32.5 (1985), p. 2857.
- [222] Leonardo Del Bino et al. “Symmetry breaking of counter-propagating light in a nonlinear resonator.” In: *Scientific Reports* 7 (2017), p. 43142.
- [223] Zhiquan Yuan et al. “Correlated self-heterodyne method for ultra-low-noise laser linewidth measurements.” In: *Optics Express* 30.14 (2022), pp. 25147–25161. DOI: 10.1364/OE.458109.
- [224] Zachary L. Newman, Vincent Maurice, Tara Drake, et al. “Architecture for the photonic integration of an optical atomic clock.” In: *Optica* 6.5 (2019), pp. 680–685.
- [225] Myoung-Gyun Suh and Kerry J. Vahala. “Soliton microcomb range measurement.” In: *Science* 359.6378 (2018), pp. 884–887.
- [226] Bonny L. Schumaker. “Noise in homodyne detection.” In: *Optics Letters* 9.5 (1984), pp. 189–191.
- [227] Warren F. Walls. “Cross-correlation phase noise measurements.” In: *Proceedings of the 1992 IEEE Frequency Control Symposium*. IEEE. 1992, pp. 257–261.
- [228] Xiaopeng Xie et al. “Phase noise characterization of sub-Hertz linewidth lasers via digital cross correlation.” In: *Optics Letters* 42.7 (2017), pp. 1217–1220.
- [229] Minh Tran et al. “Extending the spectrum of fully integrated photonics.” In: *arXiv preprint arXiv:2112.02923* (2021).
- [230] Maurice S. Bartlett. “Smoothing periodograms from time-series with continuous spectra.” In: *Nature* 161.4096 (1948), pp. 686–687.
- [231] B. Dahmani, L. Hollberg, and R. Drullinger. “Frequency stabilization of semiconductor lasers by resonant optical feedback.” In: *Optics Letters* 12.11 (1987), pp. 876–878.

- [232] Dag Roar Hjelme, Alan Rolf Mickelson, and Raymond G. Beausoleil. “Semiconductor laser stabilization by external optical feedback.” In: *IEEE Journal of Quantum Electronics* 27.3 (1991), pp. 352–372.
- [233] Bohan Li et al. “Reaching fiber-laser coherence in integrated photonics.” In: *Optics Letters* 46.20 (2021), pp. 5201–5204. DOI: 10.1364/OL.439720.
- [234] Bohan Li et al. “High-coherence hybrid-integrated 780 nm source by self-injection-locked second-harmonic generation in a high-Q silicon-nitride resonator.” In: *Optica* 10.9 (2023), pp. 1241–1244. DOI: 10.1364/OPTICA.498391.
- [235] Andrew D. Ludlow et al. “Optical atomic clocks.” In: *Reviews of Modern Physics* 87.2 (2015), p. 637.
- [236] Jeff Hecht. “Lidar for self-driving cars.” In: *Optics and Photonics News* 29.1 (2018), pp. 26–33.
- [237] Christian L. Degen, Friedemann Reinhard, and Paola Cappellaro. “Quantum sensing.” In: *Reviews of Modern Physics* 89.3 (2017), p. 035002.
- [238] Xiyuan Lu et al. “Efficient photoinduced second-harmonic generation in silicon nitride photonics.” In: *Nature Photonics* 15.2 (2021), pp. 131–136.
- [239] Adrien Billat et al. “Large second harmonic generation enhancement in Si₃N₄ waveguides by all-optically induced quasi-phase-matching.” In: *Nature Communications* 8.1 (2017), p. 1016.
- [240] Daniel D. Hickstein et al. “Self-organized nonlinear gratings for ultrafast nanophotonics.” In: *Nature Photonics* 13.7 (2019), pp. 494–499.
- [241] Edgars Nitiss et al. “Optically reconfigurable quasi-phase-matching in silicon nitride microresonators.” In: *Nature Photonics* 16.2 (2022), pp. 134–141.
- [242] Anat Siddharth et al. “Near ultraviolet photonic integrated lasers based on silicon nitride.” In: *APL Photonics* 7.4 (2022), p. 046108.
- [243] Mateus Corato-Zanarella et al. “Widely tunable and narrow-linewidth chip-scale lasers from near-ultraviolet to near-infrared wavelengths.” In: *Nature Photonics* 17.2 (2023), pp. 157–164.
- [244] Jingwei Ling et al. “Self-injection locked frequency conversion laser.” In: *Laser & Photonics Reviews* (2023), p. 2200663. DOI: 10.1002/lpor.202200663.
- [245] Cornelis A.A. Franken et al. “Hybrid-integrated diode laser in the visible spectral range.” In: *Optics Letters* 46.19 (2021), pp. 4904–4907.
- [246] Grigory Lihachev et al. “Platicon microcomb generation using laser self-injection locking.” In: *Nature Communications* 13.1 (2022), p. 1771.

- [247] Chao Xiang et al. “3D integration enables ultralow-noise isolator-free lasers in silicon photonics.” In: *Nature* 620.7972 (2023), pp. 78–85.